

**Experimental and theoretical characterization of thermal behavior of large  
format pouch type lithium-ion battery**

by

Yang Hu

A dissertation submitted to the Graduate Faculty of  
Auburn University  
in partial fulfillment of the  
requirements for the Degree of  
Doctor of Philosophy

Auburn, Alabama  
May 1, 2021

Keywords: lithium-ion battery, thermal behavior, experimental characterization, electrochemical-  
thermal model, degradation

Copyright 2021 by Yang Hu

Approved by

Song-Yul Choe, Chair, Professor of Mechanical Engineering  
Jeffrey Fergus, Professor of Materials Engineering  
Roy W. Knight, Associate Professor of Mechanical Engineering  
Yanzhao Cao, Professor of Mathematics and Statistics

## Abstract

Fundamental understanding of the heat generation process of lithium-ion batteries during operations is crucial for securing lifespan and safety by the cost-effective and efficient design of thermal management systems. Heat generation rate (HGR) of lithium-ion batteries varies at different operation conditions, such as charge and discharge rates, state of charge (SOC), temperatures and degradation conditions. In the first part of this work, a low-cost and high-performance multifunctional calorimeter is firstly developed. The calorimeter uses the thermoelectric assemblies (TEAs) as hardware and accompanied with a feedback loop, which enables the dynamic measurement of HGR and the active temperature control. The HGR performance of a large format lithium-ion cells is measured and compared as a function of charge and discharge rates, SOC, temperatures and degradation conditions, and the associated energy efficiency is analyzed. These works are presented as the first and second part of the dissertation.

The sources of HGR within lithium-ion cells are predominantly classified as reversible heat and irreversible heat. The reversible heat is generated by a change in entropy during the electrochemical reactions and can be estimated using the entropy coefficient. The irreversible heat is caused by the resistances that represent concentration, activation, and Ohmic polarizations. In the third part, we developed several novel experimental techniques that facilitate the fast and accurate characterization of the two heat source terms, which include (1) accelerated equilibration method, (2) hybridized time-frequency domain analysis (HTFDA) method, and (3) improved frequency-domain calorimetric method, and (4) wavelet-transform based simultaneous and continuous characterization method. The results are compared with those measured by the

conventional experimental methods, and show advantages with respect to measurement time and accuracy.

In order to further explore the heat generation mechanism within lithium-ion cells, an electrochemical-thermal life model is developed and validated. The electrochemical model describes the cell's internal reaction mechanisms such as the mass transport, charge conservation, and electrochemical kinetics; the degradation model describes the aging mechanisms including the solid electrolyte interphase (SEI) layer formation and lithium plating; while the associated HGRs are modeled by the coupled thermal model. Based on the developed model, the heat generation and the associated mechanism can be analyzed for both fresh and aged cells. This work is presented in the fourth part of the dissertation.

As a closing work to the dissertation, we further proposed an improved battery electrochemical model by considering a SOC-dependent diffusion coefficient lithium ions in cathode. The model has been validated to show a drastic increase of the accuracy in predicting the terminal voltage, while maintaining low computational time. The work may provide guidelines for further improvement and optimization of the battery model.

## Acknowledgments

First and foremost, I would like to extend my sincere gratitude and appreciation to my advisor, Dr. Song-Yul Choe, for his kind advice and support for my PhD study during the past five years. He has been supportive since the first day I start my journey in Auburn. He gave me insightful guidance on my research, and freedom to develop my own ideas; he gave me care and encouragement when I am stuck in difficulties; and he helped me develop scientific mindset and critical thinking skills, which will go a long way towards my career and life.

My appreciation also extends to the committee members: Dr. Jeffrey Fergus, Dr. Roy Knight, and Dr. Yanzhao Cao, for their consistent encouragement, constructive comments, and valuable suggestions during the completion of the dissertation. I would also like to thank my co-workers: Dr. Xinchun Zhao, Dr. Yilin Yin, Dr. Yalan Bi, Mr. Minseok Song, Mr. Xiaoniu Du, and Ms. Kyungjin Yu, for the intense discussions and their support to my work. Finally, I would like to thank my family and friends, for their support and unconditional love.

I believe in Auburn and love it! War Eagle!

## Table of Contents

Abstract .....	ii
Acknowledgments.....	iv
List of Tables .....	ix
List of Figures .....	x
List of Symbols.....	xv
List of Abbreviations .....	xix
Chapter 1. Introduction .....	1
1.1 Background .....	1
1.2 Motivation and objectives .....	2
1.3 Scholarly contributions and dissertation structure .....	3
Chapter 2. Design of a multifunctional calorimeter and measurement of heat generation rate.....	5
2.1 Literature review .....	5
2.2 Design of calorimeter for heat generation measurement .....	6
2.2.1 Modeling.....	7
2.2.2 Temperature control and HGR estimation using Kalman filter .....	8
2.2.3 Calibration .....	9
2.3 Experiments.....	13
2.3.1 Cell and test setup.....	13
2.3.2 Experimental procedure.....	15
2.4 Result and discussion .....	19

2.4.1 HGR at different C-rates and temperatures .....	19
2.4.2 Analysis of total heat generation and energy efficiency.....	22
2.5 Summary .....	25
Chapter 3. Characterization of heat source terms .....	27
3.1 Literature review .....	27
3.2 Accelerated equilibration method .....	30
3.2.1 Modeling and optimal time control .....	30
3.2.2 Model validation and simulation analysis .....	35
3.2.3 Experimental result and discussion .....	43
3.2.4 Summary.....	52
3.3 Hybridized time-frequency domain analysis (HTFDA) method.....	53
3.3.1 Principle.....	53
3.3.2 Experiments .....	58
3.3.3 Result and discussion.....	61
3.3.4 Summary.....	77
3.4 Improved frequency-domain calorimetric method.....	78
3.4.1 Principle.....	78
3.4.2 Experiments .....	81
3.4.3 Result and discussion.....	81
3.4.4 Summary.....	89

3.5 Wavelet-transform based simultaneous and continuous characterization method.....	90
3.5.1 Principle.....	91
3.5.2 Experiment.....	94
3.5.3 Result and discussion.....	96
3.5.4 Summary.....	106
Chapter 4. Modeling and theoretical analysis based on an electrochemical-thermal life model	108
4.1 Model development.....	108
4.1.1 Electrochemical model .....	108
4.1.2 Degradation model .....	109
4.1.3 Thermal model.....	110
4.2 Model validation and analysis.....	111
4.3 Summary .....	114
Chapter 5. Improved battery electrochemical model considering variable diffusivity of lithium ions in solid.....	115
5.1 Literature review .....	115
5.2 Model development and simplification.....	117
5.3 Determination of diffusion coefficient in solid phase of cathode .....	122
5.3.1 Overpotential and parameter sensitivity analysis .....	122
5.3.2 ROM-SPM based diffusion coefficient determination algorithm .....	127
5.4 Prediction of the $D_{s,p}$ and model validation .....	130

5.4.1 Experiments and $D_{s,p}$ prediction .....	130
5.4.2 ROM-SPMVD validation .....	134
5.5 Summary .....	140
Chapter 6. Conclusion.....	141
6.1 Conclusion.....	141
6.2 Future work .....	143
6.2.1 Experimental measurement and modeling of 2D heat generation behavior (2D-HGR) .....	143
6.2.2 Improvement of battery model using machine learning methods .....	143
Reference .....	145

## List of Tables

Table 1. Governing equations of lithium-ion battery.....	30
Table 2. Parameters for lithium-ion cell electrochemical model at 25°C.....	36
Table 3. Time cost for two profiles at 50% SOC at 25°C. ....	46
Table 4. Time cost for two profiles at 75% and 25% SOC at 25°C. ....	48
Table 5. Times for two profiles at 40°C and 10°C. ....	51
Table 6. Parameters and comparison of the required time for measurement of the entropy coefficient between HTFDA and conventional potentiometric method (CPM).....	60
Table 7. Parameters for lithium-ion cell electrochemical-thermal life model at 25°C.....	111
Table 8. Mathematical expression of sensitivity variables of the parameters for ROM-SPM ...	125
Table 9. Initial $D_{s,p}$ and learning rate at 0°C, 25°C and 45°C.....	131
Table 10. Measured lithium ion diffusion coefficient of NMC622 materials from literatures...	133

## List of Figures

Figure 1. (a) Schematic diagram of thermoelectric assemblies (TEA); (b) block diagram of the temperature control and HGR estimation; (c) schematic architecture of an artificial neural network for the static calibration. ....	12
Figure 2. Calorimeter setup: (a) side view of the calorimeter structure, (b) photo of the calorimeter, (c) connection to the clamps and locations of thermocouples. ....	15
Figure 3. Static calibration results at 25 °C: (a) training result of ANN and (b) performance evaluation. Dynamic calibration results at 25 °C: (c) pulse heat generation profile and (d) discharge heat generation profile. ....	17
Figure 4. Measurement results of HGRs at different C-rate during (a) charging and (b) (c) discharging at 25 °C, and at different temperatures under 1C (d) charging and (e) discharging. ....	21
Figure 5. Measurement results under driving cycles at 25 °C: (a) electric power, (b) SOC and (c) HGR. ....	22
Figure 6. Comparison of input and output electric energy, total heat generated, and the percentage of energy dissipation. ....	25
Figure 7. Schematic diagram of the model setup. ....	32
Figure 8. Model validation by comparison between experimental and simulated terminal voltage at C/3 (a) charge and (b) discharge at 25°C. ....	37
Figure 9. Pulse-relaxation for equilibration. (a) Current profile along with SOC, (b) terminal voltage, (c) and (d) average and surface concentration of lithium ion in negative and positive electrode particles. ....	38

Figure 10. Optimal-time current profile for equilibration. (a) Current profile along with SOC, (b) terminal voltage, (c) and (d) average and surface concentration of lithium ion in negative and positive electrode particles.....	40
Figure 11. Simulation result of solid phase lithium ion concentration distribution along the radial direction in (a) anode and (b) cathode. ....	42
Figure 12. Comparison of experimental results by pulse-relaxation profile and the optimal-time current profile at around 50% SOC, 25°C: (a) current profile, (b) SOC variation, (c) terminal voltage, and (d) voltage difference between the relaxation voltage and OCV. ....	45
Figure 13. Comparison of experimental results by pulse-relaxation profile and the optimal-time current profile at 25°C: (a.1, b.1) terminal voltage, and (a.2, b.2) voltage difference between the relaxation voltage and OCV at around 75% SOC and 25% SOC, respectively. ....	48
Figure 14. Model validation by comparison between experimental and simulated terminal voltage at C/3 charge and discharge at (a.1) 40°C and (b.1) 10°C, respectively. Comparison of experimental results by pulse-relaxation profile and the optimal-time current profiles: (a.2, b.2) current profile, (a.3, b.3) terminal voltage, and (a.4, b.4) voltage difference between the relaxation voltage and OCV at 40°C and 10°C, respectively. ....	51
Figure 15. Averaged surface temperature and (b) $U_{OC}$ response versus time for different ETCRs: $R_1=0.5^\circ\text{C}/\text{min}$ , $R_2=1.0^\circ\text{C}/\text{min}$ , $R_3=1.5^\circ\text{C}/\text{min}$ , $R_4=2.0^\circ\text{C}/\text{min}$ , $R_5=2.5^\circ\text{C}/\text{min}$ , for clarity, only one period test of $R_1$ was plotted; (c) frequency spectra of $U_{OC}$ , at 100% SOC. ....	62
Figure 16. Comparison of determined entropy coefficient at different (a) ETCR and (b) temperature amplitudes at 100% SOC. The entropy coefficient measured from conventional potentiometric method, as a reference (black dash line).....	64
Figure 17. Voltage offset after resting time of 10, 20, 30 and 65 minutes as a function of SOC. ....	66

Figure 18. Measured voltage, background offset and the voltage after correction at (a) 100% SOC, (b) 50% SOC and (c) 20% SOC, and (d) ~ (f) the corresponding frequency spectra. ....	68
Figure 19. (a) Averaged surface temperature and (b) $U_{OC}$ response at different temperature amplitudes: $\Delta T_1=2.5^\circ\text{C}$ , $\Delta T_2=5^\circ\text{C}$ , $\Delta T_3=10^\circ\text{C}$ , $\Delta T_4=15^\circ\text{C}$ and $\Delta T_5=20^\circ\text{C}$ ; (c) frequency spectra of $U_{OC}$ at 100%SOC.....	69
Figure 20. Entropy coefficient as a function of SOC for graphite-LMO/NMC battery by HTFDA and comparison with the measurement results from (a) conventional potentiometric method and (b) calorimetric method.....	73
Figure 21. Entropy coefficient values of commercial graphite-LMO/NMC battery at different temperatures of $0^\circ\text{C}$ , $15^\circ\text{C}$ , $25^\circ\text{C}$ , $35^\circ\text{C}$ and $45^\circ\text{C}$ . ....	75
Figure 22. Entropy coefficient values of commercial graphite-LMO/NMC battery at different aging conditions. ....	77
Figure 23. (a) Input current, (b) terminal voltage response, and measured HGR at (c.1) 30% SOC, (d.1) 60% SOC and (e.1) 80% SOC in time domain and the corresponding frequency spectra (c.2) ~ (e.2). ....	83
Figure 24. Calculated (a) entropy coefficient and (b) internal resistance as a function of SOC from the calorimetric method and comparison with those by potentiometric method and EIS method, respectively .....	85
Figure 25. Measured (a) total heat during discharge and charge and (b) irreversible and reversible heat during discharge. Comparison between the calculated and measured (c) irreversible and (d) reversible heat during discharge. ....	89
Figure 26. Schematic diagram of the test station .....	94

Figure 27. (a) Input current and corresponding response of (b) terminal voltage and (c) heat generation rate at 25°C. ....	97
Figure 28. Full profile of heat generation rate. ....	98
Figure 29. Scalogram of (a) modulus of wavelet coefficient by the CWT of heat generation rate and (b) wavelet coherence between heat generation rate and input current .....	101
Figure 30. Calculated (a) entropy coefficient and (b) internal resistance as a function of SOC from the wavelet analysis result and comparison with those by potentiometric and EIS method, respectively. Grey regions represent the data with errors caused by the edge effects of wavelet transform. ....	103
Figure 31. Comparison of measured and calculated heat generation rate under (a) 1C discharge and (b) 1C charge. Grey regions for erroneous data caused by the edge effects of wavelet transform. ....	106
Figure 32. Description of electrochemical model of lithium-ion battery .....	108
Figure 33. Description of degradation model considering side reaction and lithium plating/stripping. ....	110
Figure 34. Description of electrochemical-model-based thermal model based on.....	111
Figure 35 Model validation results: (a) capacity fade at 2C CC charging; comparison of discharging behaviors of (b) terminal voltage and (c) heat generation rate at 2C CC discharging; (d) total reversible and irreversible heat generation. ....	113
Figure 36. Schematic diagram of ROM-SPM.....	118
Figure 37. (a) Overpotential analysis and (b) parameter sensitivity analysis result of ROM-SPM. ....	124

Figure 38. (a) Flowchart of diffusion coefficient determination procedure. (b) Termination tolerance versus SOC, combined with an OCV-SOC curve as a reference. (c) Training and fitting path of  $D_{s,p}$  and  $V_{cell}$  to show the convergence of the algorithm..... 130

Figure 39. (a) Predicted  $D_{s,p}(SOC)$  at 0°C, 25°C and 45°C. The black dash line represents the experimental measured diffusion coefficient using GITT method at 25°C taken from Ref. [46], (b) Logarithmic scale of averaged diffusion coefficient versus inverse temperature at 0, 25 and 45°C. .... 133

Figure 40. Validation result: 1C, 0.6C and 0.2C CC discharge at 25°C..... 135

Figure 41. Comparison of (a) RMSE and (b) computation time between ROM-SPM and ROM-SPMVD at 1C, 0.6C and 0.2C CC discharge at 25°C. .... 136

Figure 42. Validation result: (a) HPPC current; (b) HPPC voltage curves. .... 138

Figure 43. Validation result: 1C CC discharge at (a) 45°C and (b) 0°C..... 139

## List of Symbols

$A$	Sandwich area of the cell ( $\text{cm}^2$ ) / contact area ( $\text{cm}^2$ ) / surface area of active material ( $\text{cm}^2$ )
$a_s$	Specific surface area of electrode ( $\text{cm}^{-1}$ )
$c$	Ion concentration ( $\text{mol m}^{-3}$ )
$c_{s,ave}$	Volume-averaged concentration of lithium ion in solid phase ( $\text{mol cm}^{-3}$ )
$c_{s,max}$	Maximum concentration of lithium ion in solid phase ( $\text{mol cm}^{-3}$ )
$c_{s,surf}$	Surface concentration of lithium ion in solid phase ( $\text{mol cm}^{-3}$ )
$c_e$	Concentration of lithium ion in electrolyte phase ( $\text{mol cm}^{-3}$ )
$D$	Diffusivity ( $\text{cm}^2 \text{s}^{-1}$ )
$D_s$	Diffusivity of lithium ion in solid phase ( $\text{cm}^2 \text{s}^{-1}$ )
$D_e^{eff}$	Effective diffusivity of lithium ion in electrolyte phase ( $\text{cm}^2 \text{s}^{-1}$ )
$E$	Open circuit voltage (V)
$E_{elec}$	Electric energy (J)
$F$	Faraday constant ( $96,487 \text{ C mol}^{-1}$ )
$f$	Frequency (Hz)
$I$	Applied current (A)
$I_{TEM}$	Input current to TEM (A)
$i_0$	Exchange current density ( $\text{A cm}^{-2}$ )

$j^{Li}$	Reaction rate ( $A\ cm^{-3}$ )
$K$	Thermal conductance ( $WK^{-1}$ )
$k$	Thermal conductivity ( $Wm^{-1}K^{-1}$ ) / kinetic rate constant ( $A\ cm^{-2})(cm^3mol^{-1})^{1.5}$ )
$k_0$	Isolation coefficient due to SEI
$L$	Thickness of cell unit (cm)
$l$	Thickness of the micro cell (m)
$Q$	Capacity of the cell (Ah) / Heat energy (J)
$\dot{Q}$	Heat generation rate (W)
$q$	Amount of ion loss (Ah)
$q_{ave}$	Volume-averaged concentration flux of lithium ion in solid phase ( $mol\ cm^{-4}$ )
$R$	Resistance ( $\Omega$ ) / universal gas constant ( $8.314\ J\ mol^{-1}\ K^{-1}$ )
$R_s$	Radius of spherical electrode particle (cm)
$r$	Coordinate along the radius of electrode particle (cm)
$S$	Seebeck coefficient ( $VK^{-1}$ )
$sgn$	Sign function
$T$	Cell temperature (K)
$t$	Time (s)
$U$	Equilibrium potential (V)

$U_{oc}$	Open circuit voltage (V)
$V$	Voltage (V) or volume of the composite electrode ( $\text{m}^3$ )
$\tilde{V}$	Molar volume ( $\text{m}^3 \text{mol}^{-1}$ )
$x$	Stoichiometric number of the anode / Cartesian coordinate
$y$	Stoichiometric number of the cathode
$z$	Output state of the nonlinear state-space model

#### Greek symbols

$\alpha$	Transfer coefficient for an electrode reaction / Thermal diffusivity ( $\text{m}^2\text{s}^{-1}$ )
$\delta$	Thickness (cm) / Dirac delta function
$\varepsilon$	Volume fraction of a porous medium
$\phi$	Potential (V)
$\eta$	Overpotential of electrode reaction (V)
$\theta$	Aging parameters
$\kappa$	Ionic conductivity ( $\text{S m}^{-1}$ )
$\sigma$	Conductivity ( $\text{S m}^{-1}$ )
$\lambda$	Fraction of plated lithium to form secondary SEI

## Subscripts and Superscripts

*act* Actual

*amb* Ambient

*ch* Charge

*dch* Discharge

*elec* Electric

*irr* Irreversible

*mea* Measurable

*n* Negative electrode

*p* Positive electrode

*ref* Reference

*rev* Reversible

*s* Separator

*sto* Stored

## List of Abbreviations

ANN	Artificial neural network
ARC	Accelerated rate calorimetry
DAQ	Data acquisition
DC	Direct current
ECM	Equivalent circuit model
EIS	Electrochemical impedance spectroscopy
ETIS	Electrothermal impedance spectroscopy
EV	Electric vehicle
HDPE	High-density polyethylene
HEV	Hybrid electric vehicle
HGR	Heat generation rate
HPPC	Hybrid pulse power characterization
IHC	Isothermal heat conduction calorimetry
NBN	Neuron by neuron
PCB	Printed circuit board
PEV	Plug-in electric vehicle
SEI	Solid electrolyte interphase

SOC State of charge

SSE Sum of square error

TEA Thermoelectric assembly

TEM Thermoelectric module

TMS Thermal management system

## Chapter 1. Introduction

### 1.1 Background

Rechargeable lithium-ion batteries are widely used as an alternative energy storage system for pure electric, hybrid, and plug-in electric vehicles (EV, HEV and PEV) because of its high energy and power density and long cycling life. When energy is stored and retrieved, heat is generated due to charge transport, chemical reactions, and intercalation and deintercalation process within the cell. Some of the generated heat is transferred to the ambient environment or a cooling system, but the remaining heat generated raises the temperature within the cell, which affects overall performance of the battery [1]. Low temperatures decrease speed of electrochemical reactions, and increase lithium deposition reaction and consequently increase formation of dendrites [2], while high temperatures increase side reaction and accelerate degradation [3] [4]. In order to ensure optimal performance and prolong the lifespan of the cells, it is highly recommended maintaining the operating temperature between 15 °C and 35 °C [1], which is accomplished by thermal management system (TMS).

Cost-effective and efficient design of the TMS requires prediction or characterization of the heat generated at given operating ranges at first, which can be conveyed using thermal models or/and measurements, where the experimental time and accuracy of the measurements play the pivot role in the design process. The thermal characterization of cells includes measurement of the HGR as well as the associate heat source terms [5] [6]. The heat source terms can be divided into reversible heat and irreversible heat. The reversible heat is generated from the entropy change that takes place during electrochemical reactions, which amount can be estimated by the entropy coefficient at a given current and temperature, while the irreversible heat is caused by the internal

resistances of the cell owing to the concentration, activation, and Ohmic polarizations [7]. On the other hand, the heat generation mechanisms can be analyzed by a physics-based electrochemical-thermal life model. The electrochemical model describes the cell's internal reaction mechanisms such as the mass transport, charge conservation, and electrochemical kinetics; the degradation model describes the aging mechanisms including the solid electrolyte interphase (SEI) layer formation and lithium plating; while the associated HGRs are modeled by the coupled thermal model.

## 1.2 Motivation and objectives

Currently, the HGR of the lithium-ion batteries is mainly measured by accelerated rate calorimetry (ARC) and isothermal heat conduction calorimetry (IHC). Both methods provide sufficiently accurate and dynamic measurement results, but the cost of equipment is relatively high. In addition, the calorimeters are only for batteries that have a capacity on the order of 1Ah to 10Ah, and are limited to measurement at constant ambient temperatures. Conventionally, the measurement of entropy coefficient is conducted by the potentiometric or the calorimetric method, while the internal resistance of the battery can be measured from V-I characteristics, and EIS technique [8]. The measurement of both terms has to be carried out by two different methods, which is time-consuming and complicated.

Therefore, the objective of this dissertation is to develop an experimental method that can efficiently characterize the HGR and heat source terms of the lithium-ion battery. In addition, an electrochemical-thermal life model for the estimation of the electrochemical and thermal states of a battery with high fidelity is required, in order to have a comprehensive understanding of the

thermal behavior of large format pouch type lithium-ion battery at various temperature, C-rate and degradation conditions.

### 1.3 Scholarly contributions and dissertation structure

In this work, the development of a low-cost multifunctional calorimeter as hardware and the associated experimental methods for the characterization of HGR and heat source terms, and the establishment of the battery thermal model to explain the measured results could make certain scholarly contributions since it provides comprehensive and systematic guidelines for the research on the thermal behavior of the lithium-ion cells. In particular, the contributions are:

- Design of a low-cost and high-performance multifunctional calorimeter that enables the accurate and dynamic measurement of HGR.
- Propose several novel experimental techniques that facilitate the fast and accurate characterization of the two heat source terms, which include (1) accelerated equilibration method, (2) hybridized time-frequency domain analysis (HTFDA) method, and (3) improved frequency-domain calorimetric method, and (4) wavelet-transform based simultaneous and continuous characterization method.
- Develop a physics-based electrochemical-thermal life model for the analysis of the heat generation mechanism within lithium-ion cells.

This dissertation is organized as follows.

- Chapter 1 introduces the research background, motivation and objectives, and scholarly contributions.

- Chapter 2 includes a brief introduction to the design of a multifunctional calorimeter, calibration, and performance analysis, and presents measured HGR result of pouch-type lithium-ion cells using the developed calorimeter at different charging and discharging current, SOC, and temperatures. The associated energy efficiency is analyzed.
- Chapter 3 presents several novel experimental methods for the fast and accurate characterization of the reversible and irreversible heat sources.
- Chapter 4 describes an electrochemical-thermal life model and its validation against the experimental data. The HGR mechanisms of the lithium-ion cells are further analyzed.
- Chapter 5 proposed an improved battery electrochemical model by considering a SOC-dependent diffusion coefficient lithium ions in cathode, which is validated to have increased accuracy while maintaining low computational time.
- Chapter 6 concludes the dissertation.

## Chapter 2. Design of a multifunctional calorimeter and measurement of heat generation rate

### 2.1 Literature review

A Cost-effective and efficient design of the TMS requires knowledge of the thermal properties, temperature, and heat generation behaviors of the cells subject to various operating conditions such as charge or discharge rate, SOC, and temperatures [9]. Recently, several studies have been conducted to characterize the cell's heat generation and the associated mechanisms, which can be categorized as indirect and direct methods. The indirect methods determine the cell's heat generation from the temperature response by various types of thermal sensors such as thermocouples, thermistors, resistance temperature detectors, infrared thermal cameras, et al.[10]. Then, the heat generation rate (HGR) and the associated heat source terms are calculated according to battery thermal models [11], [12]. The methods do not require extra experimental equipment, but the accuracy is heavily dependent upon the accuracy of the thermal model and the associated parameters.

Conversely, the direct methods measure the HGR of a cell using calorimeters, such as accelerated rate calorimetry (ARC) and isothermal heat conduction calorimetry (IHC) [13], [14]. ARC is used to determine the HGR of 18650 cylindrical can-type lithium-ion cells in an adiabatic environment [15], [16], while IHC determines the HGR of cylindrical, coin or pouch type batteries at constant temperatures [17], [18]. Both methods provide sufficiently accurate and dynamic measurement capabilities, but the cost of equipment is relatively high.

Recently, several types of low-cost calorimeters have been proposed specifically for the measurement of the HGR of large-format pouch type lithium-ion batteries. One of the approaches involves wrapping a cell with thermally stable materials and placing it into a constant temperature

environment, and the HGR is calculated from the temperature change of the wrapped material [19], [20]. Since the temperature of the cell is not actively controlled, the cell's temperature can vary during the tests, which causes errors and in turn decreases the accuracy of the measurements. The second one uses heat flux sensors as the core components of the calorimeter to measure the cell's HGR, where the generated heat is pumped out by the water-cooling based cold plate to maintain the energy balance [21] [22]. However, the optimization of the mini-channel structure within the cold plate becomes an additional challenging issue for the calorimeter setup. The third calorimeter uses two thermoelectric modules (TEMs) as a heat pump, accompanied with a closed loop controller to regulate the surface temperature of the cell to a set reference, where the HGR is directly estimated by a Kalman filter with a simplified heat transfer model of the TEM [23] [24]. Since the tuning parameters for the model are calibrated at a constant temperature, it produces errors when ambient temperature fluctuates. Therefore, a new calorimeter should be designed for pouch type cells that minimizes the effects of heat generations in battery on the measurements, and calibrated to decouple the effect of ambient temperature variation.

## 2.2 Design of calorimeter for heat generation measurement

Since the heat generation in a battery dynamically changes during operation, and the temperature inside the cell tends to follow the heat generation, the accurate measurement of heat generation is very challenging because the individual heat source terms are a function of the temperature changes. In addition, the calorimeter needs to accommodate various packaging and format sizes typical of large capacity cells. Under those considerations, two Direct-to-Air thermoelectric assemblies (TEAs) are selected for a large format pouch cell type battery that function as a heat pump in the calorimeter, where the amount of heat flux is controlled by a bipolar power supply [25]. The surface temperature of the cell is measured using thermocouples and fed

back to the controller to compare with a reference temperature. The error is compensated by this controller, which controls a bipolar power supply. Ideally, the output of the controller should match any disturbances at a constant reference. In this calorimeter, the HGR is regarded as the disturbance and is equal to the output of the controller, allowing for the TEAs to remove the heat generated by the battery cell under operation.

### 2.2.1 Modeling

Figure 1(a) shows the schematic diagram of a single TEA that consists of metal plates, foam, heat sink, fan and thermoelectric modules (TEMs). The TEMs work based on the Peltier effect. When a current flows through the TEM, there is a temperature gradient formed between two sides that drives the heat from one side to the other, which is denoted as the heat pump rate ( $\dot{Q}_{pump}$ ), whose polarity and magnitude is dependent upon the polarity and magnitude of the current. However, the exact relationship of both quantities should consider several other thermal effects such as Thomson effect, Joule effect, and heat conduction [26], which is modeled to estimate the accurate HGR as an output variable of the controller. Under the assumption that the heat generated by Thomson effect is negligible [24], the actual heat pump rate of the TEM is expressed as:

$$\dot{Q}_{pump} = \alpha I_{TEM} T_2 - 0.5 I_{TEM}^2 R_{TEM} - K (T_3 - T_2) \quad (1)$$

, where  $\alpha$  is the Seebeck coefficient,  $I_{TEM}$  is the input current,  $R_{TEM}$  is the Ohmic resistance,  $K$  is the thermal conductance, and  $T_2$  and  $T_3$  denote the temperatures at the cold and hot side of the TEM, respectively.

In addition, there is a metal plate between the battery and the TEM that acts like a heat bridge and serves to efficiently conduct the generated heat from one side to the other. In this design, the

heat conduction process within the metal plate is simplified as one-dimensional heat conduction along the thickness direction, which is described by:

$$\frac{1}{\alpha} \frac{\partial T}{\partial t} = \frac{\partial^2 T}{\partial x^2}; \quad (2)$$

$$\text{Boundary condition: } -k \left. \frac{\partial T}{\partial x} \right|_{x=0} = \frac{\dot{Q}_{in}}{A}, \quad -k \left. \frac{\partial T}{\partial x} \right|_{x=d} = \frac{\dot{Q}_{pump}}{A};$$

$$\text{Initial condition: } T(t=0) = T_0$$

, where  $\alpha$  is the thermal diffusivity,  $k$  is the thermal conductivity,  $A$  is the contact area,  $x$  is the Cartesian coordinate across the cell, and  $t$  is the time.

### 2.2.2 Temperature control and HGR estimation using Kalman filter

Figure 1(b) shows the block diagram of the calorimeter that includes a temperature control loop and a HGR estimator loop.

In the temperature control loop, the averaged surface temperature of the cell ( $T_I$ ) is measured and compared with the input reference value ( $T_{ref}$ ), and the difference is amplified by linear controllers to adjust the input current of TEM, such that the tracking error between  $T_I$  and  $T_{ref}$  is reduced. The term  $I_{TEM}=f(V_{TEM})$  describes the voltage controlled current source of the bipolar power supply.

In the HGR estimator loop, a Kalman filter is employed to estimate  $\dot{Q}_{in}$  as a state and suppress the white noise present in the temperature measurement. A discrete-time state-space form of the model is obtained from the thermal model in Eq. (2) using the Crank-Nicolson method, and then along with Eq. (1) are rewritten in the form of:

$$\begin{aligned} X_k &= AX_{k-1} + BU_k + w_k \\ Y_k &= CX_k + v_k \end{aligned} \quad (3)$$

Here,  $X_k$  is the state vector of the system at time index  $k$ , and is expressed as  $X_k = [T_1 \ \cdots \ T_2 \ \dot{Q}_{in}]^T$ ,  $U_k$  is the input of the system  $U_k = \dot{Q}_{pump}$ ,  $Y_k$  is the output of the system  $Y_k = T_1$ ,  $w_k$  and  $v_k$  represent the process and sensor noises.

A two-step recursive estimation procedure is utilized, as shown in Figure 1(b). The time update is performed to compute the present states from the prior information in conjunction with the system model. Then, a measurement update takes place using present measurements to further compensate errors in the predicted state caused by the noise in the system. The detailed procedure is illustrated in Figure 1(b), where  $K$ ,  $Q$  and  $R$  represent Kalman gain, noise covariance of process and observation respectively. After each iteration, the estimation of the state  $\dot{Q}_{in}$  is obtained, denote as  $\hat{\dot{Q}}_{in}$ , which represents the HGR of the cell.

### 2.2.3 Calibration

Calibration of the calorimeter is carried out to determine the parameters of the Eq. (1) and (2). In addition, covariance of the Kalman filter should be tuned to optimize the dynamic response of the calorimeter. Thus, static and dynamic steps are performed.

#### (1) Static calibration

The term  $\dot{Q}_{pump}$  in Eq. (1), is a function of  $T_2$ ,  $T_3$  and  $I_{TEM}$ .  $T_2$  is the temperatures at the cold of the TEM that can be regarded as a constant at steady state.  $T_3$  is the temperature at the hot side of the TEM, which cannot be directly measured. However, since the hot side of TEM is next to

the heat sink exposed to the ambient,  $T_3$  can be expressed as a function of ambient temperature,  $T_{amb}$ . Thus, Eq. (1) is modified as follows:

$$\dot{Q}_{pump} = F(T_{amb}, V_{TEM}) \quad (4)$$

When the calorimeter is at steady state,  $\dot{Q}_{pump} = \dot{Q}_{in}$ , and  $\dot{Q}_{in}$  is the heat generated by a programmable heat source, such as a printed circuit board (PCB) with a known resistance. On the other hand, Eq.(4) is a nonlinear function that is hard to fit using an input and output data set. Therefore, a data-driven approach, artificial neural network (ANN) is employed.

ANN is a mathematical model composed of several interconnected processing neurons as units. The neurons and their connections can be trained with a data set to represent the relations between inputs and outputs without the knowledge of the exact information of the system model. Figure 1(c) shows a schematic architecture of ANN used for the static calibration, which is a multilayer perceptron (MLP) structure. The input vector includes the  $T_{amb}$  and  $V_{TEM}$  and the output is the  $\dot{Q}_{pump}$ . The neurons in both hidden layer and output layer have a sigmoid activation function. The training data for the ANN comes from the experimental measurement, which includes hundreds of data sets indicating the relationship between  $T_{amb}$ ,  $V_{TEM}$  and  $\dot{Q}_{pump}$  that cover all the possible testing conditions for the battery, such as the boundaries for HGR and ambient temperature fluctuations. The training procedure of the ANN is carried out using a highly efficient Neuron by Neuron (NBN) algorithm [27]. As a result, the relationship shown in Eq.(4) is excellently fit by the well-trained ANN. The details of the training data collection, training procedure, and the performance analysis of ANN can be found in the next section.

## (2) Dynamic calibration

Dynamic calibration is used to identify the parameters of Eq. (2) and optimize the covariance values of Kalman filter. Different profiles of HGR are produced using a programmable heat source. The values of the parameters and the covariance are tuned such that the estimated HGR has a good match with that of the programmable heat source in both accuracy and time response.

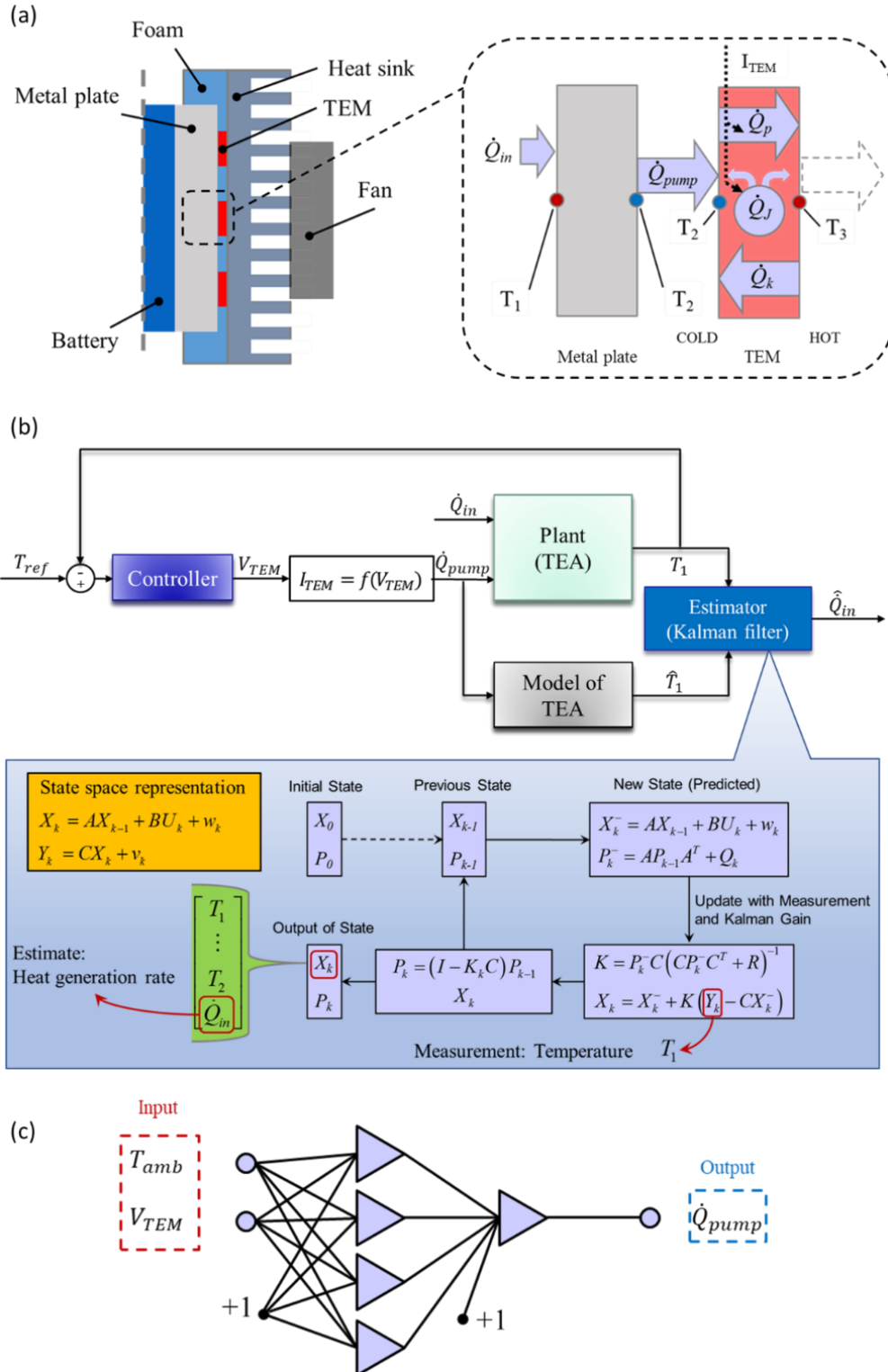


Figure 1. (a) Schematic diagram of thermoelectric assemblies (TEA); (b) block diagram of the temperature control and HGR estimation; (c) schematic architecture of an artificial neural network for the static calibration.

## 2.3 Experiments

### 2.3.1 Cell and test setup

The cells used for the experiment are commercial LMO-NMC/graphite cells with following key specifications:

- Active materials: LMO (30%) – NMC (70%) for cathode, and graphite for anode,
- Electrolyte: Solution of  $\text{LiPF}_6$ ,
- Nominal capacity: 25.9Ah,
- Nominal voltage: 3.65V,
- End-of-charge voltage, current: 4.15V, 1.25A,
- End-of-discharge voltage: 2.5V,
- Dimension: 203mm×154mm×7.2mm.

A test station is designed to charge and discharge the cell using a DC power supply and an electronic load, which are controlled via National Instruments data acquisition (DAQ) system along with the LabVIEW software.

The calorimeter is constructed with two 160W Direct-to-Air thermoelectric assemblies (TEAs) as the main bodies that are connected in series. The detailed drawing of the calorimeter is depicted in Figure 2(a), where a cell is placed between an upper (TEA #1) and a lower TEAs (TEA #2), and graphite thermal sheets are used to reduce the thermal resistance between the cell and the

TEAs. The TEA is a compact device that has a chilled planar surface that allows for a directly thermal coupling to objects to be cooled down. The aluminum metal plate acts like a heat bridge and serves to efficiently conduct the heat between the measuring object and the TEM. The heat sink with the fan serves to transfer the heat to the environment. Three K-type thermocouples are attached to the surface of the cell for measurement of temperature, where two are located near the terminal tabs on one side and the third one is at the center of the back side. The TEAs are powered by a bipolar power supply controlled by the temperature controller. The controller is implemented using LabVIEW, while the thermal model and Kalman filter are coded using MATLAB. The maximum range of measurable HGR is 100W with the measurement temperature range from -30 °C to 35 °C.

Figure 2(b) shows a photo for the calorimeter. In experiments, the calorimeter is placed in a thermal chamber, in which a K-type thermocouple is used to measure the ambient temperature,  $T_{amb}$ . The tested cell is powered using two custom designed clamps as shown in Figure 2(c).

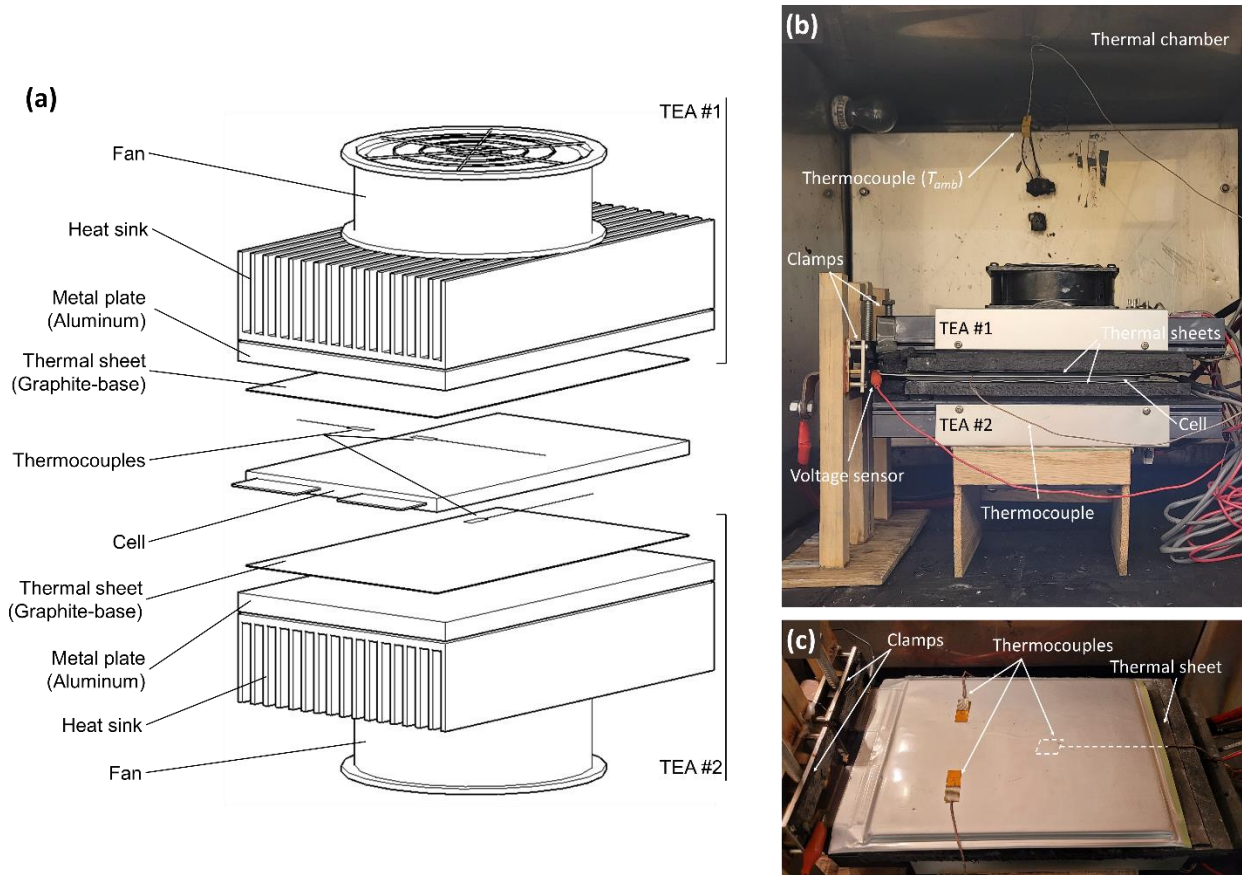


Figure 2. Calorimeter setup: (a) side view of the calorimeter structure, (b) photo of the calorimeter, (c) connection to the clamps and locations of thermocouples.

## 2.3.2 Experimental procedure

### 2.3.2.1 Calibration

For static and dynamic calibration, a printed circuit board (PCB) is designed that has the same dimension as the cell, has a known resistance, and is connected to a voltage controlled current source. The total heat generated in the PCB can be programmed using the current source.

#### (1) Static calibration

The static calibration starts with adjusting the ambient temperature  $T_{amb}$  to the required value,  $T_0$ , and resting for 30 min to get a steady state. Then, a series of pulse currents are applied to the PCB to generate the desired heat generation as an input to the calorimeter, as  $\dot{Q}_{in}$ , which ranged from 0W to 100W. Each current pulse lasts for 10 min to allow the calorimeter to reach an equilibrium state where  $\dot{Q}_{pump} = \dot{Q}_{in}$ , and then was followed by a 10 min rest period. The measurement data  $\dot{Q}_{pump}$ ,  $V_{TEM}$ , and  $T_{amb}$  within the last 1 min of each pulse tests are collected, averaged, and stored.

The calibration should take all the possible conditions at testing into account, such as the boundaries for HGR and ambient temperature fluctuations. Usually, the temperate inside a thermal chamber fluctuates around a set reference. Thus, the calibration is repeated at different set temperatures with a tolerance of  $\pm 2$  °C, where the  $T_0 = -30, -15, 0, 15, 25$  and  $35$  °C. Afterwards, ANN is trained. For an example, at  $T_0 = 25$  °C, the dataset given by the static calibration has 212 patterns, and each pattern includes values of  $T_{amb}$  and  $V_{TEM}$  as an input, and  $\dot{Q}_{pump}$  as an output. The dataset is randomly divided into two separate parts; a training set with 155 patterns and testing set with 57 patterns. The training set is applied to train the ANN using the NBN algorithm. The maximum number of iterations is set to 5000, and the Sum of Square Error (SSE) is calculated as a method to evaluate the training process. The training process is repeated 20 times, and the result with minimum SSE (=0.0051) is selected. Figure 3(a) shows the training result of ANN, where the x and y axis represents the two input values and the color map represents the value of the output. The training result reveals that the cooling power of TEM exhibits a highly nonlinear relationship with respect to the control voltage and ambient temperature.

To evaluate the performance of the trained ANN, the testing set was applied to the ANN model. The heat pump rates predicted by the ANN model are compared with the actual values, which is shown in Figure 3(b). The  $x$  and  $y$  coordinate of the circles denotes the value of  $T_{amb}$  and  $V_{TEM}$ , the color represents the predicted heat pump rates by ANN, and the numbers beside the circles indicate the prediction error. The averaged prediction error for the ANN model is 0.408W.

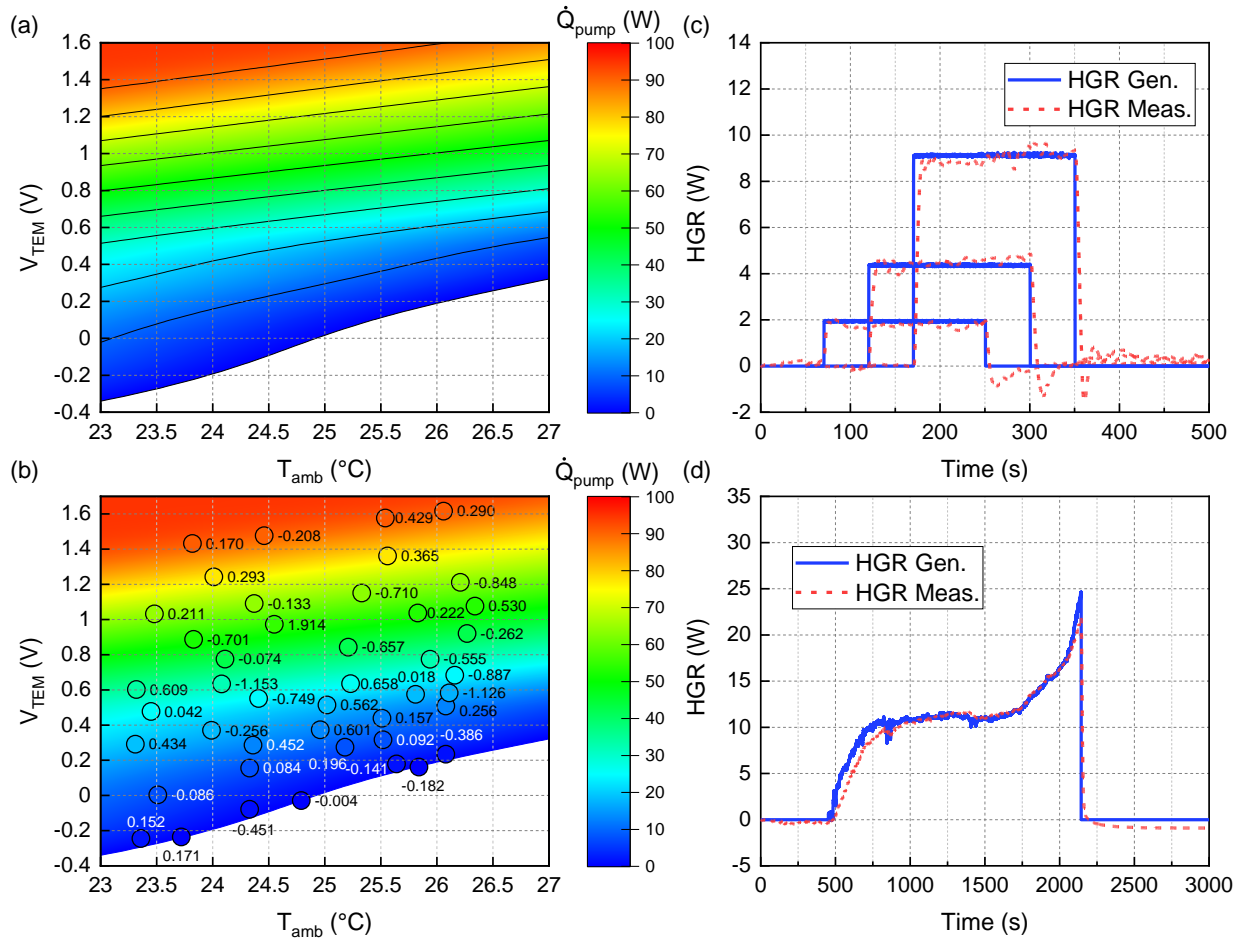


Figure 3. Static calibration results at 25 °C: (a) training result of ANN and (b) performance evaluation. Dynamic calibration results at 25 °C: (c) pulse heat generation profile and (d) discharge heat generation profile.

## (2) Dynamic calibration

Dynamic calibration is carried out using two types of profiles of HGR artificially created by a PCB which include three standard pulse profiles and a discharge profile, as shown in Figure 3(c) and (d) with the solid blue lines. The first one produces 2W, 4.4W and 9W heat generation pulses that last for 3 min. The second one is the similar form of the heat generation profile of a real battery during 2C discharge. These two types of profiles are used to find a set of the parameters of the calorimeter model and Kalman filter with respect to measurement error of the HGR and the time response. The values of the model parameters are set with  $\alpha = 3.2856 \times 10^{-6}$ ,  $k = 20 \text{ Wm}^{-1}\text{K}^{-1}$  and the covariance of Kalman filter are  $Q = 1500$ , and  $R = 10^{-5}$ . The measured HGRs of the calorimeter in Figure 3(c) and (d) with the red dash lines show that the averaged absolute measurement errors of the two cases are 0.46W and 0.67W, respectively, and the time delay is less than 10s.

#### 2.3.2.2 Measurement of HGR

After a cell is placed in the calorimeter and in a thermal chamber, the temperature inside the thermal chamber is set to a value,  $T_0$ , and is held for 30 min before proceeding to allow the system to reach equilibrium. Then, the cell is charged or discharge with a given C-rate (A C-rate is the amplitude of current needed to fully charge or discharge the theoretical maximum capacity in one hour) from an initial state to the end state, and the current, along with the measured voltage, surface temperature, and the HGR are recorded. In addition, the C-rate and the temperature are changed to quantify effects on the HGRs. Tests to determine effects of the C-rates on heat generation are performed at  $T_0=25 \text{ }^\circ\text{C}$ , where cells were charged or discharged with different C-rates in the constant current (CC) mode. The range of SOC considered was varied from 4% to 98% (measured by Coulomb counting method), or until the terminal voltage reached the cutoff voltage of 4.15V and 2.5V, respectively. The C-rates considered for charging and discharging were 1C, 1.5C and 2C and C/3, 0.5C, 1C, 2C, 3C and 4C.

In order to investigate the effects of temperature on the HGR, cells were charged or discharged at 1C within the same operation range, and the temperatures considered were  $T_0=0, 15, 25$  and  $35\text{ }^\circ\text{C}$  for charging and  $T_0=-30, -15, 0, 15, 25$  and  $35\text{ }^\circ\text{C}$  for discharging. Temperatures during charge were kept above  $0\text{ }^\circ\text{C}$  to avoid the occurrence of the lithium plating side reaction, which may have introduced error into the heat generation measurements.

In addition, the HGR of a cell was measured under dynamic driving test cycles at  $25\text{ }^\circ\text{C}$ , where a power profile for 600s provided by the cell manufacturer was used as an example. In the measurement, the cell was fully charged up to 100% SOC at  $25\text{ }^\circ\text{C}$ , and then overall discharged using the ten driving cycles until 15% SOC.

## 2.4 Result and discussion

### 2.4.1 HGR at different C-rates and temperatures

The HGR of the cells were measured under different charge and discharge C-rates and temperatures. For all cases, the maximum averaged surface temperature fluctuation of the cell was less than  $0.3\text{ }^\circ\text{C}$ . Figure 4(a), (b) and (c) show the measurement results as a function of C-rates during charging and discharging at  $25\text{ }^\circ\text{C}$ . The HGR tends to increase as the current increases. In addition, the heat generated during discharging is larger than that seen during the charging, which is caused by the endothermic or exothermic process of the reversible heat. On the other hand, the irreversible heat source is exothermic regardless of operating conditions. As the current increases, the irreversible heat becomes a dominant part of the total heat generated.

Figure 4(d) and (e) show the HGR at various temperatures during 1C charging and discharging. The magnitude of the HGRs is drastically increased when temperature decreases,

which is caused by increased Ohmic and SEI resistances, and the charge transfer resistance due to the decreased mass transport. Thus, when temperatures decrease, the irreversible heat generation increases rapidly.

However, the magnitudes of the HGR at 25 °C and 35 °C are very similar during charging and discharging process, despite the decreased irreversible heat generation. This is due to an increased reversible HGR at high temperature conditions. In addition, the shapes of the HGR responses are also affected by the temperatures. At low temperatures, the HGR increases monotonously. When the cell was charging at 0 °C, the HGR was seen to always be positive, indicating an exothermic process, as shown in Figure 4(d) during charging at 0 °C. However, as temperature increases, the endothermic process is seen to appear at the beginning of the charge, and becoming most prominent at 35 °C. Also in Figure 4(e), as the temperature increases to 35 °C, the shape of the heat generation profile becomes a distinct S type. These phenomena indicates an increased proportion of reversible heat generation as temperature increases, which can be mathematically explained by Eq. (5):

$$\dot{Q}_{total} = \dot{Q}_{rev} + \dot{Q}_{irr} = -I \cdot T \cdot \frac{dU_{oc}}{dT} + I^2 \cdot R \quad (5)$$

,where  $I$ ,  $T$ ,  $\frac{dU_{oc}}{dT}$ , and  $R$  represent the current, temperature, entropy coefficient and internal resistance of the cell.

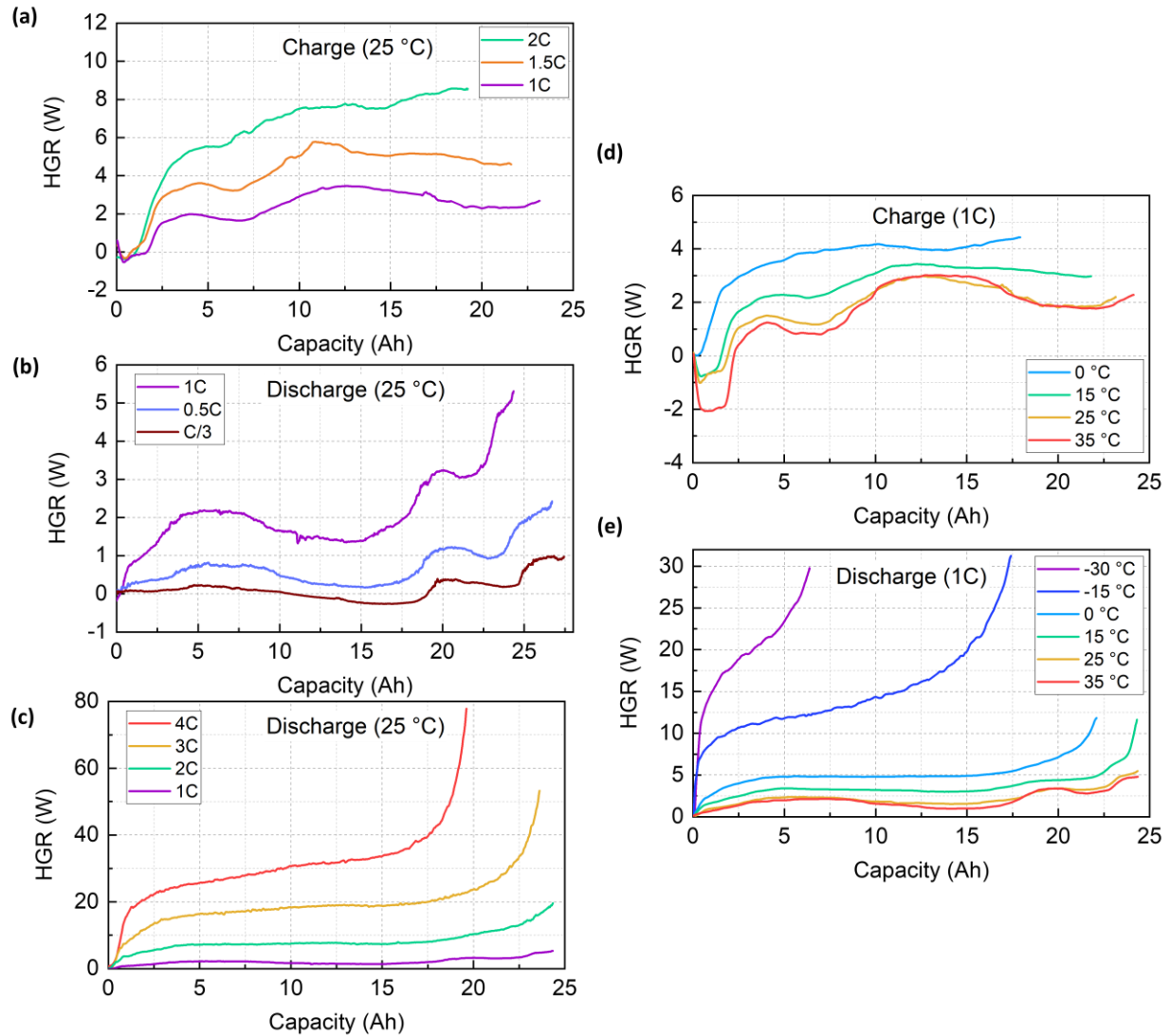


Figure 4. Measurement results of HGRs at different C-rate during (a) charging and (b) (c) discharging at 25 °C, and at different temperatures under 1C (d) charging and (e) discharging.

The measurement results under driving cycles at 25 °C are plotted in Figure 5, where Figure 5(a), (b) and (c) show the applied electric power profile that consists of ten driving cycles, the corresponding SOC depletion and HGR, respectively. The HGR of the cell under driving cycles is relatively low, where the magnitude is generally smaller than 8W in the 100% -15% SOC range. In addition, the overall tendency of the HGR profile shows a V shape at the power profile, where HGR between 70% - 50% SOC is less than those at high or low SOC ranges.

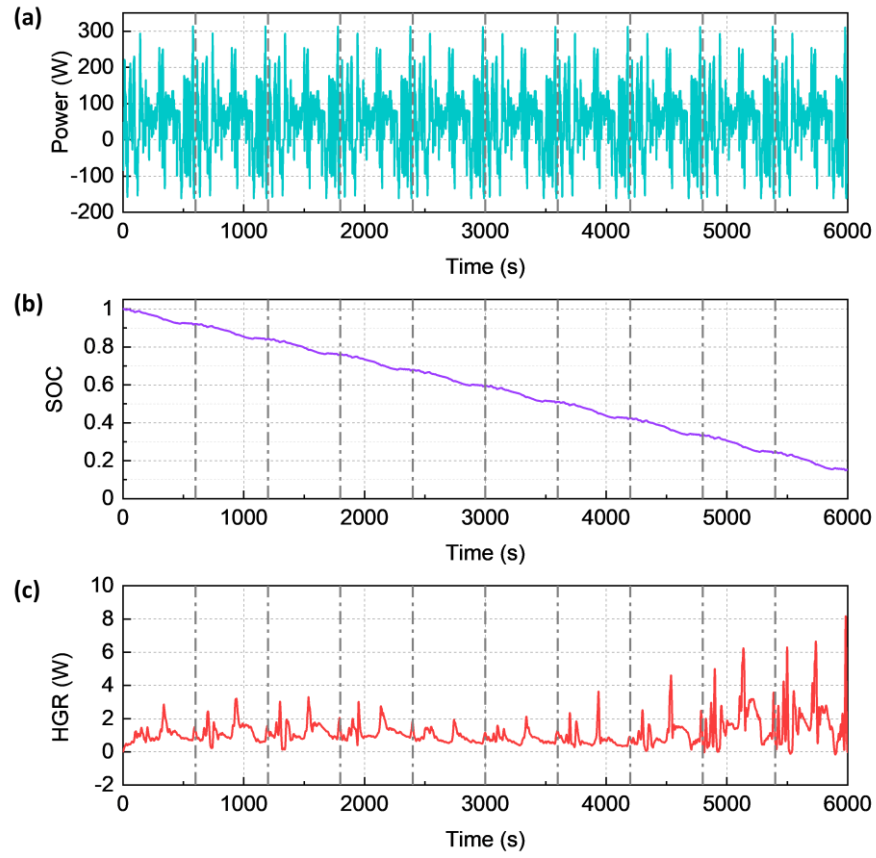


Figure 5. Measurement results under driving cycles at 25 °C: (a) electric power, (b) SOC and (c) HGR.

#### 2.4.2 Analysis of total heat generation and energy efficiency

When battery is charged or discharged, electric energy is converted to chemical energy or vice versa. During this process, heat is generated as an energy loss that affects the energy efficiency of the battery. The energy efficiency can be characterized as a ratio of the heat generation to the total energy input or output during charging or discharging ( $p_{heat}$ ) [18] as follows:

$$P_{heat-ch} = Q_{total} / E_{total-ch} \quad (6)$$

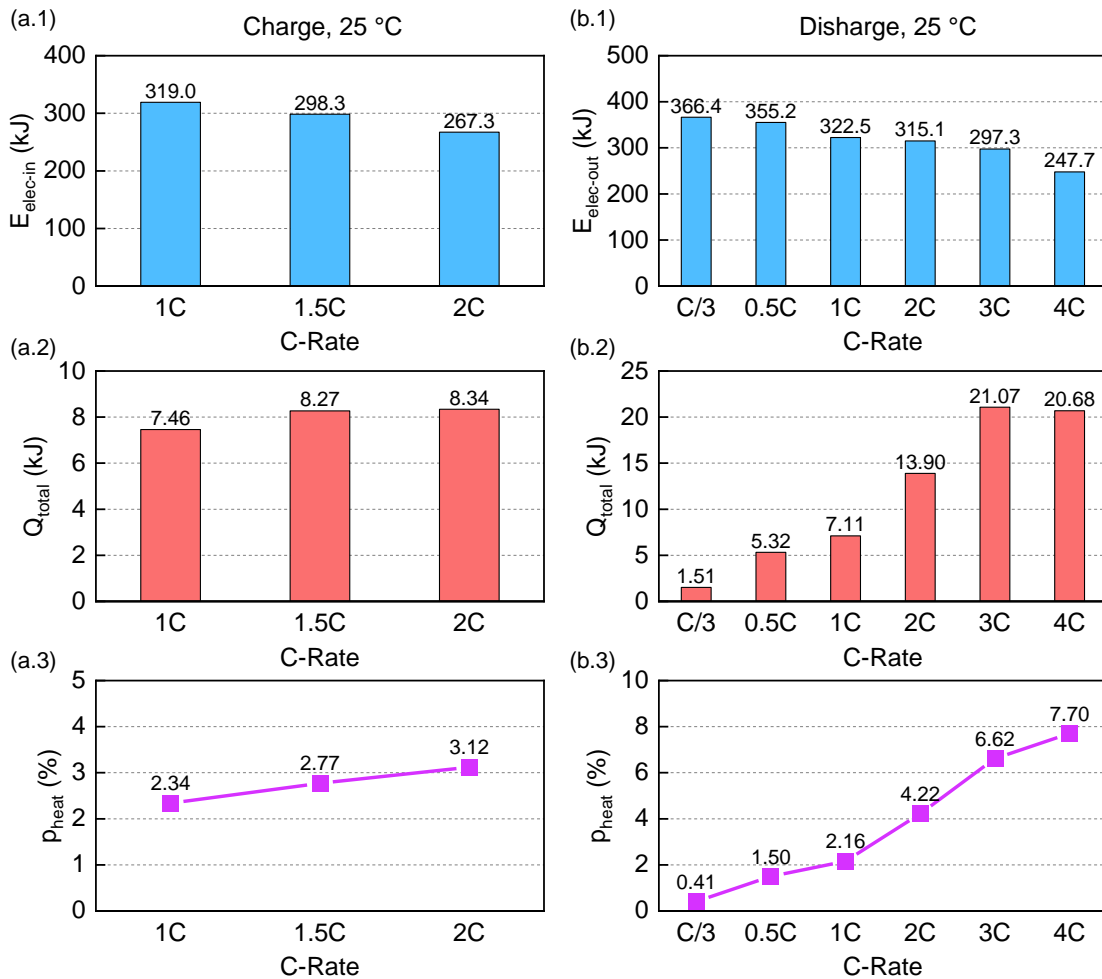
$$P_{heat-dch} = Q_{total} / E_{total-dch} \quad (7)$$

, where  $Q_{total}$  denotes the total heat generation that is calculated by integrating the HGR over time. The term  $E_{total}$  represents the total energy input and output during charging and discharging process. The total input energy during charging ( $E_{total-ch}$ ) is equal to the input electric energy, which is obtained by integrating the power at the terminal over time, while for discharging the total energy output ( $E_{total-dch}$ ) is the sum of the output electric energy and the heat generation.

Figure 6(a) and (b) show a comparison of input/output electric energy, total heat generation, and  $p_{heat}$  at different C-rates at 25 °C. As the C-rate increases, the input and output electric energy of the battery during charging or discharging decreases due to the increased overpotentials. Conversely, the total heat generation increases because of the increased irreversible heat. However, when the cell was discharged at 4C, the total heat generation becomes lower than that at 3C, as shown in Figure 6(b.2). This effect was mainly caused by the reduced discharging time or capacity at high C-rates. In addition,  $p_{heat}$ , as shown in Figure 6(a.3) and (b.3) increases as the C-rate increases, which indicates that the proportion of electrical energy lost due to conversion to waste heat becomes higher at higher C-rates.

Similarly, effects of different operating temperatures are plotted in Figure 6(c) and (d). The amount of the stored electric energy during charging and the released energy during discharging increases as the temperature increases, while the total heat generation decreases when temperature increases from 0 °C to 35 °C for charging, and -15 °C to 35 °C for discharging. The main causes for these phenomena are attributed to the decreased internal resistance. As temperatures increase, overpotentials become smaller and less heat is generated. The total heat generated during 1C discharging at -30 °C was nearly 50% less than that at -15 °C, as shown in Figure 6(d.2). For this

case, the available capacity at  $-30\text{ }^{\circ}\text{C}$  (6.38Ah) is much less than that at  $-15\text{ }^{\circ}\text{C}$  (17.41Ah), which results in a reduced discharge time and less heat generated, even with a higher HGR. Figure 6(c.3) and (d.3) show the relationship between the  $p_{heat}$  and the temperatures. As the temperature decreases, the value of  $p_{heat}$  increases. Thus, a higher percentage of electric energy is dissipated when the operating temperatures are low. In addition, as the subzero temperatures lower,  $p_{heat}$  drastically increases as temperature further decreases, which indicates that energy efficiency of the battery is severely limited in the subzero temperature conditions.



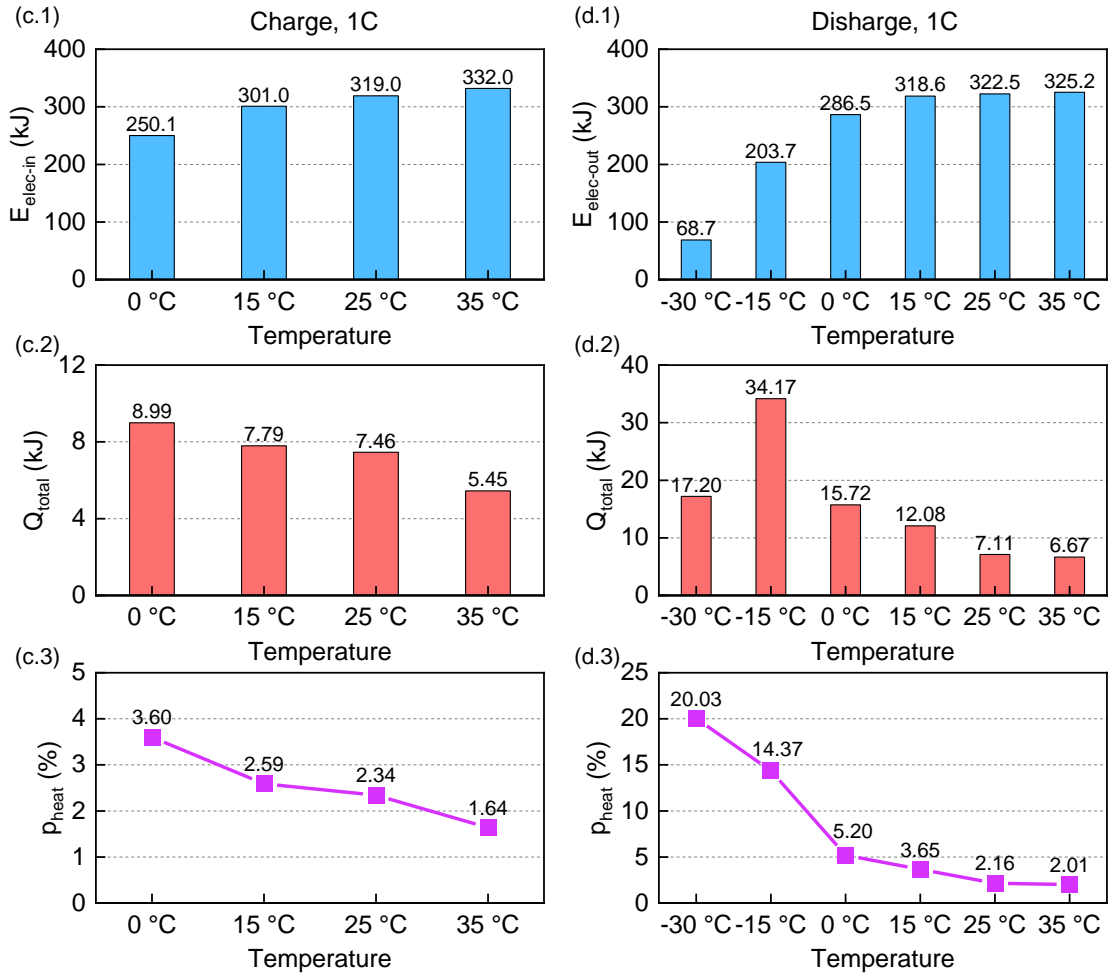


Figure 6. Comparison of input and output electric energy, total heat generated, and the percentage of energy dissipation

## 2.5 Summary

In this section, we present a new calorimeter working as a heat pump in a control loop is developed that enables the measurement of the HGR of large format pouch cell lithium-ion batteries, while simultaneously regulating and measuring the cell temperature and a reference temperature. Procedures needed for static and dynamic calibrations are also developed and successfully implemented. The designed calorimeter is used to measure and analyze the HGR and heat source of a 25.9Ah pouch type LMO-NMC/graphite cell as a function of C-rates, SOCs, and operating temperatures. Here is a summary of the major outcomes:

- Design of an accurate and dynamic isothermal calorimeter with the maximum measurement error of 0.67W and the response time of less than 10s.
- The high C-rates and low temperature affect the irreversible heat generation significantly, while the high temperatures mainly affect the reversible heat generation.
- The percentage of heat-induced energy loss,  $p_{heat}$  increases at high C-rates and low temperatures, indicating that more energy is dissipated.

## Chapter 3. Characterization of heat source terms

### 3.1 Literature review

The heat generated during the operation of lithium-ion batteries is predominantly produced by two heat source terms, reversible heat and irreversible heat. The reversible heat is generated by a change in entropy during the electrochemical reactions and can be estimated using the entropy coefficient. The irreversible heat is caused by the resistances that represent concentration, activation, and Ohmic polarizations.

In order to understand and predict the reversible heat generation of the battery, the cell's entropy coefficient as a function of state of charge (SOC) should be given. Currently, the entropy coefficient for lithium-ion battery is measured using one of two methods: the potentiometric or calorimetric method [28].

The potentiometric method firstly creates an equilibrium state at a given temperature once a cell has been discharged to a specific SOC and then relaxed until a specified condition is reached. Then, the temperature is increased or decreased, and the corresponding change of the terminal voltage is measured. The entropy coefficient is then determined by calculating the slope of the open circuit voltage ( $U_{OC}$ ) vs. temperature ( $T$ ). Even with decent accuracy, the measurement takes a significant amount of time because of the long-lasting relaxation needed to reach equilibration in addition to the limited temperature change rate (TCR), which is usually less than  $0.5^{\circ}\text{C}/\text{min}$  that is required to be within a linear range between  $U_{OC}$  and  $T$  [28] [29]. Depending on electrode chemistries, the measurement time of an entropy coefficient ranges from 10 to 30 hours per SOC point, which results in an overall measurement time on the order of 600 hours [30].

Alternatively, the calorimetric method uses a calorimeter to determine the entropy coefficient. In fact, the calorimeter allows for measurement of the heat generation rate during charging and discharging. If the irreversible heat generation rates during charge and discharge process are assumed to be identical, the reversible heat source term can be obtained from the difference of the measured total heat, and then the entropy coefficient can be determined. Compared to the former method, this method requires significantly less measurement time because the time-consuming relaxation period is not necessary. However, the achievable accuracy is usually lower than that of the potentiometric method because of the inherent inaccuracy of the calorimeter, and meanwhile the measurement result is usually an averaged value within the SOC range during charging and discharging periods [28][28]. In addition, design of an accurate calorimeter is also a challenging issue because of the required calibrations necessary to minimize the effects of the heat generated by heat pump and transient responses as a result of the controls methodology.

Recently, several novel techniques have been proposed that reduce the measurement time for determination of the change of entropy or the entropy coefficient, while maintaining the accuracy of the potentiometric method. One of them is by an electrothermal impedance spectroscopy (ETIS), where a sinusoidal current is applied to a cell and the entropy is estimated by analyzing the corresponding heat generation rates using Fourier transformation (FT) techniques in the frequency domain [31]. This method enables drastic reduction of the measurement time and takes only one hundredth of the time compared to the potentiometric method. However, the heat generation is not directly measured but estimated using a thermal transfer function between the heat generation and the surface temperature of the cell, which requires a significant amount of experiments. The potentiometric method is further improved by applying a background correction

approach [30], where the drift of relaxation voltage after a discharge is identified and removed, which results in a reduced relaxation period. However, the temperature change rate (TCR) for the step excitation of the temperature should be lower than  $0.5^{\circ}\text{C}/\text{min}$ , which prolongs the overall measurement time.

On the other hand, for the prediction of the irreversible heat, the cell's internal resistance as a function of state of charge (SOC) should be known. Currently, the internal resistance of the battery can be measured from V-I characteristics, the EIS technique, as well as hybrid pulse power characterization (HPPC) tests [32]. Among the above methods, the EIS test has been widely used to extract electrochemical impedance of lithium-ion batteries. The internal resistance is a sum of Ohmic resistance, SEI resistance and charge transfer resistance, which is extracted from the experimental data with the help of the EIS equivalent circuit model (EIS-ECM) [33]. The measurements are repeated at different discrete SOC points and the relationship between the internal resistance and SOC is obtained. This method provides relatively accurate measurement results, but needs a long testing time because of the time required to reach each equilibrium at a given SOC point.

Therefore, in this section, we propose several novel experimental techniques that facilitate the fast and accurate characterization of the two thermal parameters, which include (1) accelerated equilibration method, (2) hybridized time-frequency domain analysis (HTFDA) method, and (3) improved frequency-domain calorimetric method, and (4) wavelet-transform based simultaneous and continuous characterization method. The results are compared with those measured by the conventional experimental methods, and show advantages with respect to measurement time and accuracy.

### 3.2 Accelerated equilibration method

In this part, we proposed a new equilibration method for lithium-ion batteries by formulating an optimal time control problem using a single-particle based electrochemical model and solving the problem [34]. Firstly, the electrochemical model of the lithium-ion battery was developed, and validated against the experimental result of a commercial pouch type NMC/Graphite cell. Then, constraints for the formulated optimal time control problem were defined. There are two most important constraints, the evenly distributed concentration of lithium ions in the solid phase, and a target SOC at the end of operation. The cost function includes a minimum time of the operation. The optimal problem is solved by employing the direct method. Finally, an optimal-time current profile was obtained that was tested with the cell. The time to reach an equilibrium was compared with the currently used pulse-relaxation method at different SOCs and temperatures.

#### 3.2.1 Modeling and optimal time control

##### 3.2.1.1 Electrochemical model of lithium-ion battery

The model of the pouch type lithium-ion polymer single cell is approximated by a micro cell that has a sandwich structure with three domains between the two current collectors at the end of each electrodes: a composite anode, a separator, and a composite cathode. The governing equations for the micro cell are listed in Table 1 that describe ion transport and intercalation and deintercalation using the principles of diffusion, mass transport, electrochemical kinetics, and Ohm's laws.

Table 1. Governing equations of lithium-ion battery.

Description	Governing equation
-------------	--------------------

Ion concentration in electrode	$\frac{\partial c_s}{\partial t} = \frac{1}{r^2} \frac{\partial}{\partial r} \left( D_s r^2 \frac{\partial c_s}{\partial r} \right)$ $D_s \frac{\partial c_s}{\partial r} \Big _{r=0} = 0$ $D_s \frac{\partial c_s}{\partial r} \Big _{r=R_s} = -\frac{j^{Li}}{a_s F}$
Ion concentration in electrolyte	$\frac{\partial \varepsilon_e c_e}{\partial t} = \frac{\partial}{\partial x} \left( D_e^{eff} \cdot \frac{\partial c_e}{\partial x} \right) + \frac{1-t_+^0}{F} j^{Li}$ $\frac{\partial c_e}{\partial x} \Big _{x=0} = \frac{\partial c_e}{\partial x} \Big _{x=L} = 0$
Potential in electrode	$\frac{\partial}{\partial x} \left( \sigma^{eff} \frac{\partial \phi_s}{\partial x} \right) - j^{Li} = 0$ $-\sigma^{eff} \frac{\partial \phi_s}{\partial x} \Big _{x=0} = \sigma^{eff} \frac{\partial \phi_s}{\partial x} \Big _{x=L} = \frac{I}{A}$ $\frac{\partial \phi_s}{\partial x} \Big _{x=L_n} = \frac{\partial \phi_s}{\partial x} \Big _{x=L_n+L_s} = 0$
Potential in electrolyte	$\frac{\partial}{\partial x} \left( \kappa^{eff} \frac{\partial \phi_e}{\partial x} \right) + \frac{\partial}{\partial x} \left( \kappa_D^{eff} \frac{\partial \ln c_e}{\partial x} \right) + j^{Li} = 0$ $\frac{\partial \phi_e}{\partial x} \Big _{x=0} = \frac{\partial \phi_e}{\partial x} \Big _{x=L} = 0$
Butler-Volmer equation	$j^{Li} = a_s i_0 \left\{ \exp \left[ \frac{\alpha_a F}{RT} \eta \right] - \exp \left[ -\frac{\alpha_c F}{RT} \eta \right] \right\}$ $\eta = \phi_s - \phi_e - U$ $i_0 = k (c_e)^{\alpha_a} (c_{s,max} - c_{s,surf})^{\alpha_a} (c_{s,surf})^{\alpha_c}$

In this study, the electrode of the cell is simplified with the single particle model (SPM) scheme [35], which rests on two main assumptions that (1) each electrode is approximated as a

spherical particle where the intercalation and deintercalation of lithium ions take place and (2) the volume current density maintains uniformly distributed in each domain. The schematic diagram of the model setup is shown in Figure 7.

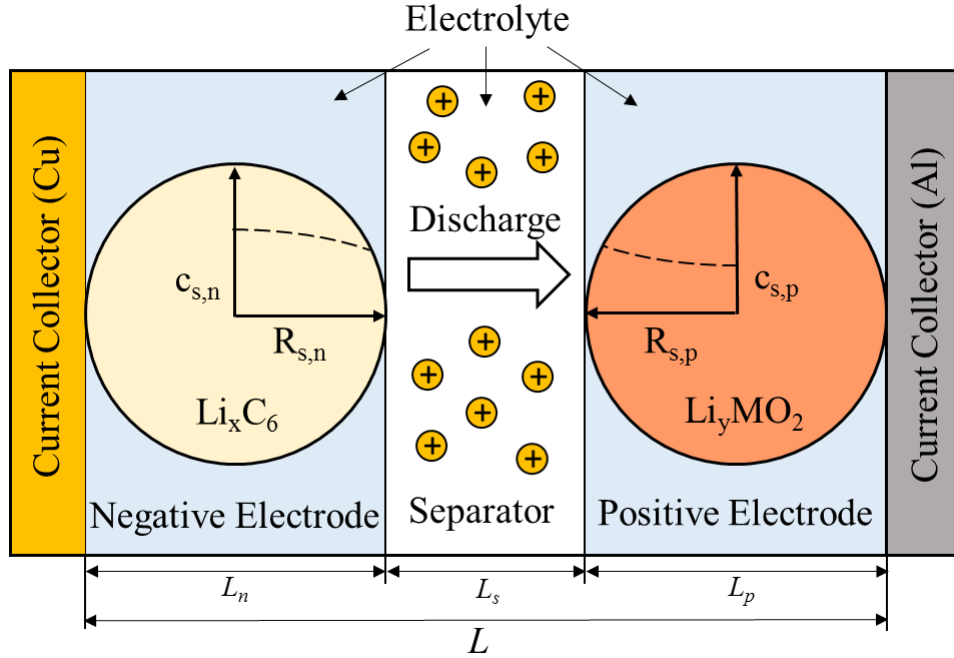


Figure 7. Schematic diagram of the model setup.

The model is solved using the following approaches: (1) the solid-state concentration along the radial direction of the particle is numerically solved by finite difference method, (2) the ion concentration of electrolyte is approximated using residual grouping method [36], and (3) Butler-Volmer equation is linearized by applying Taylor expansion.

### 3.2.1.2 Optimal time control problem

Optimal control techniques provide a powerful tool that facilitates an optimal control performance through minimization of a cost function of the system. In this study, our goal is to find an appropriate current profile that minimizes the time to get to an equilibrium state when

changing a cell to a target SOC from an initial SOC. Consequently, an optimal time control problem was formulated based on the electrochemical model of the lithium-ion battery. The objective function for minimizing the final time  $t_f$  is given as follows:

$$\min_{I(t)} J = \int_0^{t_f} 1 dt = t_f \quad (8)$$

In fact, relaxation process of a cell is mainly attributed to the assimilation processes of lithium ions in the solid phase[37]. Thus, the ion concentration in the solid,  $c_s(r,t)$  should be imposed with a constraint. At the steady state, it remains constant along the radial direction of particles in both electrodes. The equilibrium state of the cell is ensured by constraint #1 as follows:

$$\begin{aligned} \max_{r=0,\dots,R_{s,n}} c_{s,n}(r,t_f) - \min_{r=0,\dots,R_{s,n}} c_{s,n}(r,t_f) &< \varepsilon_1, \\ \max_{r=0,\dots,R_{s,p}} c_{s,p}(r,t_f) - \min_{r=0,\dots,R_{s,p}} c_{s,p}(r,t_f) &< \varepsilon_2 \end{aligned} \quad (9)$$

, where  $\varepsilon_1$  and  $\varepsilon_2$  represent the error tolerance.

Constraint #2 is imposed to ensure the end SOC of the cell meets the target value. SOC is defined as a ratio of the releasable charge capacity to the maximum charge capacity ( $Q_{max}$ ), which can be expressed using the averaged lithium ions concentration within the solid phase in the electrochemical model:

$$SOC = SOC^0 - \frac{\int_0^t I(\tau) d\tau}{Q_{max}} \times 100\% = \frac{\theta - \theta_{0\%}}{\theta_{100\%} - \theta_{0\%}} \times 100\% \quad (10)$$

, where  $SOC^0$  denotes initial SOC,  $\theta = c_{s,ave}/c_{s,max}$  and the subscript of 100% or 0% denotes the states where battery is fully charged (100% SOC) or discharged (0% SOC). From Eq.(10), the  $c_{s,ave}$  at a target SOC (denotes as  $SOC^*$ ) is expressed as:

$$c_{s,ave}(SOC^*) = c_{s,max} \left[ \theta_{0\%} + SOC^* (\theta_{100\%} - \theta_{0\%}) \right] \quad (11)$$

Thus, the state constraint #2 is imposed by:

$$\begin{aligned} \max_{r=0,\dots,R_{s,n}} c_{s,n}(r, t_f) + \min_{r=0,\dots,R_{s,n}} c_{s,n}(r, t_f) &= 2c_{s,ave,n}(SOC^*) \\ \max_{r=0,\dots,R_{s,p}} c_{s,p}(r, t_f) + \min_{r=0,\dots,R_{s,p}} c_{s,p}(r, t_f) &= 2c_{s,ave,p}(SOC^*) \end{aligned} \quad (12)$$

In addition, the initial solid phase concentration, output terminal voltage, SOC range and the input current limit are considered as other constraints:

$$c_{s,n}(r, 0) = c_{s,ave,n}(SOC^0), \quad (13)$$

$$c_{s,p}(r, 0) = c_{s,ave,p}(SOC^0),$$

$$V_{t,min} \leq V_t(t) \leq V_{t,max}, \quad (14)$$

$$SOC_{min} \leq SOC(t) \leq SOC_{max}, \quad (15)$$

$$I_{min} \leq I(t) \leq I_{max}. \quad (16)$$

A direct solution approach is selected to solve the optimal control problem. The direct method allows the optimal control problem to formulate as a nonlinear programming problem (NPL), where the state and control variable are approximated by a piecewise constant

parameterization [38] [39]. For this case, the input current  $I(t)$  is parameterized by a sequence of constant current input,  $I_i$ , with a fixed time interval. Then, the MATLAB's built-in *fmincon* function is used to obtain the optimal  $I_i$  values.

### 3.2.2 Model validation and simulation analysis

#### 3.2.2.1 Model validation

The electrochemical model with single particle scheme is developed and experimentally validated. The cells used for experiments is a large format pouch type NMC622/Graphite lithium-ion energy cell with following key specifications:

- Active materials:  $\text{Li}[\text{Ni}_{0.6}\text{Mn}_{0.2}\text{Co}_{0.2}]\text{O}_2$  for cathode and graphite for anode,
- Nominal capacity: 58Ah,
- Maximum continuous charge and discharge current: 19.3A (C/3),
- End-of-charge voltage, current: 4.2V, 3A,
- End-of-discharge voltage: 2.5V,
- Dimension: 99.7mm×301.5mm×13.2mm.

The tested cell was placed in a multifunctional calorimeter [24] that actively controls the cell's temperature at a set value of 25°C. The cell is charged and discharged with constant current at C/3 rate, which corresponds to the maximum applicable continuous charge and discharge current. The values of the parameters used for validation were listed in Table 2. Experimental and simulated terminal voltages are plotted in Figure 8 for comparison, where the voltage responses

are in a good match with the experimental data. The root-mean-square error (RMSE) of the voltage for charging and discharging are 0.021V and 0.044V, respectively.

Table 2. Parameters for lithium-ion cell electrochemical model at 25°C

Parameter	Negative electrode	Separator	Positive electrode	Unit
$A$	18637		18637	$\text{cm}^2$
$\delta$	$8.40 \times 10^{-3}$		$7.75 \times 10^{-3}$	cm
$R_s$	$1.745 \times 10^{-3}$		$1.073 \times 10^{-3}$	cm
$\varepsilon_s$	0.703		0.675	
$\varepsilon_p$	0.247	0.5	0.243	
$c_{s,max}$	0.031		0.050	$\text{mol cm}^{-3}$
$c_e$	0.012	0.012	0.012	$\text{mol cm}^{-3}$
$D_s$	$2.5 \times 10^{-10}$		$2.0 \times 10^{-10}$	$\text{cm}^2 \text{s}^{-1}$
$D_e$	$2.0 \times 10^{-6}$	$2.0 \times 10^{-6}$	$2.0 \times 10^{-6}$	$\text{cm}^2 \text{s}^{-1}$
$\sigma$	1		0.01	$\text{S cm}^{-1}$
$\kappa$	0.057	0.057	0.057	$\text{S cm}^{-1}$
$\alpha_a, \alpha_c$	0.5		0.5	
$k$	12.9		6.28	$(\text{A cm}^{-2})(\text{cm}^3 \text{mol}^{-1})^{1.5}$
$R_c$	$1.60 \times 10^{-3}$		$1.60 \times 10^{-3}$	$\Omega$
$Q_{max}$		60.5		Ah

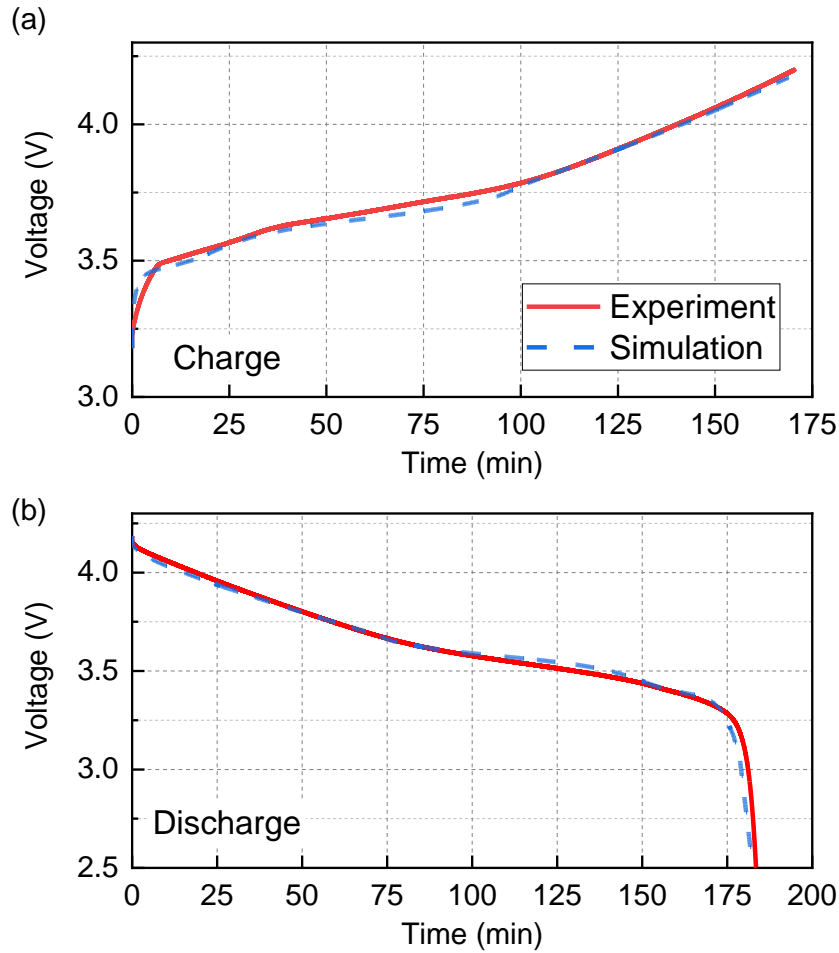


Figure 8. Model validation by comparison between experimental and simulated terminal voltage at C/3 (a) charge and (b) discharge at 25°C.

### 3.2.2.2 Simulation analysis

The performance of a typical pulse-relaxation profile and a proposed optimal-time current profile is compared and analyzed using the validated model. As an example at 25°C, the initial and target SOC are set to 0.497 and 0.447, and the maximum current is limited to  $\pm C/3$  ( $\pm 19.3A$ ) for the two profiles.

#### (1) Pulse-relaxation (PR) profile

The pulse-relaxation profile is the simplest and most widely used method, where the constant current charge or discharge pulse is applied to set the cell to a target SOC and followed with a resting period for equilibration. When C/3 discharge is applied for 9 minutes and rested for 50 minutes, the current and corresponding SOC change, and the variation of the terminal voltage was plotted in Figure 9 (a) and (b).

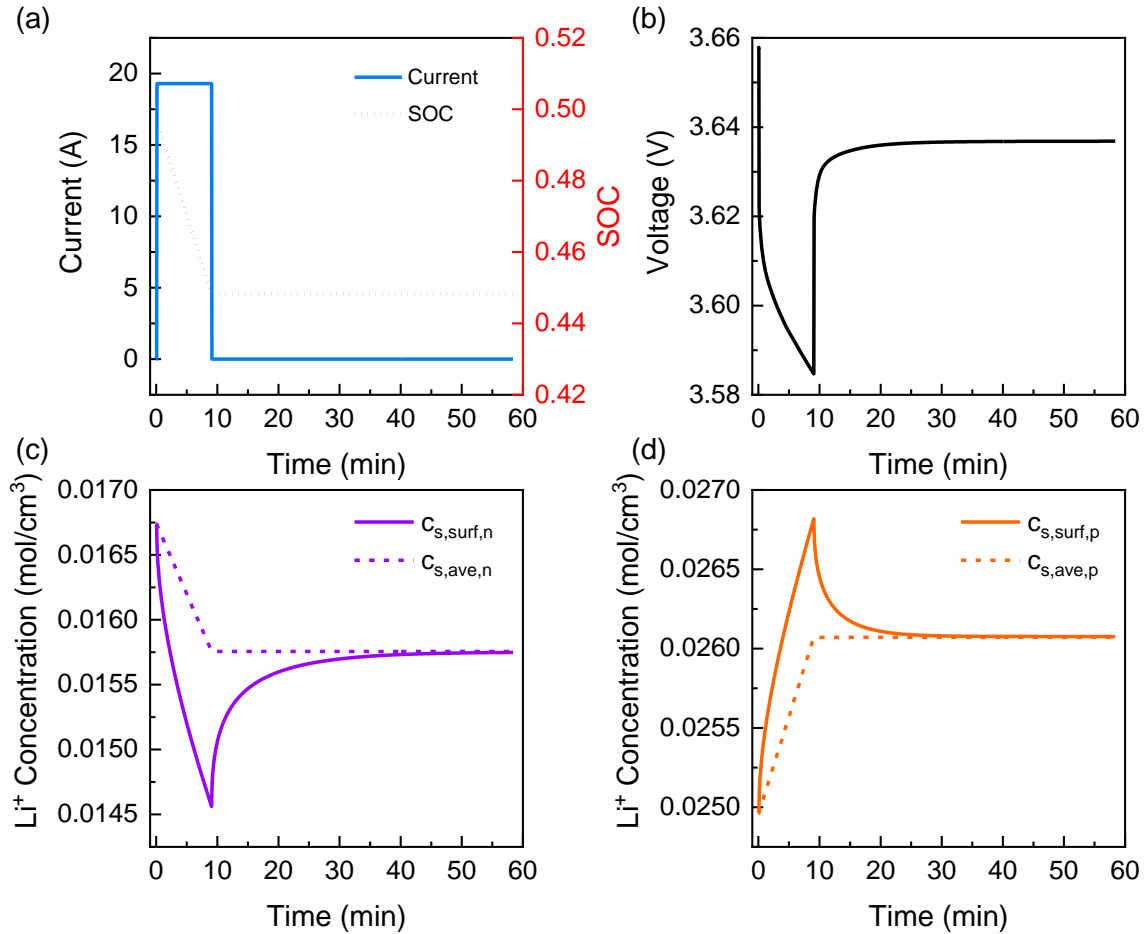


Figure 9. Pulse-relaxation for equilibration. (a) Current profile along with SOC, (b) terminal voltage, (c) and (d) average and surface concentration of lithium ion in negative and positive electrode particles.

The voltage firstly responds with a quick drop due to the Ohmic and charge transfer resistance, and then slowly decreases due to the transport of lithium ions in the solid phase. When

the discharging process stops, the voltage increases as the lithium-ion concentration becomes evenly distributed throughout the solid phase and reaches a steady state. This can be seen more obviously in the response of the surface and average concentration variation in anode and cathode particles, as shown in Figure 9 (c) and (d). At the end of discharge, there was a large difference between the surface and average concentration, which is reduced by ion flows during the resting period, where the surface concentration gradually approaches to the average value. The relaxation process has taken more than 50 minutes to reach the equilibrium state. Moreover, the equilibration process in anode is observable to be longer than in cathode because of the relatively large radius of the particle in anode, which indicates that the long-lasting relaxation time by the pulse-relaxation profile is mainly caused by redistribution of the lithium ions in anode.

## (2) Optimal-time current (OC) profile

The optimal current profile was obtained by solving the optimal time control problem, with the state and input bounds specified as:

$$\begin{aligned}
 SOC^0 &= 0.497, SOC^* = 0.447, \\
 V_{t,\min} &= 2.5V, V_{t,\max} = 4.2V, \\
 SOC_{\min} &= 0, SOC_{\max} = 1, \\
 I_{\min} &= -19.3A, I_{\max} = 19.3A.
 \end{aligned}$$

The resulting current profile along with SOC, terminal voltage, the surface and average concentration in solid phases are plotted in Figure 10 (a), (b), (c) and (d). The current profile consists of six consecutive discharge and charge pulses, which is basically similar to the bang-bang controls. The first five pulses used the maximum discharge/charge current, while the last one did a 10-second peak pulse charge with the magnitude of 12.5A. At the end of the pulses, the cell's

SOC was reached the target value. In addition, at the end of the applied optimal current profile, the terminal voltage does not change over time. Meantime, the surface concentration reaches the average value for both anode and cathode and remains constant. This indicates that the cell reached an equilibrium state with no need for relaxation. Simulation results have shown that the time needed for the OC profile was 28.3 minutes, which reduces 53% of the time taken by the traditional PR process.

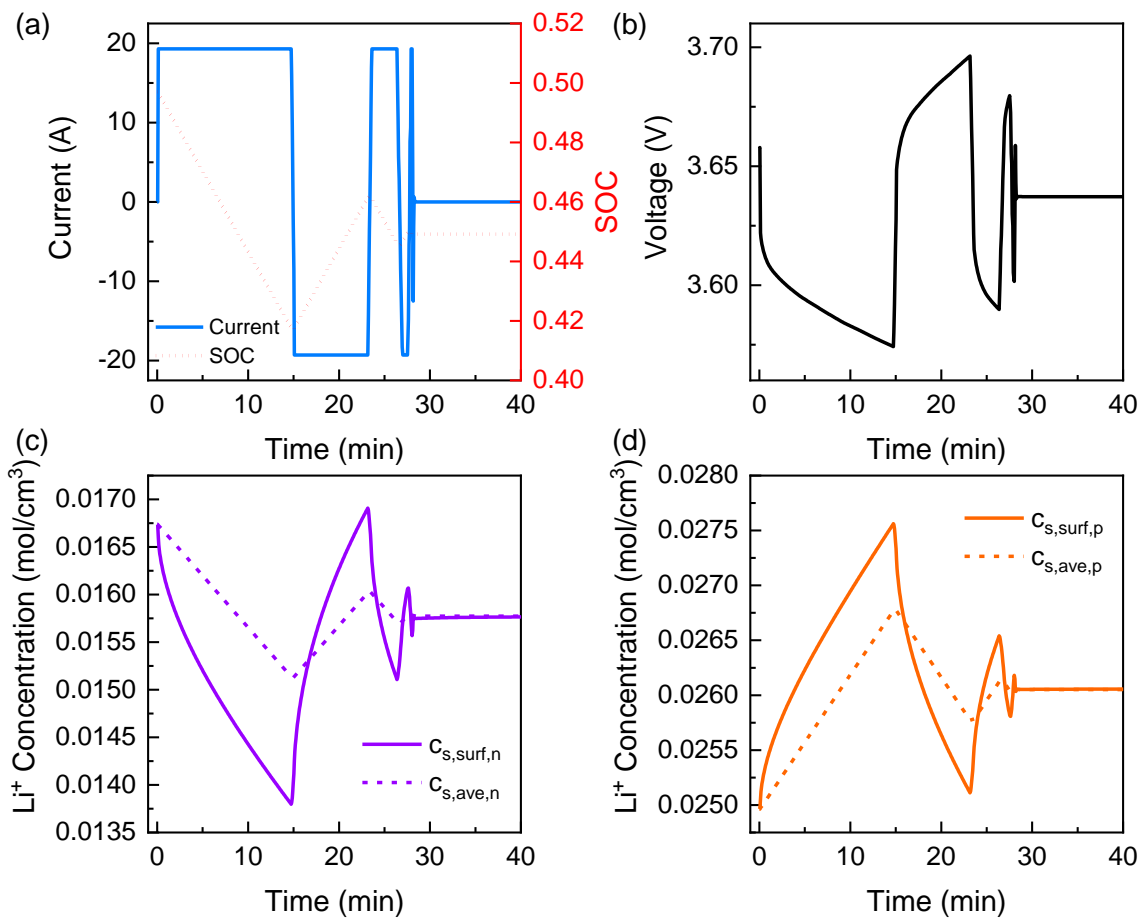


Figure 10. Optimal-time current profile for equilibration. (a) Current profile along with SOC, (b) terminal voltage, (c) and (d) average and surface concentration of lithium ion in negative and positive electrode particles.

The evolution of lithium-ion concentration along the radial direction in anode and cathode particles at different times is plotted in Figure 11 (a) and (b), respectively. Initially, the cell is at the equilibrium state, and there are no concentration gradient at anode and cathode. During the first pulse discharge, the lithium-ion concentration begins to decrease in anode and at the same time increase in cathode, where a rapid change of the concentration takes place at the surface. At the end of the first pulse discharge ( $t = 14.7$  min), a steep concentration gradient is formed within the solid phase. Then, a pulse charge enables equalization of the lithium-ion distribution. Each of the following pulse actions helps reduce the concentration gradient to some extent, and at the end of the current profile,  $t = 28.3$  min, the concentration gradient both in anode and cathode becomes negligible, which implies that the cell finds itself in the equilibrium state.

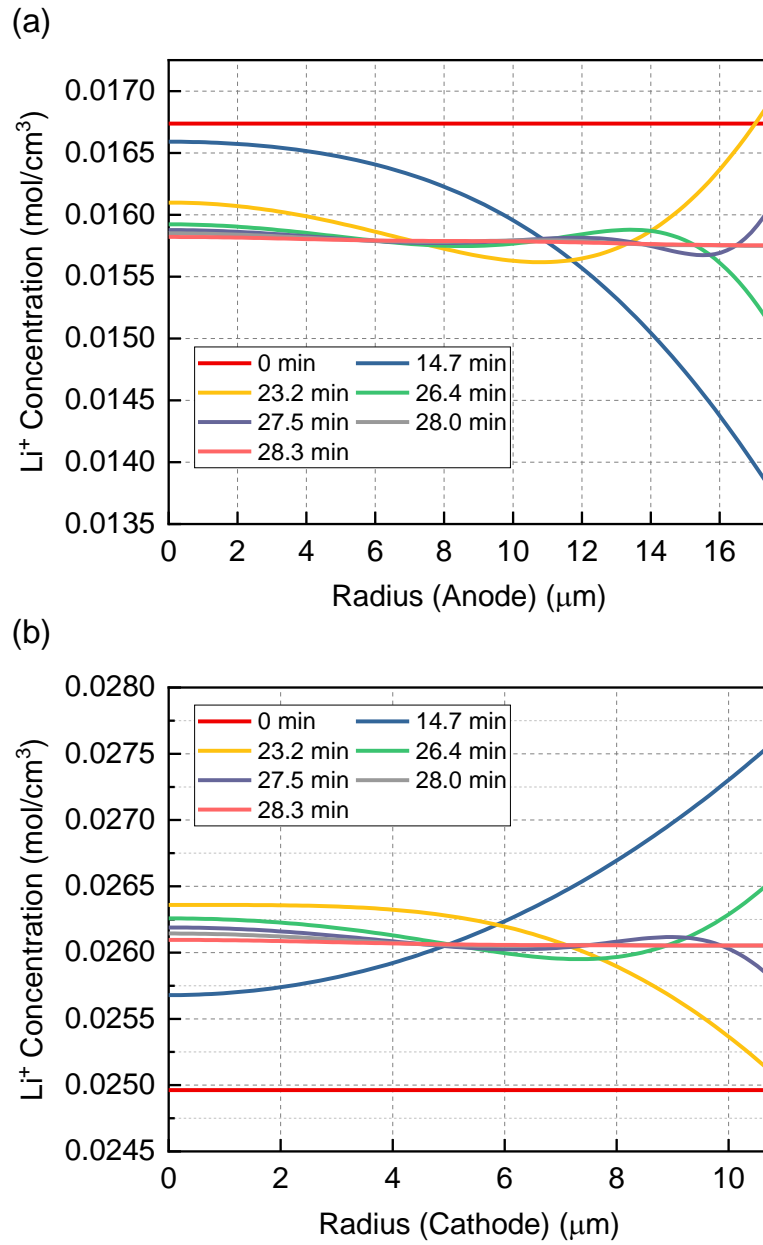


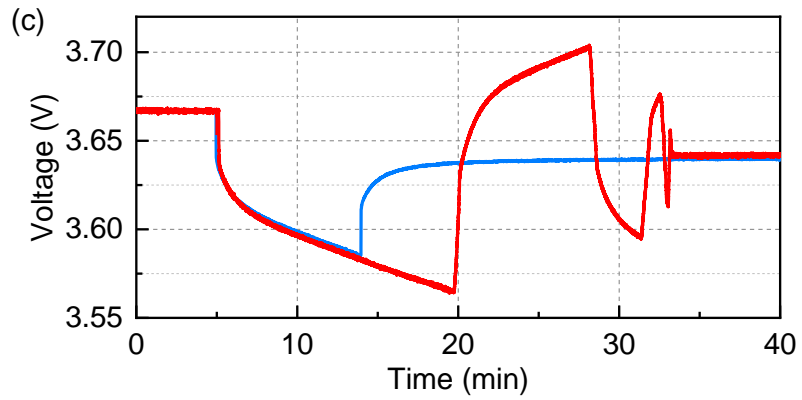
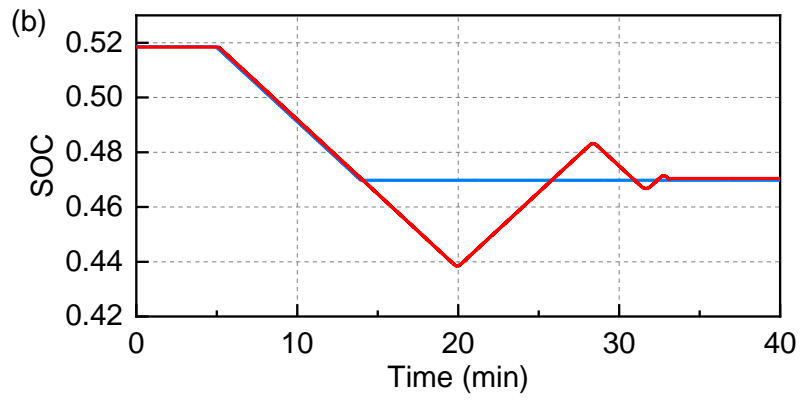
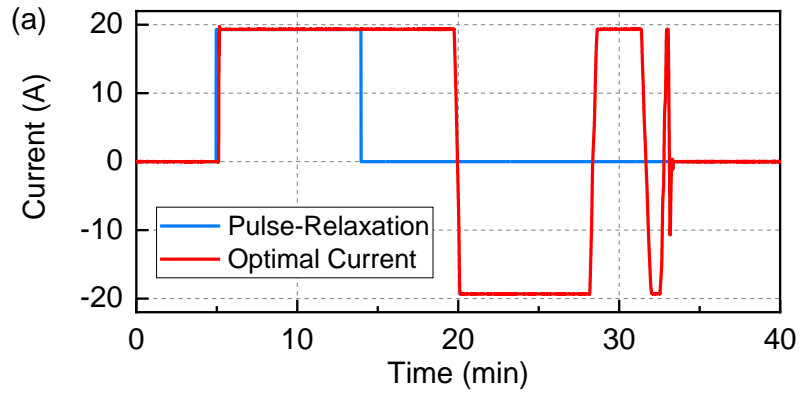
Figure 11. Simulation result of solid phase lithium ion concentration distribution along the radial direction in (a) anode and (b) cathode.

### 3.2.3 Experimental result and discussion

For evaluation of the performance of the proposed method, the PR profile and the OC profile were implemented in a test station with a capability of battery-in-the-loop and applied to the aforementioned cell at 25°C. The maximum current for charge and discharge was limited to  $C/3$  in order to minimize any potential degradation of the cell. The initial SOC was 51.8%, and the target SOC was set to 46.8%, which corresponds to a 5% SOC decrement. The current profile, corresponding SOC variation, and the terminal voltage are plotted in Figure 12 (a) ~ (c).

For the PR test, the cell was discharged with  $C/3$  for 9 minutes and then the SOC was set to the target value. Conversely, it took three times more time for the optimal-time current profile to reach the target SOC. This extra time was consumed to reach the equilibrium state of the ion concentration within the particles, which can be seen in the SOC trajectory fluctuating by approaching the target value, as shown in Figure 12 (b). For the PR test, the cell was at a non-equilibrium state after the pulse discharge, where a steep concentration gradient of lithium ions was formed within the solid phase, which indicates that a long relaxation time will take. On the other hand, since the potential in solid phase is determined by the surface concentration of lithium ions, the terminal voltage tends to slowly change along with the redistribution of the lithium ions. Figure 12 (c) compares the terminal voltage for the two cases.

For PR profile, when the current becomes zero, the voltage firstly shows an immediate increase due to the Ohmic and charge transfer resistance, and then increases in an exponential decaying pattern due to the transport of lithium ions in the solid phase. On the other hand, the OC profile ensures a uniform distribution of lithium ions at the end, thus no apparent voltage relaxation is observed during the resting.



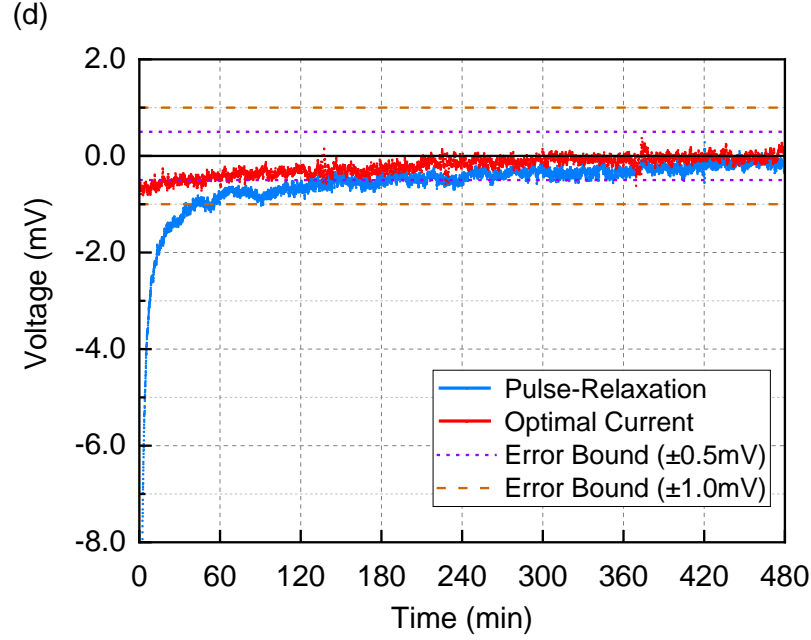


Figure 12. Comparison of experimental results by pulse-relaxation profile and the optimal-time current profile at around 50% SOC, 25°C: (a) current profile, (b) SOC variation, (c) terminal voltage, and (d) voltage difference between the relaxation voltage and OCV.

Figure 12 (d) gives a zoom-in view of the voltage difference between the relaxation voltage and the OCV, which was measured after the 10-hour relaxation, where the starting time of the resting period was set as zero. In addition, two different error bounds were specified: (1)  $\pm 1\text{mV}$ , applicable for the measurement with moderate demand of the equilibrium condition, such as the OCV test [40]; (2)  $\pm 0.5\text{mV}$ , applicable for the tests that require a high-level equilibrium state, such as the measurement of entropy coefficient [30] and EIS analysis [37].

At the end of the OC profile, the terminal voltage fluctuates within the  $\pm 1\text{mV}$  error bound of the OCV, and it takes 34 minutes to reach the  $\pm 0.5\text{mV}$  error bound. The extra voltage relaxation indicates that the cell is not at the perfect equilibrium state after applying OC profile, which is caused by the model error, inner temperature change during the operation and so on. Conversely,

for PR profile, it takes 55 minutes and 140.5 minutes for the voltage to be relaxed to reach the same level of equilibration.

The total time for the two profiles, calculated as a sum of the time for charge and discharge processes and the time for relaxation, are summarized in Table 3. With the given  $\pm 1\text{mV}$  error bound, the OC profile reduces 55.8% compared to that of the PR profile. To reach the  $\pm 0.5\text{mV}$  level of the equilibration, the OC profile can reduce the total testing time by 58.3%. In addition, the tests aforementioned are repeated with two more identical battery cells. The average percentage of saved time by OC than PR is 43.8% and 50.8% at  $\pm 1\text{mV}$  and  $\pm 0.5\text{mV}$  error bound, respectively.

Table 3. Time cost for two profiles at 50% SOC at 25°C.

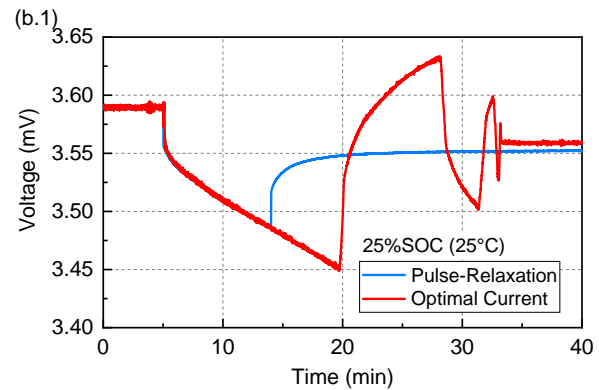
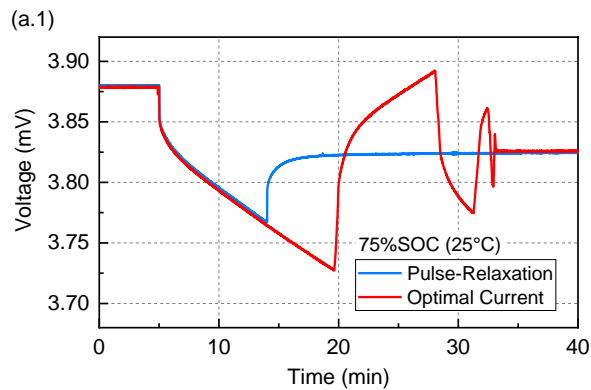
Type	Testing time (min)			Percentage of saved time
	Charge/Discharge	Relaxation	Total	
PR ( $\pm 1\text{mV}$ )	9	55	64	55.8%
OC ( $\pm 1\text{mV}$ )	28.3	0	28.3	
PR ( $\pm 0.5\text{mV}$ )	9	140.5	149.5	58.3%
OC ( $\pm 0.5\text{mV}$ )	28.3	34	62.3	

### 3.2.3.1 Effects of different SOC's

The optimal time control problem is formulated based on the battery model to minimize the concentration gradients in both electrodes. In fact, the model used for the calculation of OC profile at around 50% SOC and 25°C was validated from 0% to 100% SOC, and the parameters such as  $R_s$ ,  $c_{s,max}$  and  $D_s$  are assumed to be constant at different SOC's. Under this assumption, the concentration gradients and the diffusion velocity should be very similar, except for a shift in the magnitude of ion concentration at the applied same current load to the cell at different SOC's. Thus,

theoretically, the obtained OC profile should work at different SOC levels except for those near 0% and 100% SOC, where the terminal voltage may exceed the cutoff voltage during operations.

Experimental verifications were conducted at around 75% and 25% SOC. Initially, the cells were set at 75% and 25% SOC, and rested for 12 hours at 25°C. Then, both OC and PR profiles are applied to the cell to compare each other, which results in a 5% SOC decrease. Figure 13 (a.1)-(b.1) and (a.2)-(b.2) show the terminal voltage behaviors and a zoom-in view of the voltage difference between the relaxation voltage and the OCV, respectively. As shown, the deviation of the terminal voltage to the OCV by the OC profile is much smaller than that by the PR profile, resulting in an even fast transition to reach the equilibrium state. Table 4 summarizes the total time cost taken by the two profiles. The OC profile saves 33.1% ~ 45.2% of testing time than that of PR profile at 25% and 75% SOC.



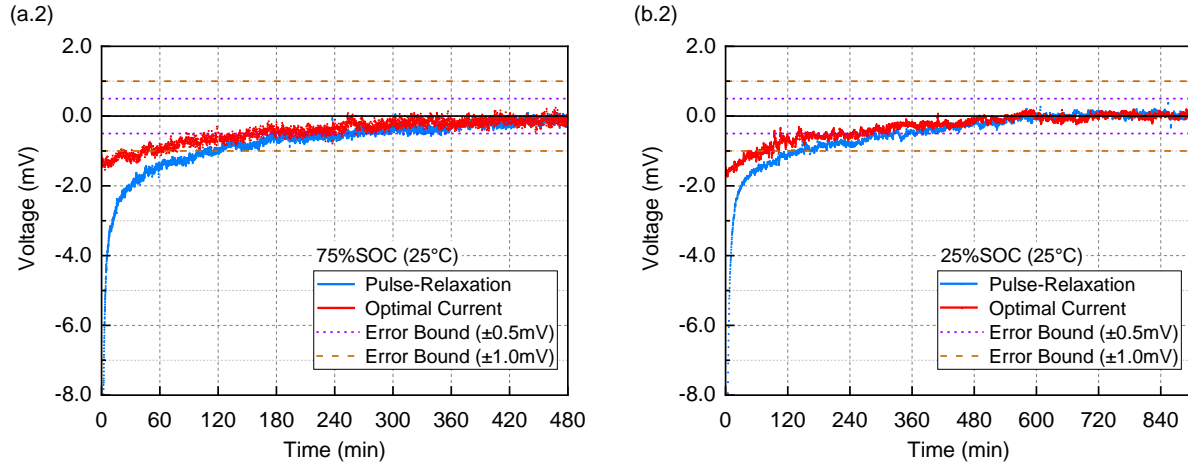


Figure 13. Comparison of experimental results by pulse-relaxation profile and the optimal-time current profile at 25°C: (a.1, b.1) terminal voltage, and (a.2, b.2) voltage difference between the relaxation voltage and OCV at around 75% SOC and 25% SOC, respectively.

Table 4. Time cost for two profiles at 75% and 25% SOC at 25°C.

SOC	Type	Testing time (min)			Percentage of saved time
		Charge/Discharge	Relaxation	Total	
75%	PR ( $\pm 1\text{mV}$ )	9	123	132	45.2%
	OC ( $\pm 1\text{mV}$ )	28.3	44	72.3	
	PR ( $\pm 0.5\text{mV}$ )	9	262	271	33.1%
	OC ( $\pm 0.5\text{mV}$ )	28.3	153	181.3	
25%	PR ( $\pm 1\text{mV}$ )	9	152	161	41.4%
	OC ( $\pm 1\text{mV}$ )	28.3	66	94.3	
	PR ( $\pm 0.5\text{mV}$ )	9	370	379	33.2%
	OC ( $\pm 0.5\text{mV}$ )	28.3	225	253.3	

### 3.2.3.2 Effect of different temperatures

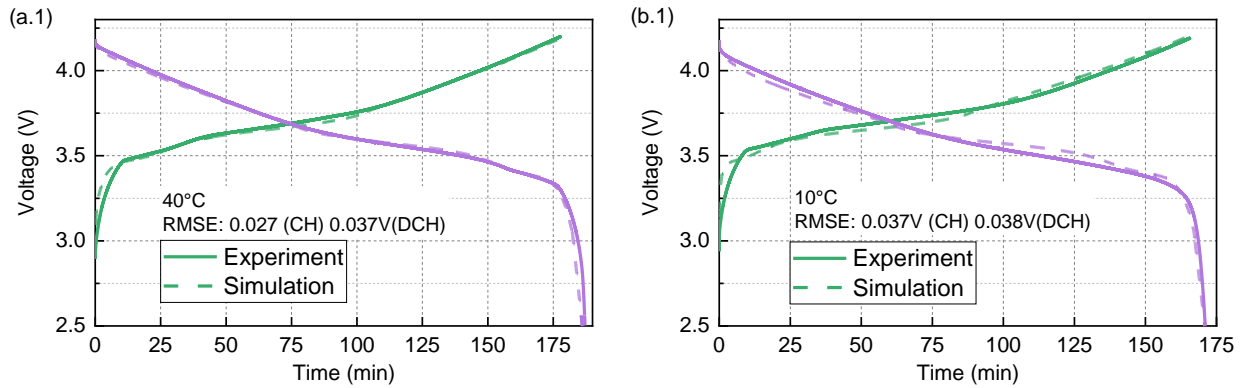
Firstly, the battery model is validated against the experimental data at the two different temperatures. The proposed method using the model is implemented and experimentally tested at 40°C and 10°C. The multifunctional calorimeter is used to control the cell's surface temperature at 40°C and 10°C, respectively, while the cell is being charged and discharged with a constant current at C/3 rate. Since the solid phase concentration dominantly determines the relaxation process, only the diffusivity of the solid phase is regarded as a function of temperature. The updated lithium-ion diffusivities in anode and cathode particles are  $1.50 \times 10^{-9} \text{ cm}^2 \text{ s}^{-1}$  and  $1.60 \times 10^{-10} \text{ cm}^2 \text{ s}^{-1}$  at 40°C;  $2.25 \times 10^{-10} \text{ cm}^2 \text{ s}^{-1}$  and  $7.30 \times 10^{-11} \text{ cm}^2 \text{ s}^{-1}$  at 10°C. Figure 14 (a.1) and (b.1) show the experimental and simulated terminal voltages at 40°C and 10°C, respectively, and the corresponding RMSE, where the voltage responses are in a good match with the experimental data.

Then, similar to the previous case, optimal time control problems were formulated based on the validated model and solved to obtain the OC profiles, which are so designed that 5% SOC gets decreased.

In order to evaluate the performance of the OC profile, the tested cell was initially set at around 52% SOC and rested for 12 hours at the preset temperature to reach an equilibrium state. Current profiles for OC method with red solid line and PR methods with blue solid lines are plotted in Figure 14 (a.2) and (b.2), where the cell is discharged with C/3 for 9 minutes to reach the same target SOC for the PR profile. The corresponding terminal voltage variations and the zoom-in view of the voltage difference between the relaxation voltage and the OCV are plotted in Figure 14 (a.3)-(b.3) and (a.4)-(b.4), respectively.

The total time taken by OC and PR profile at 40 and 10 °C is summarized in Table 5, where both of them take almost the same time to reach the  $\pm 1\text{mV}$  error bound at 40°C. However, the OC profile takes 33.7% less than the PR to reach the  $\pm 0.5\text{mV}$  error bound. In addition, the relaxation time by both methods at 40°C is shorter than that at 25°C under the same level of the equilibration. These two results are due to an increased lithium-ion diffusivity in anode and cathode particles at elevated temperatures that leads to decreased ion concentration gradients and fast diffusion processes.

The advantage of fast equilibration of the OC method can also be seen at 0°C, where the testing time by OC profile is 78.4% and 52.1% shorter than that by PR profile method with the  $\pm 1\text{mV}$  and  $\pm 0.5\text{mV}$  error bound. As the values of solid phase diffusivity drops at lower temperature condition, the time to reach equilibrium at 0°C is generally longer than that at 25°C.



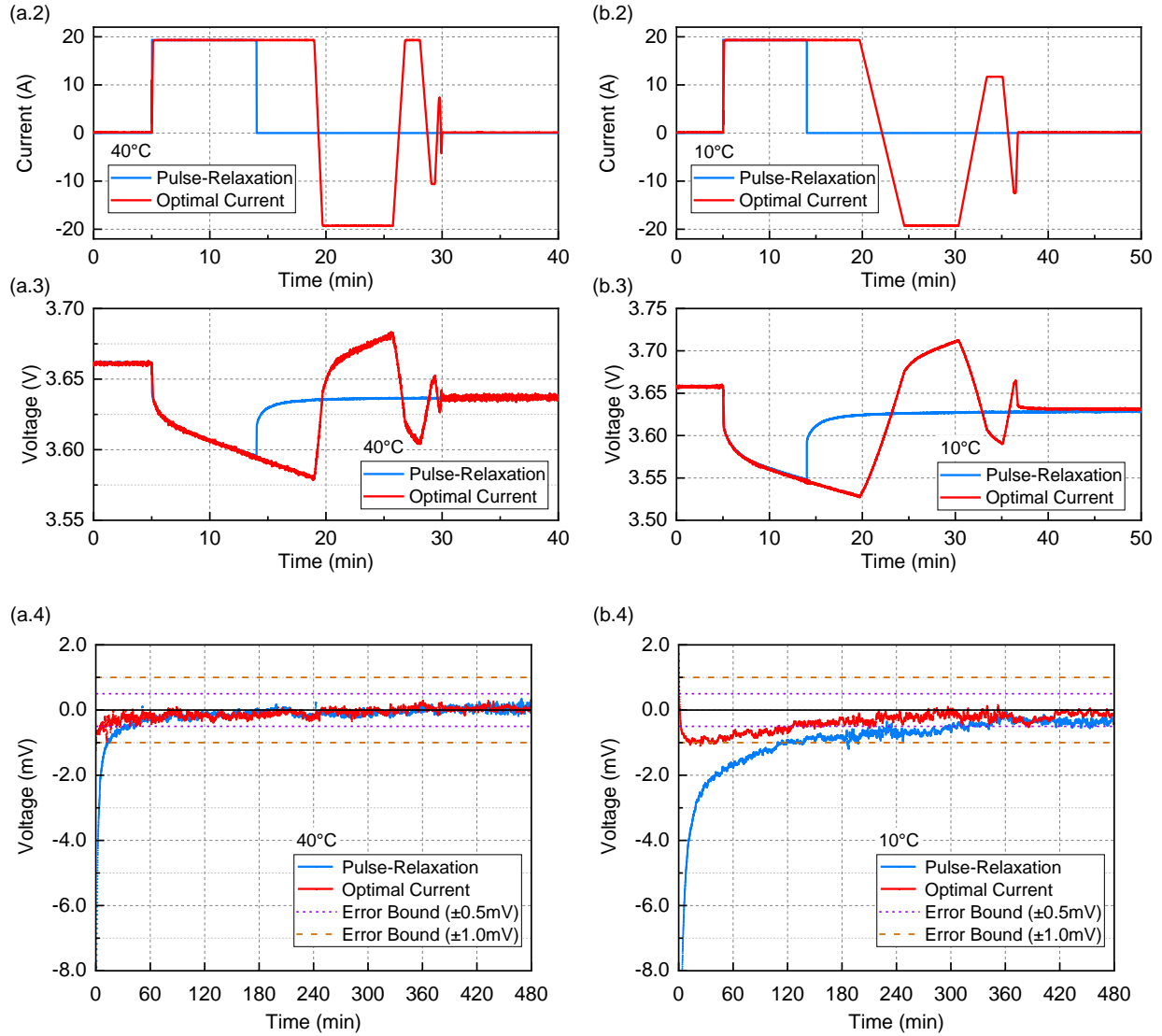


Figure 14. Model validation by comparison between experimental and simulated terminal voltage at C/3 charge and discharge at (a.1) 40°C and (b.1) 10°C, respectively. Comparison of experimental results by pulse-relaxation profile and the optimal-time current profiles: (a.2, b.2) current profile, (a.3, b.3) terminal voltage, and (a.4, b.4) voltage difference between the relaxation voltage and OCV at 40°C and 10°C, respectively.

Table 5. Times for two profiles at 40°C and 10°C.

T (°C)	Type	Testing time (min)			Percentage of saved time
		Charge/Discharge	Relaxation	Total	
40	PR ( $\pm 1\text{mV}$ )	9	15.5	24.5	-

	OC ( $\pm 1\text{mV}$ )	25	0	25	
	PR ( $\pm 0.5\text{mV}$ )	9	43	52	33.7%
	OC ( $\pm 0.5\text{mV}$ )	25	9.5	34.5	
10	PR ( $\pm 1\text{mV}$ )	9	138	147	78.4%
	OC ( $\pm 1\text{mV}$ )	31.7	0	31.7	
	PR ( $\pm 0.5\text{mV}$ )	9	320	329	52.1%
	OC ( $\pm 0.5\text{mV}$ )	31.7	126	157.7	

### 3.2.4 Summary

In this section, an equilibration method for lithium-ion batteries is proposed that significantly reduces the settling time needed for a battery cell to reach an equilibrium state when SOC is changed from one to a target value. An optimal current profile is obtained using optimal control theory along with the electrochemical model. The resulting current profile is implemented in a test station, and its performance is tested with a pouch type lithium-ion battery with NMC/graphite chemistry. The proposed OC profile at a constant temperature of  $25^\circ\text{C}$  reduces up to 55.8% and 58.3% testing time compared with that by the current PR method dependent upon  $\pm 1\text{mV}$  and  $\pm 0.5\text{mV}$  OCV error bounds, while the OC method  $10^\circ\text{C}$  and  $40^\circ\text{C}$  does up to 78.4% and 33.7% testing time, respectively. As a result, the testing time can be significantly reduced regardless of operating temperatures.

### 3.3 Hybridized time-frequency domain analysis (HTFDA) method

In this section, we propose a new method for measurement of the entropy coefficient based on a hybridized time-frequency domain analysis (HTFDA) technique [41]. This method is similar to the potentiometric method, but a sinusoidal temperature excitation is applied to the cell, and a two-step data processing procedure is applied, which includes (1) background correction in the time domain, and (2) entropy coefficient determination in frequency domain. In the first step, the background correction decouples the relaxation induced voltage offset from the raw  $U_{OC}$  data by fitting background voltage response with a polynomial equation, which reduces the usual multiple hours of relaxation time to approximately 30 min. In the second step, the periodic  $U_{OC}$  response is analyzed in the frequency domain using a FT, which is then used to determine the value of the entropy coefficient in the frequency domain. Due to the performance of the fast Fourier transformation (FFT), the applicable equivalent TCR (ETCR) for the exciting step magnitude of the temperature can be increased to  $2.5^{\circ}\text{C}/\text{min}$ .

#### 3.3.1 Principle

Open-circuit voltage ( $U_{OC}$ ) is the battery terminal voltage specifically at the ideal equilibrium state that is given by the difference of equilibrium potentials of two electrodes. The equilibrium potential is a function of a stoichiometric number that represents ion concentrations, which is given from the Nernst Equation [42]. Subsequently, the  $U_{OC}$  varies with SOC, operating temperature, and the degree of aging [43]. For a fresh cell,  $U_{OC}$  is expressed only as a function of SOC and temperature,  $U_{OC}(\text{SOC}, T)$ . When the cell is set to a specific SOC, the  $U_{OC}$  should be solely dependent upon  $T$ . This nonlinear function can be linearized using the Taylor series expansion with the first order at a given temperature  $T_0$  as follows:

$$U_{oc}(T) = U_{oc}(T_0) + \frac{\partial U_{oc}}{\partial T}(T - T_0) \quad (17)$$

Before measurement of the  $U_{oc}$ , the SOC should be set by a charge or discharge current, and a new equilibrium of the terminal voltage should be reached, which takes hours or even days of relaxation depending on the chemistry and structure of each electrode [30]. The measured terminal voltage during the relaxation,  $V_t(T, t)$  is expressed by a sum of the  $U_{oc}$  and the relaxation induced time-dependent offset,  $v(t)$  as follows:

$$V_t(T, t) = U_{oc}(T, t) + v(t) \quad (18)$$

, where the effects of side reaction and self-discharge on the terminal voltage and the thermal effects such as heat of mixing are presumably negligible at the low currents [48]. Thus, the  $v(t)$  becomes independent of other side effects and temperature.

Based on this assumption, combining Eq. (17) and Eq.(18) can yield:

$$V_t(T, t) = U_{oc}(T_0) + v(t) + \frac{\partial U_{oc}}{\partial T}(T - T_0) \quad (19)$$

The left hand side term in Eq.(19) represents the measured terminal voltage at time  $t$  and temperature  $T$ . The first and second terms in the right side refer to the  $U_{oc}$  at a reference temperature  $T_0$  (reference  $U_{oc}$ ) and the relaxation induced voltage offset. The last term represents the temperature induced  $U_{oc}$  change, which contains the entropy coefficient  $\frac{\partial U_{oc}}{\partial T}$  and temperature  $T$ .

When the temperature changes, the  $V_t$  varies as well. When a sinusoidal temperature is applied to the cell, the resulting function of the last term should contain the same frequency as that of the applied temperature function.

The FT of a sine function can be expressed with a sum of two Dirac pulses that have a positive and a negative frequency  $f_i$ :

$$\mathfrak{F}[\sin(2\pi f_i t)] = \frac{i}{2} [\delta(f + f_i) - \delta(f - f_i)] \quad (20)$$

When applying a sinusoidal temperature profile to the cell

$$T(t) = T_0 + \Delta T \sin(2\pi f_i t) \quad (21)$$

, where  $\Delta T$  represents the amplitude of the temperature change and  $f_i$  represents the frequency, the  $U_{OC}$  expression in Eq.(19) becomes:

$$V_t(T, t) = U_{OC}(T_0) + v(t) + \Delta T \frac{\partial U_{OC}}{\partial T} \sin(2\pi f_i t) \quad (22)$$

Fourier transformation of Eq. (22) in the frequency domain results in the expression of  $U_{OC}$ :

$$\mathfrak{F}[V_t(T, t)] = U_{OC}(T_0) \cdot \delta(f) + \mathfrak{F}[v(t)] + \Delta T \frac{\partial U_{OC}}{\partial T} \frac{i}{2} [\delta(f + f_i) - \delta(f - f_i)] \quad (23)$$

According to the superposition principle of the FT,  $V_t$  in frequency domain is a sum of all of terms. The first term in the right side refers to the  $U_{OC}(T_0)$  in frequency domain, where  $U_{OC}(T_0)$

does not vary over time and contains only a DC component. The second term represents the frequency response of the relaxation-induced voltage offset. Its FT results in a monotonically decreasing function of the frequency that is hard to decompose in frequency domain but is easily separated and removed in time domain [30]. Based on these facts aforementioned, a new two-step procedure is proposed that combines the time domain analysis with the frequency domain analysis, which is called Hybridized Time and Frequency Domain Analysis (HTFDA):

(1) Time domain analysis for background correction

Previous study [30] on voltage behaviors during the relaxation period has shown that the voltage relaxation occurs rapidly initially and slows down over time, allowing for the response to be approximated by a parabolic function in the time domain as follows:

$$v(t) = a_0 + a_1t + a_2t^2 \quad (24)$$

By subtracting the empirical  $v(t)$  from  $V_i(T,t)$  in the time domain, the relaxation voltage offset term is removed and the remaining voltage changes,  $U_{OC}^*(T,t) = V_i(T,t) - v(t)$  reflect the time response to the temperature excitation (the last term in the right side of Eq.(22) and Eq.(23) in time and frequency domain respectively). The time domain background correction technique works to compensate the effect of the long-lasting voltage relaxation for the measurement of entropy coefficient, so that the measurement can be performed even at the non-equilibrium state, and thus the testing time can be drastically reduced.

After the background correction in time domain, the expression of Eq.(23) is modified to:

$$\Im[U_{oc}^*(T,t)] = U_{oc}(T_0) \cdot \delta(f) + \Delta T \frac{\partial U_{oc}}{\partial T} \frac{i}{2} [\delta(f + f_i) - \delta(f - f_i)] \quad (25)$$

## (2) Frequency domain analysis for determination of entropy coefficient

The entropy coefficient is determined by transforming the measured response in time domain to the frequency domain using the FT. The third term in Eq.(23) reflects the contribution from the first harmonic  $f_i$  of the input frequency. When the temperature  $T$  is a sinusoidal function, change in the  $U_{oc}(T,t)$  is also a sinusoidal function with the same frequency. The value of the Fourier coefficient of  $f_i$  of this term contains the expression of entropy coefficient, thus the value of the entropy coefficient can be determined by:

$$\left| \frac{\partial U_{oc}}{\partial T} \right| = \left| \frac{2}{\Delta T} P(f_i) \right| \quad (26)$$

, where  $P(f_i)$  denotes the amplitude of the frequency spectrum of  $\Im[U_{oc}^*(T,t)]$  at  $f=f_i$ .

The sign of the entropy coefficient is determined from the phase angle between  $T$  and the corresponding  $U_{oc}^*(T,t)$  signal at frequency  $f_i$ . The Fourier coefficient at  $f_i$  expressed in Eq.(25) is a pure imaginary number  $-\Delta T \frac{\partial U_{oc}}{\partial T} \frac{i}{2}$  and its phase angle is either  $-\frac{\pi}{2}$  or  $\frac{\pi}{2}$  dependent upon the sign of the entropy coefficient. In the experiment, there is always a time delay between the temperature excitation and the voltage change caused by the heat capacity of the cell, which leads to a slight deviation of the phase angle change around its expected value, but without a change of the sign.

Thus, the entropy coefficient is determined as follows:

$$\frac{\partial U_{oc}}{\partial T} = -\text{sgn}[\angle PA(f_i)] \cdot \left| \frac{2}{\Delta T} P(f_i) \right| \quad (27)$$

, where  $\angle PA$  denotes the phase angle in radian at the frequency  $f_i$ .

### 3.3.2 Experiments

In order to reduce the measurement time of the entropy coefficient, there are two possibilities, increase of TCR and decrease of  $\Delta T$ . A new term Equivalent Temperature Change Rate (ETCR, °C/min) is introduced to compare effects of sinusoidal temperature excitation on the measurement time with those of the conventional potentiometric methods. ETCR is given as the temperature amplitude divided by the time needed from the DC offset reference to reach the maximal amplitude of the temperature. The relationship between the  $\Delta T$ ,  $f_i$ , and the ETCR is given as follows:

$$ETCR = 240\Delta T f_i \quad (28)$$

The proposed measurement method for the entropy coefficient by HTFDA is applied to lithium-ion cells and its performance is evaluated by comparison with that of the conventional potentiometric method and the calorimetric method.

#### 3.3.2.1 Cell and test station

The battery cell used for the experiments and the test station is the same as those described in Section 2.3.1.

### 3.3.2.2 Design of experiments

During experimental measurement and analysis, two tests were designed that aimed to analyze the effect of ETCR and temperature amplitude on the measurement accuracy, and in turn measure the entropy coefficient using HTFDA with the goal of comparing the results with those from the conventional potentiometric method and calorimetric method.

#### (1) Effects of ETCR and temperature amplitude

Initially, the cell is fully charged up to 100% SOC and then allowed to relax for 10 hours in order to reach equilibrium. At the equilibrium state, a sinusoidal temperature reference is applied to the multifunctional calorimeter to create the same surface temperature profile of the cell. The amplitude of the reference temperature is set with  $\Delta T=15^{\circ}\text{C}$ , and different rates of ETCR are selected from 0.5, 1.0, 1.5, 2.0 to  $2.5^{\circ}\text{C}/\text{min}$ . For each rate, two periods of the temperature were applied. The data for the temperature and the voltage of the cell were collected at a sampling rate of 2Hz. Secondly, the amplitude of temperature was increased from  $5^{\circ}\text{C}$  to  $20^{\circ}\text{C}$  while the ETCR was kept constant at  $2.5^{\circ}\text{C}/\text{min}$ . All other experimental steps were identical to previous conditions.

#### (2) Determination of the entropy coefficient

To start measurement of the entropy coefficient using HTFDA, the cell was fully charged at  $25^{\circ}\text{C}$ . Then, the cell was stepwise discharged at 0.1C for 30 minutes, which corresponds to a discharge capacity step of 1.295Ah and 5% SOC decrease. After a step for discharge, the cell was rested for 30 minutes, so that the cell reached equilibrium. Then, a sinusoidal temperature profile was applied to the cell. Detailed information of the values chosen for the  $T_0$ ,  $\Delta T$ ,  $f$ , and the ETCR is listed in Table 6.

The sinusoidal temperature excitation is held for two periods at first and then was kept at 25°C for 10 minutes for the cell to equilibrate and then repeated for the next discharge step. The time for each SOC step of HTFDA requires 72 minutes and the total time to complete the measurement requires 34 hours. The data collected for the temperature and the voltage was used to determine the entropy coefficient of the cell using the proposed HTFDA method.

The performance of the HTFDA is compared with that of the conventional potentiometric method and the calorimetric method. For the conventional potentiometric method, the same experimental setup as HTFDA method is used. The value of TCR was selected to be 0.5°C/min in order to obtain a linear relationship between  $U_{OC}$  and  $T$  [28]. Other detailed parameters are also listed in Table 6. The conventional potentiometric method required a total time of 294 hours for 20 SOC points. After completion of the measurements, the entropy coefficient was determined using the least-squares linear fit to the slope of  $U_{OC}$  to  $T$ .

Table 6. Parameters and comparison of the required time for measurement of the entropy coefficient between HTFDA and conventional potentiometric method (CPM).

	HTFDA	CPM
$\Delta SOC / \%$	5	5
$T_0 / ^\circ C$	25	25
$\Delta T / ^\circ C$	10	10
$f_i / mHz$	1.04	-
ETCR / $^\circ C/min$	2.5	0.5
Measurement duration per SOC / h	1.2	14.7

For validation of the calorimetric method, the designed multifunctional calorimeter is used. The cell was fully charged and then discharged at 0.1C to certain SOC. After reaching equilibrium,

a testing profile consisting of a 120s 2C discharge, 1h resting, and 120s 2C charge was applied to the cell. The calorimeter measured the total heat generated during the discharge and charge separately while maintaining the temperature of the cell at 25°C.

The measurement was performed by decreasing the SOC from 80% to 20% with  $\Delta\text{SOC}=10\%$ . The entropy coefficient was determined by [28]:

$$\frac{\overline{\partial U_{OC}}}{\partial T} = \frac{Q_{dis} - Q_{ch}}{-2I_0 t_0} \quad (29)$$

, where  $Q_{dis}$  and  $Q_{ch}$  denote the total heat during discharge and charge,  $I_{dis} = -I_{ch} = I_0 (> 0)$ , and  $t_{dis} = t_{ch} = t_0$ . The entropy coefficient determined by the calorimetric method is an averaged value over the SOC range (6.7% in our case) assessed during the charging and discharging process.

### 3.3.3 Result and discussion

#### 3.3.3.1 Selection of an optimal ETCR

Figure 15 (a) shows the average measured surface temperature obtained by averaging the readings of three thermocouples (TC1~TC3) of the cell at different ETCRs,  $R_1=0.5^\circ\text{C}/\text{min}$ ,  $R_2=1.0^\circ\text{C}/\text{min}$ ,  $R_3=1.5^\circ\text{C}/\text{min}$ ,  $R_4=2.0^\circ\text{C}/\text{min}$ , and  $R_5=2.5^\circ\text{C}/\text{min}$ . The corresponding responses of  $U_{OC}$  were plotted in Figure 15 (b). For a clearer representation, the raw data of  $U_{OC}$  were smoothed by means of a moving average filter and plotted as curves in the following figures. At 100% SOC, the  $U_{OC}$  is in phase with the change of the temperature, which indicates a positive entropy coefficient.

Additionally, the frequency spectra of  $U_{OC}$  obtained by the FFT is plotted in Figure 2 (c), where the highest peak is located at  $f_i = 0.104, 0.208, 0.312, 0.417$  and  $0.521$  mHz for each case, which corresponds to the fundamental frequency of the AC temperature excitation at  $R_1$  to  $R_5$ , calculated by Eq.(28). These peaks show a similar magnitude to each other despite the different frequencies.

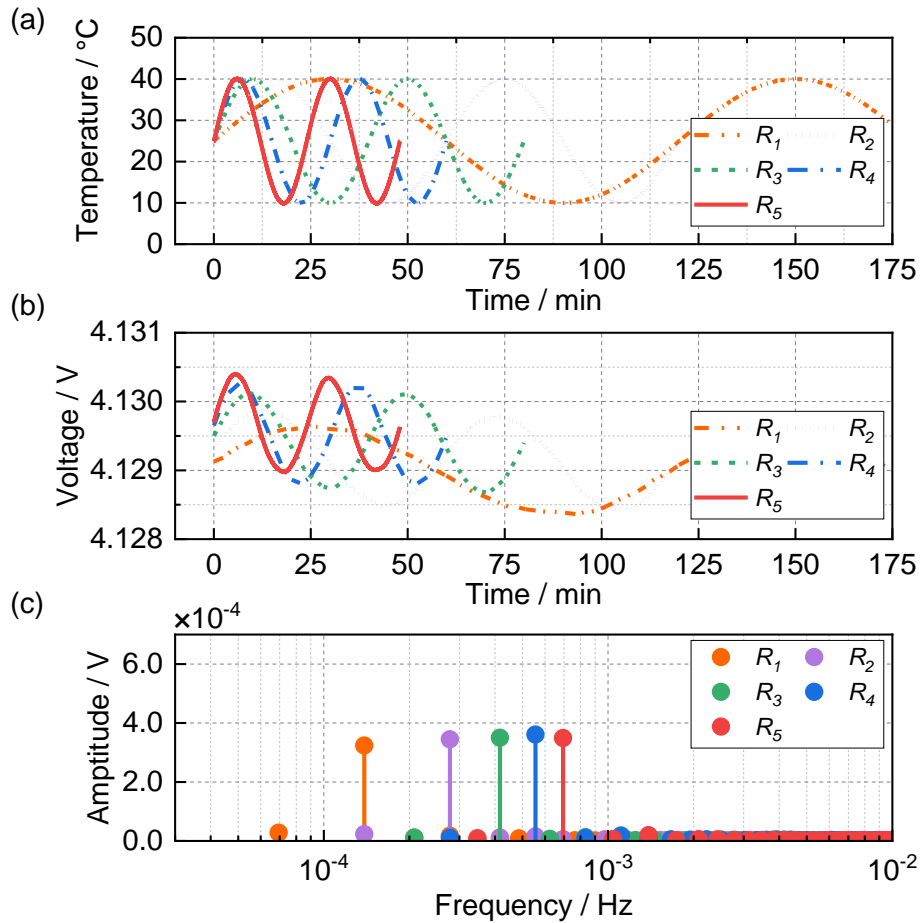


Figure 15. Averaged surface temperature and (b)  $U_{OC}$  response versus time for different ETCRs:  $R_1=0.5^\circ\text{C}/\text{min}$ ,  $R_2=1.0^\circ\text{C}/\text{min}$ ,  $R_3=1.5^\circ\text{C}/\text{min}$ ,  $R_4=2.0^\circ\text{C}/\text{min}$ ,  $R_5=2.5^\circ\text{C}/\text{min}$ , for clarity, only one period test of  $R_1$  was plotted; (c) frequency spectra of  $U_{OC}$ , at 100% SOC.

The entropy coefficients for each case were calculated using Eq. (27) and plotted in Figure 16 (a) as a function of different ETCRs. The black dashed line indicates the entropy coefficient

measured by the conventional potentiometric method, where the values of the determined entropy coefficients at the different ETCRs are in good accordance with the reference value of  $4.761 \times 10^{-5}$  V/K. The relative errors to the reference value are less than 3.7%. As a result, the effect of the variation of the ETCR of the temperature excitation on the measurement of the entropy coefficient for the proposed method is negligible.

For the determination of the entropy coefficient, an appropriate ETCR is selected by considering the following three facts:

- (1) The ETCR of the temperature excitation has little impact on the measurement result.
- (2) The higher ETCR is, the shorter becomes the measurement duration.
- (3) The maximum temperature change rate of the cell is limited by the cooling/heating capacity of the multifunctional calorimeter and the heat capacity of the cell.

Consequently,  $2.5^{\circ}\text{C}/\text{min}$  is selected as the optimal ETCR, and is applied for the following tests.

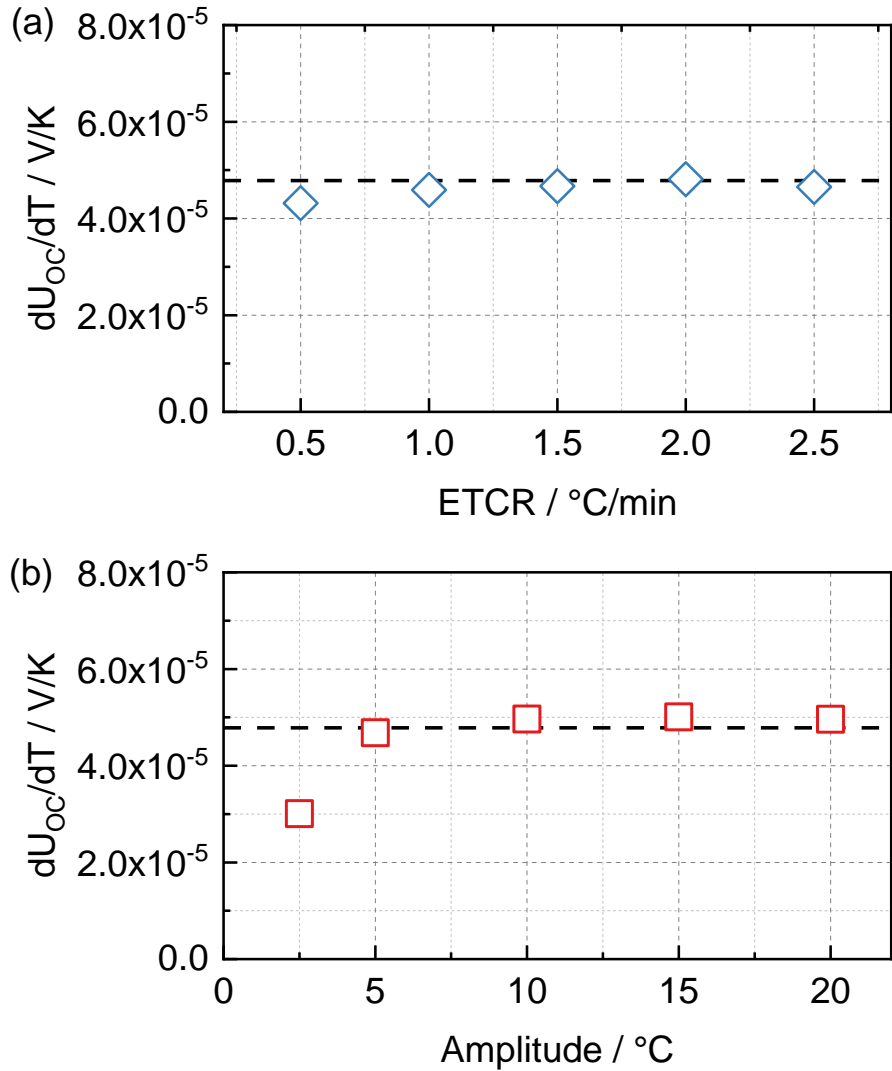


Figure 16. Comparison of determined entropy coefficient at different (a) ETCR and (b) temperature amplitudes at 100% SOC. The entropy coefficient measured from conventional potentiometric method, as a reference (black dash line).

### 3.3.3.2 Selection of an optimal temperature amplitude

A series of temperature excitations at a fixed ETCR =  $2.5^\circ\text{C}/\text{min}$  with different amplitude ( $\Delta T_1=2.5^\circ\text{C}$ ,  $\Delta T_2=5^\circ\text{C}$ ,  $\Delta T_3=10^\circ\text{C}$ ,  $\Delta T_4=15^\circ\text{C}$  and  $\Delta T_5=20^\circ\text{C}$ ) were applied to the cell. After the

ETCR has been fixed at 2.5°C/min, different amplitudes of the temperature excitation are applied to the cell in order to find an optimal value for the measurement of the entropy coefficient. The average surface temperatures and the corresponding responses of  $U_{OC}$  are plotted in Figure 19 (a) and (b). As seen here, the amplitude of  $U_{OC}$  is in phase with the temperature. The amplitude of the peaks are plotted in Figure 19 (c), which tends to decrease as  $\Delta T$  decreases from 20°C to 2.5°C.

For the lithium-ion cells, the value of the entropy coefficient is usually in the order of  $10^{-4} \sim 10^{-5}$  V/K. When  $\Delta T$  becomes small, the value of the  $U_{OC}$  change by a variation of temperature becomes small and is easily masked by the noise. As shown in Figure 19 (c), when  $\Delta T$  is 2.5°C, the amplitude of the peak at  $f_i$  is too small to identify. Thus, a large measurement error is induced.

Figure 16 (b) shows a comparison of the calculated entropy coefficient of the cell at different temperature amplitudes. For an amplitude of temperature at  $\Delta T_3$ ,  $\Delta T_4$  and  $\Delta T_5$ , the value of the determined entropy coefficients are very similar and are all close to the reference. When the amplitude of the temperature was decreased lower than 5°C, the error began to increase. At  $\Delta T_1=2.5^\circ\text{C}$ , the relative error was 36.8%. Thus, a large temperature perturbation is required to maintain the accuracy.

However, the high temperature range results in a long measurement time and potentially exceeds limitation of the safe operating temperature range, 15~40°C [1] [44]. Therefore, a compromise has been found between the measurement accuracy and the measurement duration, where  $\Delta T=10^\circ\text{C}$  at the reference  $T_0=25^\circ\text{C}$  is chosen.

### 3.3.3.3 Background correction of voltage offset in time domain

#### (1) Analysis

The terminal voltage during resting includes a time-variant voltage offset that is measured after 10, 20, 30 and 65 minutes and at different SOC, which are plotted in Figure 17. The offset voltages see the most significant decay within the first 10 minutes, which is caused by the equilibration of the lithium-ion concentration within the particles and by the diffusion process of ions across the electrodes [37]. In addition, the decaying behavior of the offset voltage is dependent on the SOC, which can be caused by the SOC dependent diffusion coefficient of the lithium ions in solid states [45], [46]. Typically, the cell would be required to reach equilibrium prior to proceeding, however, in this method, a correction can be made to remove the relaxation effect and determine the response with respect to the equilibrium potential.

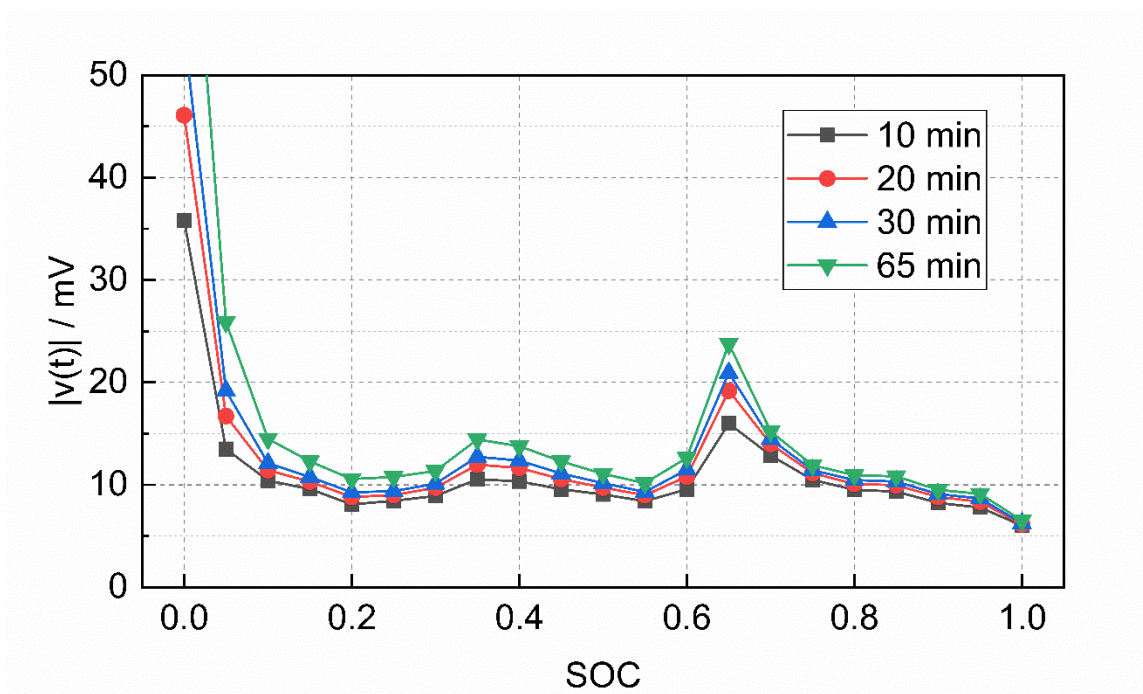


Figure 17. Voltage offset after resting time of 10, 20, 30 and 65 minutes as a function of SOC

(2) Correction

When a cell is thermally excited at a non-equilibrium state by applying a sinusoidal temperature perturbation, the terminal voltage immediately responds and tends to follow the applied temperature profile, but with an offset to the reference. The measured voltages at 100%, 50% and 20% SOC are plotted in Figure 18 (a)-(c) as red solid lines. In order to remove this relaxation-induced voltage offset from the measured voltage curve, a correction was made using an empirical function that is obtained by a curve fitting of voltage offset curve  $v(t)$ . To perform this correction, the terminal voltage is collected at the reference temperature of 25°C at rest in the 10 minutes prior to and following the temperature excitation, and then approximated by a parabolic function, as Eq. (24) (black dashed lines). Finally, the compensated voltage,  $U_{OC}^*(T,t)$  is obtained by subtracting the polynomial function  $v(t)$  from the terminal voltage, so that the remaining  $U_{OC}^*(T,t)$  changes only include the response to the temperature excitation (solid blue lines).

The voltage responses are analyzed in the frequency domain and the corresponding frequency spectra before and after the voltage correction offset are plotted in Figure 18 (d)-(f). Prior to the correction, the spectra includes a fundamental frequency and harmonics. The amplitude of the harmonics monotonically decreases as the frequency increases, which is caused by the polynomial-shaped voltage offset in time domain [47]. Following the correction, the amplitude of the harmonics is decreased aside from that of the fundamental frequency.

The intent of compensating for the voltage offset is to minimize the effects on the measured terminal voltage, which results in reduction of the relaxation time. By employing this method for HTFDA entropy coefficient measurement, the time to reach equilibrium is significantly reduced compared to other methods, and the time necessary to sample at each SOC is less than 0.5 hour. In addition, the method reduces the resting time to 80%~95% of that by the conventional potentiometric method [48] [31].

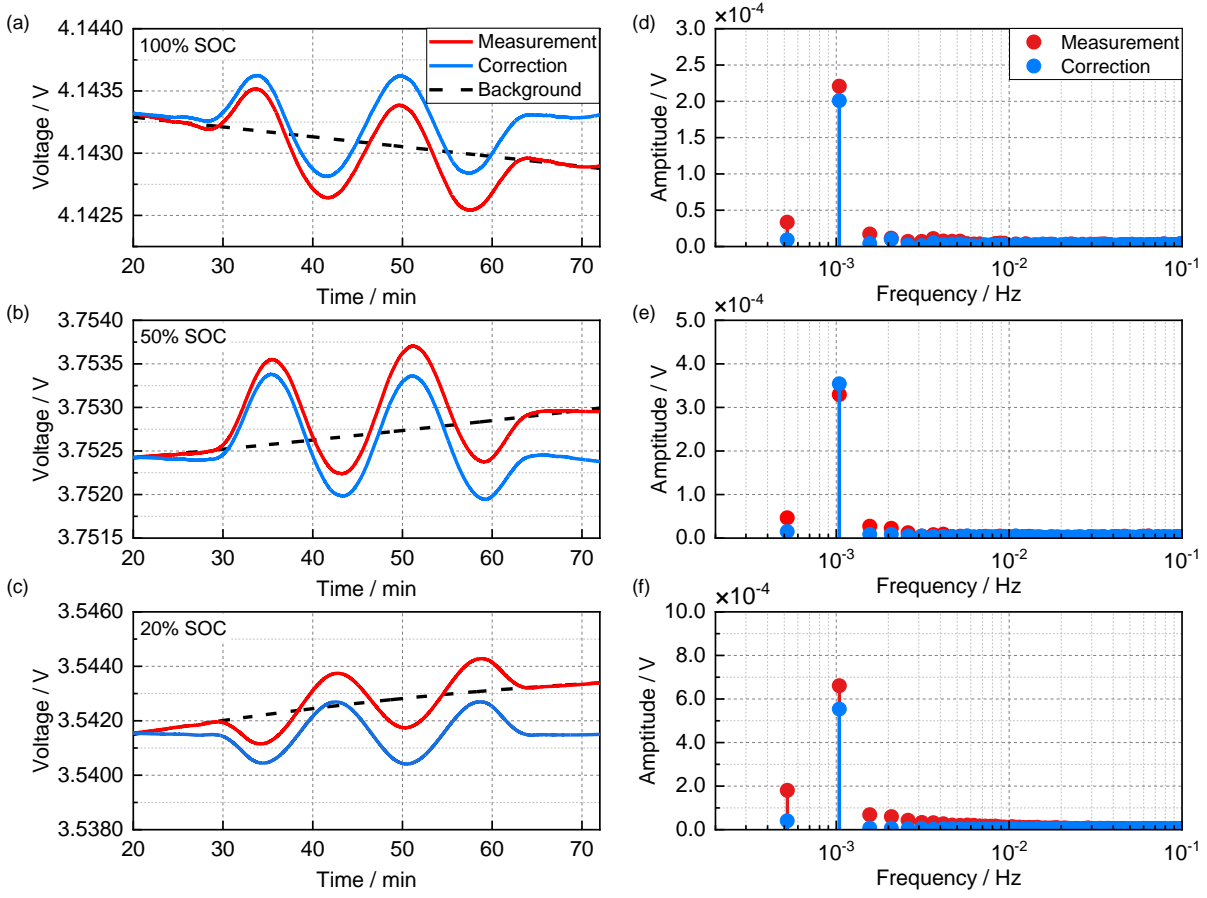


Figure 18. Measured voltage, background offset and the voltage after correction at (a) 100% SOC, (b) 50% SOC and (c) 20% SOC, and (d) ~ (f) the corresponding frequency spectra.

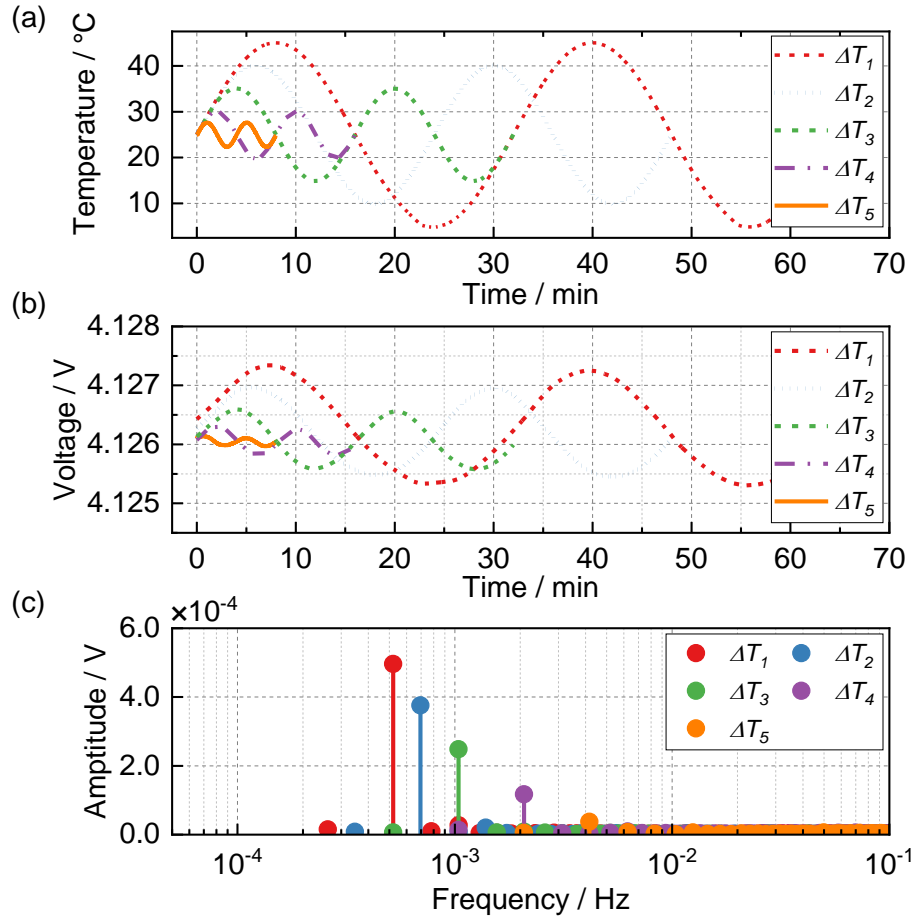


Figure 19. (a) Averaged surface temperature and (b)  $U_{OC}$  response at different temperature amplitudes:  $\Delta T_1=2.5^\circ\text{C}$ ,  $\Delta T_2=5^\circ\text{C}$ ,  $\Delta T_3=10^\circ\text{C}$ ,  $\Delta T_4=15^\circ\text{C}$  and  $\Delta T_5=20^\circ\text{C}$ ; (c) frequency spectra of  $U_{OC}$  at 100% SOC.

### 3.3.3.4 Comparison of the HTFDA method with others

Firstly, the effectiveness and the necessity of the time-domain background correction was evaluated by comparing the measurement result from HTFDA with the data measured by the conventional potentiometric method (CPM) as a reference.

Three profiles are shown in Figure 20 (a), where the orange line indicates the entropy coefficient profile calculated using frequency domain analysis (FDA) by Eq. (27), but without the

background correction. The red line indicates the entropy coefficient by HTFDA method including the background correction, and the blue line represents the CPM.

At high SOC ranges from 70% to 100% SOC, all three methods provide similar values of the entropy coefficient. As SOC decreases, the difference in the measured entropy coefficients between the non-corrected FDA and the CPM begins to increase, becoming noticeable at 65% SOC and significant below 10% SOC. This tendency aligns well with the profile of the voltage offset at different SOC, as shown in Figure 17, which is the primary cause for the discrepancy. This discrepancy can be minimized by applying the background correction in HTFDA method, which illustrates that the measurement result is in good accordance with that by CPM for the SOC range from 0% to 100%, as seen in Figure 7(a) In addition, both results by HTFDA and CPM show a similar trend, with values in good quantitative agreement with the published data for LMO-NMC blended cells collected using the potentiometric method [49][50][51].

As seen in Figure 7(a), the measured entropy coefficient for the cell ranges from  $-3.7 \times 10^{-4}$  V/K to  $1.0 \times 10^{-4}$  V/K, with a shift in sign around 88.5%, 65.5% and 37.8% SOC, respectively, which indicates a transition between endothermic and exothermic reversible heat generation. It should be noted here that the trends in entropy coefficient are not representative of a single electrode or material in the cell, rather, the magnitude and the shape of the entropy coefficient is affected by the competing reactions of both electrodes and the associated entropy change for each. For example, when considering LMO as cathode chemistry, the entropy coefficient generally decreases from positive to negative values during the transition from a fully delithiated to lithiated state, a local valley at around 85% SOC is typically seen [28] [49]. This gradual shift from positive to negative as seen in Figure 7(a) is representative of this phenomenon and the overall entropy coefficient varies between  $1.0 \times 10^{-4}$  V/K and  $-3.5 \times 10^{-4}$  V/K, which is comparable to the  $2.5 \times 10^{-4}$

V/K to  $-3.7 \times 10^{-4}$  V/K range typically seen for LMO. In contrast, the curve of the entropy coefficient for the NMC cathode is rather smooth and its variation is quantitatively smaller in comparison and ranges from  $0.3 \times 10^{-4}$  V/K to  $-1.7 \times 10^{-4}$  V/K [18][21], which indicates a minimal impact on the shape of the curve. Additionally, the entropy coefficient for a graphite anode shows a distinct plateau around 40%~55% SOC and 60%~85% SOC because of phase transitions [52] [53] and its range is  $-3.7 \sim 1.8 \times 10^{-4}$  V/K, similar to the additional phenomena seen in Figure 7(a).

The review above reveals that the shape of the entropy coefficient of the cell used in this work, as shown in Figure 20(a) is qualitatively similar to that of a cell with the graphite and LMO, where the peak, the inflection points, and the valley are shown at 95% SOC, around 85% SOC, and at 5% SOC, respectively. In addition, the inflection points near at 65%, 35%, and 10% SOC correspond to  $x=0.52$ ,  $0.27$ , and  $0.09$  of  $\text{Li}_x\text{C}$  in graphite, which indicates potential structure changes from the stage 2, to stage 2L and stage 4 [53].

Though the conventional potentiometric method (CPM) enables an accurate and reliable measurement of the entropy coefficient, it takes several weeks to obtain an entropy coefficient - SOC curve at one condition. This drawback is primarily caused by two factors: prolonged relaxation time caused by long-term equalization effect, and limited TCR (lower than  $0.5^\circ\text{C}/\text{min}$ ) in order to obtain a linear relationship between  $U_{OC}$  and  $T$  [28]. Over the course of our study, the implemented CPM in the test station took around 294 hours across 20 SOC points, which includes a 12-hour relaxation and a 2.7-hour temperature excitation per SOC. Further improved CPM [30] that employed the background correction approach was able to drastically reduce the relaxation time to 1.5 hour per SOC, but the time for the temperature excitation still requires the same time as that of the CPM with a TCR =  $0.5^\circ\text{C}/\text{min}$ .

The proposed HTFDA method not only takes advantage of the background correction to shorten the relaxation time, but also incorporates the frequency domain analysis for the entropy coefficient measurement, which is applicable at increased ETCR up to 2.5°C/min. The overall time needed for HTFDA at each SOC step is reduced to 72 minutes, which results in significant time saving, requiring only 34 hours for a complete measurement procedure, which is 52% less time than that by Osswald's method and 88.4% less than that by CPM.

As seen in Figure 7 (b), the result by the proposed HTFDA method is compared with that of the calorimetric method (CM), where the measurement using the CM is repeated three times and its average value is plotted with green horizontal lines. The vertical thickness of the green boxes indicates the maximum error. The proposed HTFDA method produces similar values to that of the calorimetric method within the CM's measurable SOC range. However, CM has several drawbacks. For one, it requires an isothermal condition during testing, which is achieved through the use of a set of well-calibrated and highly dynamic calorimeters, which are not trivial to design or obtain. In addition, the calorimetric method can only determine an averaged entropy coefficient over a limited SOC range. Moreover, its accuracy is highly affected by the size of the cell and amplitude of the charging and discharging current because of the signal-to-noise ratio [28], and the Ohmic resistance of the cell that is related to the irreversible heat generation [49]. Therefore, accurate measurements are difficult to obtain.

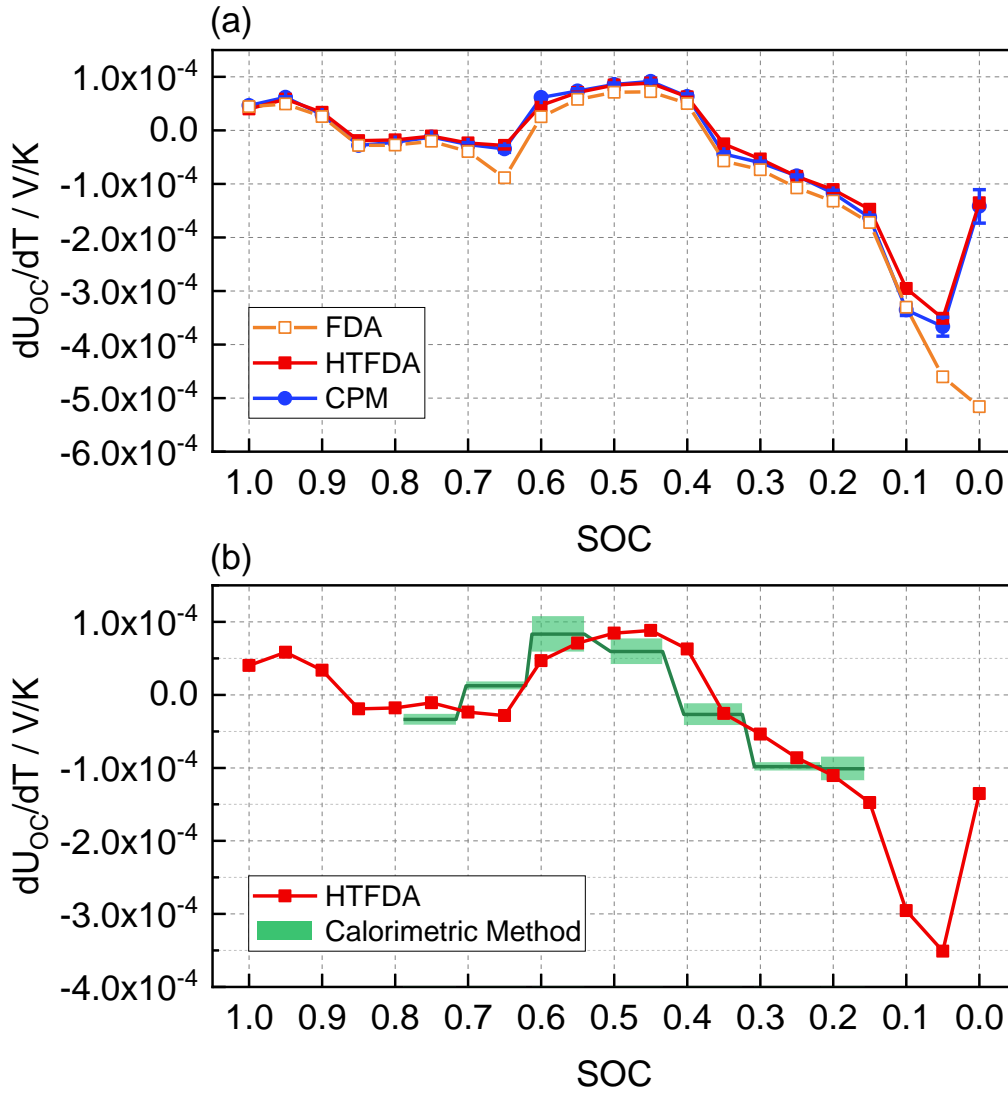


Figure 20. Entropy coefficient as a function of SOC for graphite-LMO/NMC battery by HTFDA and comparison with the measurement results from (a) conventional potentiometric method and (b) calorimetric method.

(1) Effect of reference temperature

During the operation of electric vehicles, electric scooters, and portable electronic devices, the ambient and operating temperature of the battery cells can vary widely, and knowledge of the entropy coefficient across the operating range is critical. Therefore, the entropy coefficient at

different reference temperatures was measured using the proposed HTFDA for further analysis. A graphite-LMO/NMC cell identical to the one used in the previous section was utilized, and the reference temperatures were set to 0, 15, 35 and 45°C. Before the measurement using HTFDA, the capacity of the cells was measured using the C/3 CC/CV charging and discharging method under 0, 15, 35 and 45°C. In addition, all the parameters of the sinusoidal temperature excitation were identical to those listed in Table 6. It was determined that at lower temperatures, such as 0°C, the relaxation voltage after 30 minutes still exhibits an exponential decaying pattern because of the slow relaxation of lithium-ion in solid, which causes a large error in the parabolic approximation that was used for the background correction and the corresponding measurement results. Therefore, the resting time after the discharge was extended from 30 minutes to 1 hour.

The entropy coefficient profiles at each reference temperature are plotted in Figure 21, where their shapes are identical, including all the critical inflection points. However, the absolute magnitude of the entropy coefficient is dependent upon the reference temperature. When the temperature changes, the absolute value of the coefficient tends to follow regardless of the SOC, which is similar to those published in previous works [29] [54]. In addition, the extent of the temperature-dependent effect varies at different SOCs, with the most notable effect being in 40%~60% SOC range, where phase transition occurs in the anode [55] and cathode [56] active materials. Since the entropy change ( $\Delta S$ ) reflects the way of how lithium-ions are ordered in the electrode material lattices, the value of the entropy coefficient ( $\frac{dU_{OC}}{dT} = \frac{\Delta S}{nF}$ ) is accordingly affected by the structure change and phase transition that occurred in the anode and cathode active materials at different temperatures. Based on the XRD analysis on NMC/LMO blend cathode [57][57], both NMC and LMO phases exhibit a structural change at different temperatures. The graphite anode also exhibits the changes in layer spacing and the range of certain phases when temperature varies

[58]. Consequently, the value of entropy coefficient varies with reference temperature of the measurements.

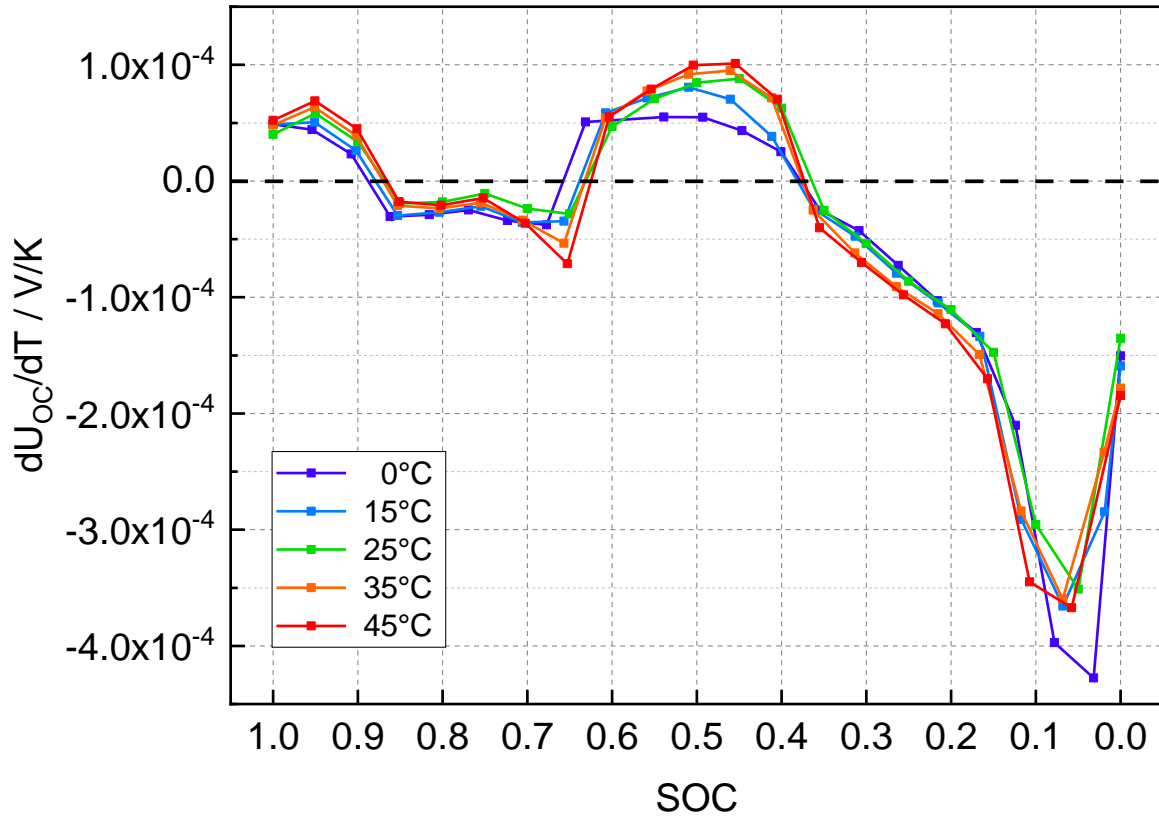


Figure 21. Entropy coefficient values of commercial graphite-LMO/NMC battery at different temperatures of 0°C, 15°C, 25°C, 35°C and 45°C.

(2) Effect of aging condition

In order to investigate effects of the aging condition on the entropy coefficient of the battery, four cells were cycled with 2C charging and 4C discharging at 25°C. The capacity of the cells were measured with C/3 discharge rate at 25°C. After 200, 250, 300 and 325 cycles of the aging tests, the capacity fade of the cells reached 4.85%, 8.88%, 14.65% and 19.23% that corresponds

to End-of-Life (EOL), respectively. The entropy coefficient of the aged cells were measured by applying the HTFDA method at 25°C, where the parameters of the sinusoidal temperature excitation were the same as those listed in Table 6.

The entropy coefficient profiles as a function of the discharge capacity for the cells at different states of aging are plotted in Figure 22. The resulting curves are similar in appearance, but scaled along with the magnitude of the entropy coefficient and shifted towards higher SOC values. With increased capacity fade of the cell, the flat portion of the entropy coefficient curve between 65% SOC and 85% SOC (A-A') becomes smaller and results in a local minimum A', when the cell reaches EOL. In addition, the plateau B/B' and the inflection point C/C' were shifted to the left at higher SOC. Moreover, the range of the  $dU_{OC}/dT$  decreased as the cell aged. The value of  $dU_{OC}/dT$  for a fresh cell ranged from  $-3.51 \times 10^{-4}$  to  $8.81 \times 10^{-4}$  V/K, while the entropy coefficient range of the cell with 19.23% capacity fade is  $-3.23 \times 10^{-4}$  to  $7.72 \times 10^{-4}$  V/K. When the cell is getting aged, the anode structure is changing during the degradation process. Based on the XRD analysis of the electrode [59], the graphite anode of the aged cell shows larger graphene layers stacking disorder. This will affect the Li-intercalated state of positive and negative electrode and thus, the value of entropy change (or entropy coefficient), as one of the thermodynamic parameters, will be changing accordingly.

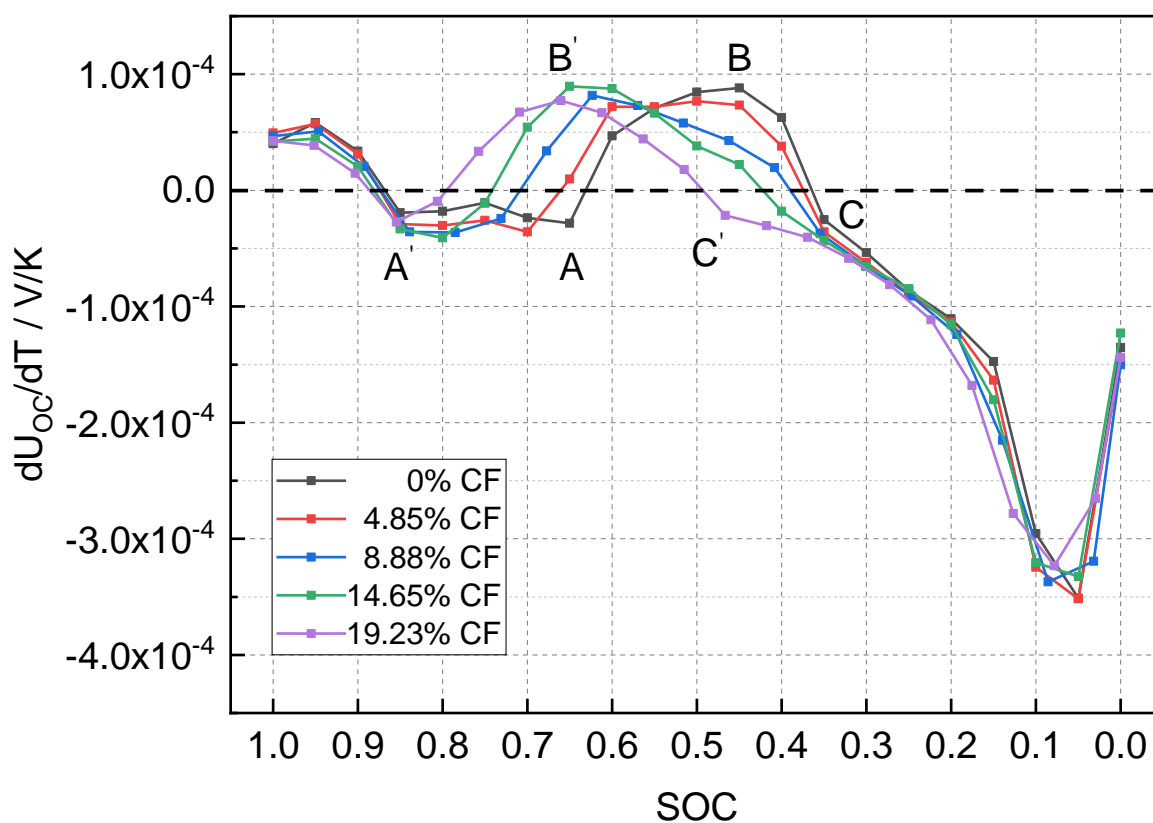


Figure 22. Entropy coefficient values of commercial graphite-LMO/NMC battery at different aging conditions.

### 3.3.4 Summary

In this section, a fast and accurate measurement method of entropy coefficient for lithium-ion batteries is proposed, which is based on a hybridized time-frequency domain analysis (HTFDA). The HTFDA works in two following sequential steps, time-domain background voltage offset correction and frequency-domain entropy coefficient determination. A test cell is excited with a sinusoidal temperature generated by the multifunctional calorimeter that follows the reference input with high and accurate dynamics, and the terminal voltage of the cell response is

measured. The excitation temperature needs two parameters, ETCR and the amplitude, which were determined with consideration of the effect on the time and accuracy of the measurement.

The cell used for experiments is a large format graphite-LMO/NMC pouch type lithium-ion battery. The results of the entropy coefficient measurement are compared with those measured by the conventional potentiometric method and calorimetric method.

Here is a summary of the major outcomes:

- HTFDA allows for fast and accurate determination of the entropy coefficient as a function of SOC.
- The accuracy of the HTFDA method is comparable to that of the conventional two methods.
- The measurement time of the HTFDA is drastically reduced to around 1/10 of that of the conventional potentiometric method.
- Entropy coefficient profiles are measured and compared at different reference temperatures and aging conditions, which allows for analysis of reversible heat source terms under real operating conditions.

### 3.4 Improved frequency-domain calorimetric method

#### 3.4.1 Principle

Based on the expression of the total heat generated given as Eq.(5), the reversible and irreversible heat source is expressed as a function of the input current  $I$  and  $I^2$ . If a sinusoidal current profile is applied to the cell,

$$I(t) = \Delta I \cdot \sin(2\pi f_i t) \quad (30)$$

, where  $\Delta I$  and  $f_i$  denote the amplitude of the current change and the frequency, the expression of the total HGR inside the cell (Eq.(5)) becomes:

$$\dot{Q}_{total}(t) = -\Delta I \cdot \sin(2\pi f_i t) \cdot T \cdot \frac{dU_{oc}}{dT} + (\Delta I)^2 \cdot \sin^2(2\pi f_i t) \cdot R \quad (31)$$

The function in frequency domain by Fourier transform results in:

$$\begin{aligned} \mathfrak{F}[\dot{Q}_{total}(f)] &= -i \frac{\Delta I T}{2} \frac{dU_{oc}}{dT} \cdot [\delta(f + f_i) - \delta(f - f_i)] \\ &+ \frac{(\Delta I)^2 R}{4} \cdot [-\delta(f + 2f_i) + 2\delta(f) - \delta(f - 2f_i)] \end{aligned} \quad (32)$$

Eq. (23) includes two terms, and indicates that by applying a sinusoidal current excitation to the cell, the reversible heat source includes the first harmonic frequency  $f_i$  while the irreversible heat source contains the second harmonic frequency  $2f_i$ . Therefore, separation of the two parts is possible by analyzing their frequencies in the frequency domain. In addition, the entropy coefficient and internal resistance of the cell are the key parameters for reversible and irreversible heat and are further identified.

As shown in Eq. (23), the Fourier coefficient of  $f_i$  contains the expression of entropy coefficient, which is used to determine the value of the entropy coefficient from the amplitude of the frequency:

$$\left| \frac{dU_{oc}}{dT} \right| = \left| \frac{2}{\Delta IT} P(f_i) \right| \quad (33)$$

, where  $P(f_i)$  denotes the amplitude of the frequency of  $\Im[\dot{Q}_{total}(f)]$  at  $f=f_i$ .

Similarly, the sign of the entropy coefficient is determined from the phase angle at the frequency  $f_i$ :

$$\text{sgn} \left[ \frac{dU_{oc}}{dT} \right] = \text{sgn} [\angle PA(f_i)]. \quad (34)$$

, where  $\angle PA(f_i)$  denotes the phase angle in radian at  $f=f_i$ . Thus, the entropy coefficient can be calculated as follows:

$$\frac{dU_{oc}}{dT} = \text{sgn} [\angle PA(f_i)] \cdot \left| \frac{2}{\Delta IT} P(f_i) \right|. \quad (35)$$

On the other hand, the Fourier coefficient of  $2f_i$  contains the expression of internal resistance, which is used to determine the value of the internal resistance:

$$R = \frac{4|P(2f_i)|}{(\Delta I)^2}. \quad (36)$$

### 3.4.2 Experiments

#### 3.4.2.1 Cell and test station

The battery cell used for the experiments and the test station is the same as those described in Section 2.3.1.

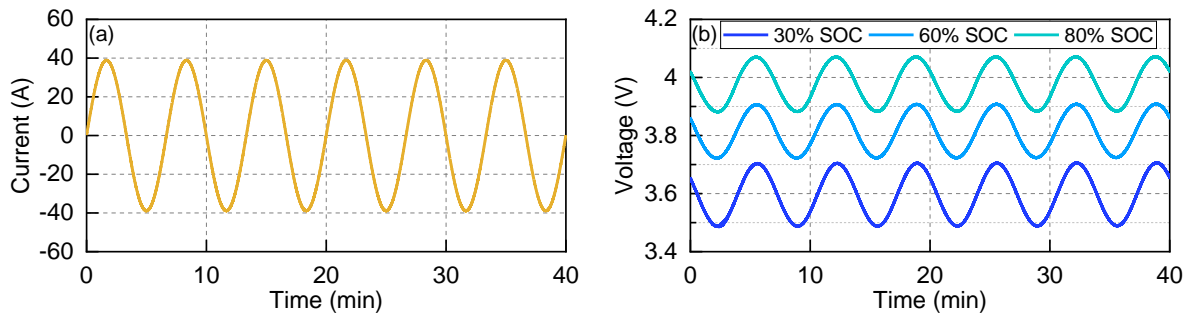
#### 3.4.2.2 Experiments procedure

The characterization of the reversible and irreversible heat sources was performed at 25 °C using the calorimetric method previously described. Initially, the cell was set to a specific SOC and a sinusoidal current was applied to the cell for six periods at different SOCs (10%, 20%,...90%), where  $\Delta I = 38.85\text{A}$  (1.5C) and  $f_i = 0.0025\text{Hz}$ . The values of the entropy coefficient and internal resistance were measured using the proposed method. The measured entropy coefficient result was compared with the one by the conventional potentiometric method as shown in Section 3.3.3.4. The measured internal resistance was compared with the conventional EIS analysis by summing up the Ohmic resistance, SEI resistance, and charge transfer resistance, which were extracted from the EIS-ECM.

### 3.4.3 Result and discussion

The two key parameters, entropy coefficient and internal resistance of the cell, are determined by experimentally measuring the two heat source terms using the proposed calorimetric method. The applied input sinusoidal current and the voltage response as output at

30%, 60%, and 80% SOC are plotted in Figure 23 (a) and (b). The corresponding HGRs of the cell are plotted in Figure 23 (c.1) ~ (e.1) in time domain, where the signal of the HGR contains an additional frequency to that of the input  $f_i$ . The corresponding frequency spectra are plotted in Figure 23 (c.2) ~ (e.2), where two peaks at the fundamental frequency  $f_i$  and the second order harmonics  $2f_i$  are observed. The peak at  $f_i$  corresponds to the reversible heat source, while the one at  $2f_i$  corresponds to the irreversible heat source.



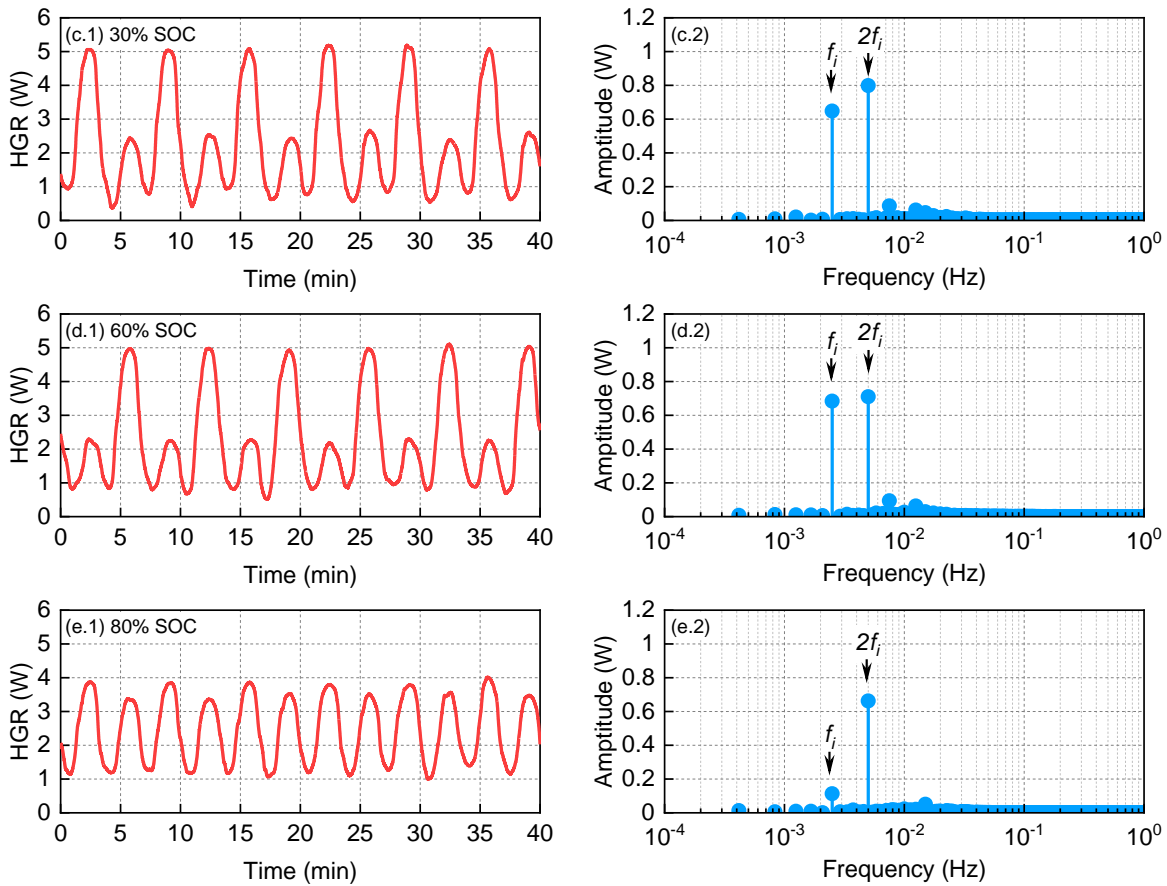


Figure 23. (a) Input current, (b) terminal voltage response, and measured HGR at (c.1) 30% SOC, (d.1) 60% SOC and (e.1) 80% SOC in time domain and the corresponding frequency spectra (c.2) ~ (e.2).

Based on Eq.(27) and (36), the values of the entropy coefficient and the internal resistance are calculated. The calculated entropy coefficient as a function of SOC was plotted in Figure 24 (a) with the blue dots. Its values range from  $-1.53 \times 10^{-4}$  V/K to  $1.18 \times 10^{-4}$  V/K in the SOC range of 10% to 90%, and its sign is altered around 40%, and 70% SOC, respectively, which indicates a transition between endothermic and exothermic reversible heat generation. In addition, the entropy coefficient – SOC profile measured by the potentiometric method is also plotted in Figure 24 (a) with the red dots, which delivers similar results including the shape, magnitude and inflection points. In fact, the proposed calorimetric method measures an averaged entropy coefficient over a

limited SOC range by the input current, which results in a slight shift of the curve position in the horizontal direction, as shown in Figure 24 (a).

Figure 24 (b) shows internal resistances at different SOC levels that are calculated by the proposed calorimetric method and characterized by EIS method. Both curves are in good agreement with each other, ranging from 1.71 m $\Omega$  to 3.01 m $\Omega$ , which is similar to those published [60], [61]. In addition, the internal resistance of the cell varies as a function of SOC, which generally increases as SOC decreases, which indicates that more irreversible heat is generated when the cell operates in the low SOC range.

The total testing time for the measurement of entropy coefficient and internal resistance by the conventional methods is approximately 15.2 h and 3.8 h per SOC point, respectively. However, the proposed calorimetric method is able to simultaneously determine the two parameters, and the overall testing time is reduced to 1.5 h per SOC, which saves 92% of the time cost by the conventional approaches.

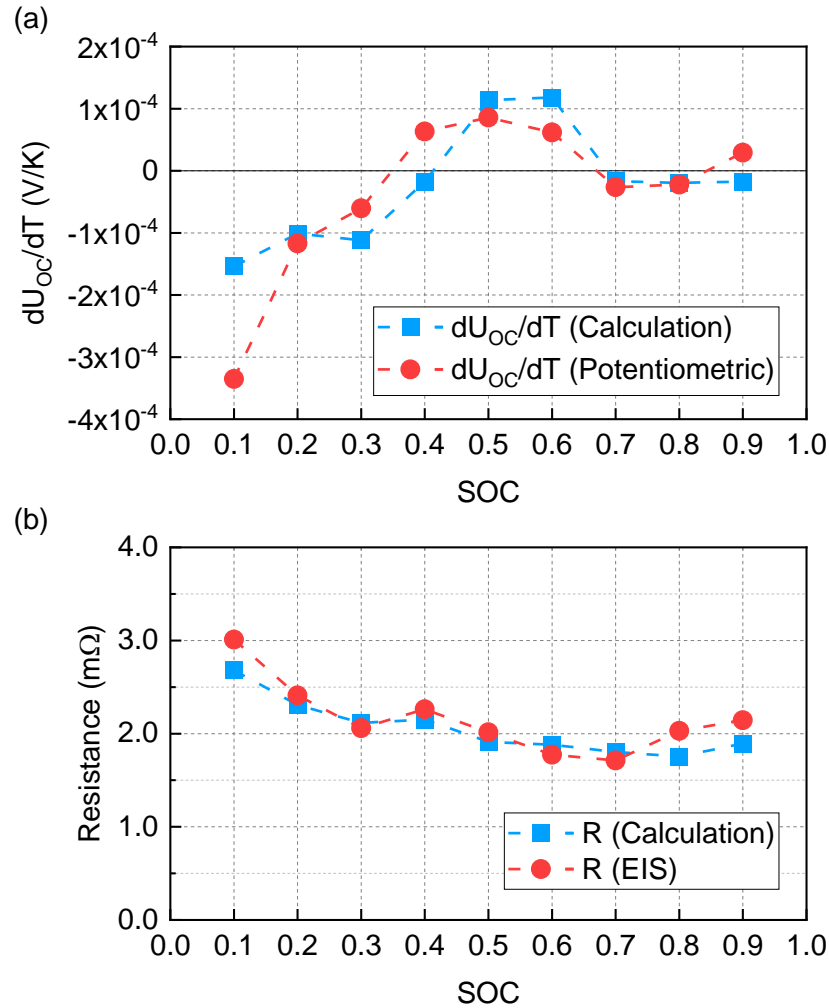


Figure 24. Calculated (a) entropy coefficient and (b) internal resistance as a function of SOC from the calorimetric method and comparison with those by potentiometric method and EIS method, respectively

The determined entropy coefficient and internal resistance of the cell are further verified by comparing the calculated reversible and irreversible heat generation with the experimental measured results. The cell was initially set to a specific SOC. After resting, a testing profile consisting of a 120s 2C discharge, 1h resting and 120s 2C charge was applied to the cell. The same setup of the calorimeter was used to separately measure the total heat generated during the discharge and charge while maintaining the temperature of the cell at 25 °C.

During discharging or charging process, the SOC changes by around 6.8%. Thus, it is assumed that the values of the entropy coefficient and internal resistance do not vary within such SOC window, so the irreversible heat during discharge and charge is identical, while the reversible one has the same amount but the sign is opposite. Then, the total heat generation during the discharging and charging process can be written as follows:

$$Q_{total-dch} = -I_0 \cdot T_0 \cdot \frac{dU_{oc}}{dT} \cdot \Delta t + I_0^2 \cdot R \cdot \Delta t = Q_{rev} + Q_{irr}, \quad (37)$$

$$Q_{total-ch} = I_0 \cdot T_0 \cdot \frac{dU_{oc}}{dT} \cdot \Delta t + I_0^2 \cdot R \cdot \Delta t = -Q_{rev} + Q_{irr} \quad (38)$$

, where  $I_0 = 51.8\text{A}$  (2C),  $T_0 = 298.15\text{K}$ , and  $\Delta t = 120\text{s}$ . The term  $Q_{rev}$  and  $Q_{irr}$  denote the reversible and irreversible heat during discharge, which can be determined by rearranging Eq.(37) and (38) to yield:

$$\begin{aligned} Q_{rev} &= (Q_{total-dch} - Q_{total-ch})/2 \\ Q_{irr} &= (Q_{total-dch} + Q_{total-ch})/2 \end{aligned} \quad (39)$$

The measurements were performed from 80% to 20% SOC with a step of  $\Delta\text{SOC}=10\%$ . At each SOC, the test was conducted three times, and an averaged total heat,  $Q_{rev}$  and  $Q_{irr}$  were determined. Then, the calculated reversible and irreversible heat is obtained by applying the determined parameters of entropy coefficient and internal resistance into Eq.(5). The results from the measurement and the calculation are plotted in Figure 25.

Figure 25 (a) shows the averaged total heat generation during the discharging and charging at each SOC, where the error bars represent the standard deviation. The heat generation of the cell

varies at different SOC's during the discharging and charging process. During discharging, the heat generation at high or low SOC ranges is greater than that at mid SOC's, and it becomes exactly opposite during charging, which is caused by the reversible heat generation of the cell, which has previously been seen to be endothermic or exothermic. In addition, the magnitude of the reversible heat generation depends upon the magnitude of the entropy coefficient. The value of the entropy coefficient at 60% SOC and 70% SOC is  $1.18 \times 10^{-4} \text{ VK}$  and  $-1.68 \times 10^{-5} \text{ VK}^{-1}$ , respectively, which is seven times as large at 60% as that at 70%. Accordingly, the absolute differences of the measured total heat between discharging and charging at 60% and 70% SOC are 0.34 kJ and 0.05kJ, respectively, which is also a factor of seven times greater in magnitude.

Figure 25 (b) shows the averaged values of each source for the discharging process, where the error bar indicates the standard deviation. At different SOC's, the heat generation caused by reversible and irreversible heat have different values. The irreversible heat is always positive and is a function of SOC that is similar to that of the internal resistance – SOC curve shown in Figure 24 (b). As for the reversible heat, its magnitude is lower than that of the irreversible heat, but the sign can be negative dependent upon SOC. In fact, from Eq.(5), the sign of the reversible heat is dependent on the sign of the applied current and the  $\frac{dU_{oc}}{dT}$ . The measured  $\frac{dU_{oc}}{dT}$ -SOC relationship in Figure 24 (a) shows that the value of  $\frac{dU_{oc}}{dT}$  is positive between 50% and 70% SOC, and is positive in the rest SOC range. Thus, for discharge ( $I > 0$ ), the reversible heat is negative during 50%~70% SOC, and becomes positive value at other SOC points. Since the measured internal resistance and entropy coefficient are average values within an SOC range of 6.8% at a given SOC point, the calculation error may occur due to the assumption that the values of the entropy coefficient and internal resistance do not vary within such SOC window.

The irreversible heat generation from the calculation and the measurement are plotted in Figure 25 (c), where two results are qualitatively similar. Additionally, the magnitude seen via measurement is smaller than calculated. The mismatch is a result of part of the heat generated stored in the battery [62], which is not compensated for in the proposed calorimeter.

In reality, when the cell is charged or discharged, part of the heat generation stored in the battery results in an increase in the internal temperature. The relationship between the actual ( $Q_{act.}$ ), measurable ( $Q_{mea.}$ ) and stored ( $Q_{sto.}$ ) heat can be expressed as:

$$Q_{act.} = Q_{mea.} + Q_{sto.} \quad (40)$$

Thus, the expression of the irreversible and reversible heat from Eq.(39) is modified to

$$\begin{aligned} Q_{mea.irr} &= \left[ (Q_{act.-dch} - Q_{sto.}) + (Q_{act.-ch} - Q_{sto.}) \right] / 2 = Q_{act.irr} - Q_{sto.} \\ Q_{mea.rev} &= \left[ (Q_{act.-dch} - Q_{sto.}) - (Q_{act.-ch} - Q_{sto.}) \right] / 2 = Q_{act.irr} \end{aligned} \quad (41)$$

Consequently, the amplitude of the measured irreversible heat is lower than that of the actual value, while the amplitude of the measured reversible heat should be equal to that of the actual value.

Finally, the reversible heat generation from the calculation and the measurement is compared in Figure 25 (d). Since the heat capacity does not affect the measurement of the reversible heat, the measurement results tend to follow the calculation results, where the highest exothermal and endothermal reversible heat are at 20%-30% SOC and 50%-60% SOC, respectively. However, there are some discrepancies in the magnitude caused by the inherent errors of the simplified

thermal model of the battery, errors of the measured entropy coefficient, and the assumed average entropy coefficient for calculation.

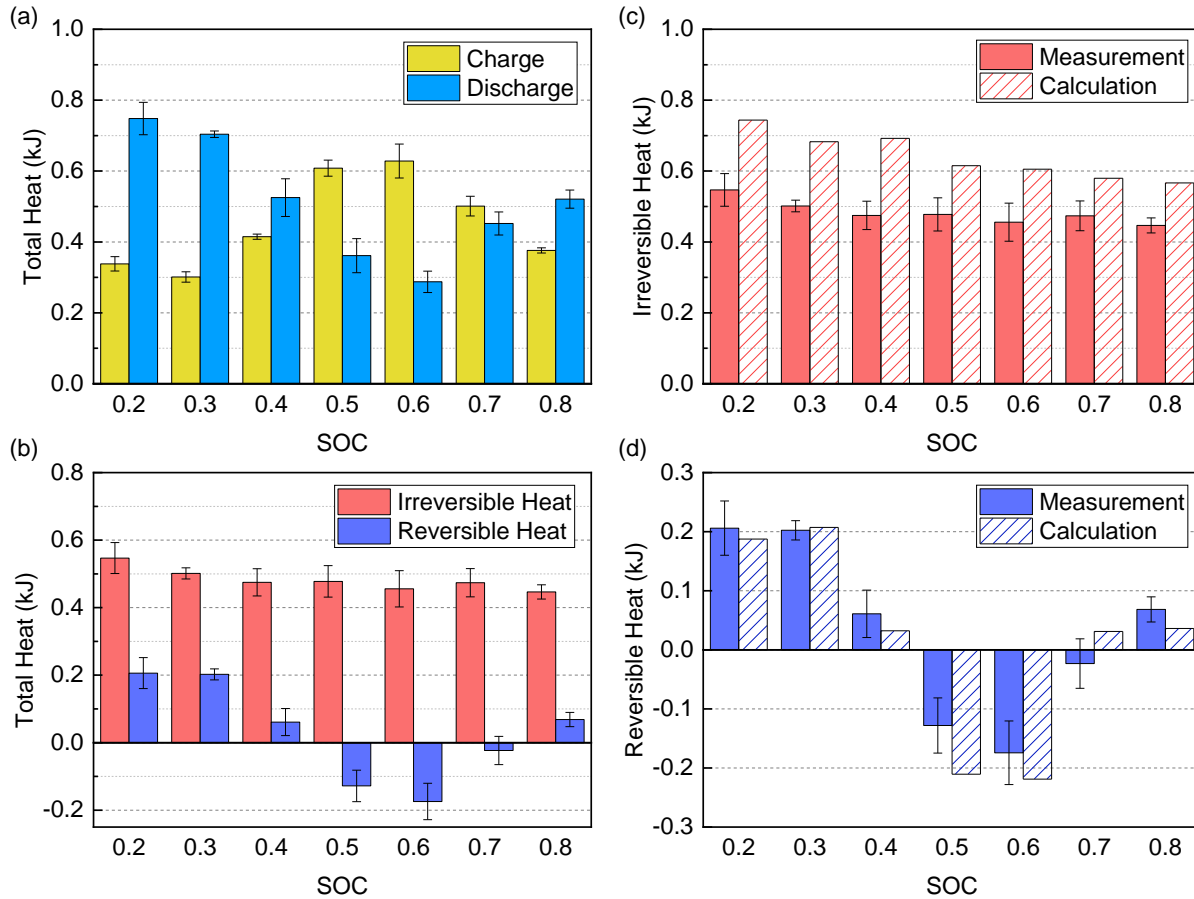


Figure 25. Measured (a) total heat during discharge and charge and (b) irreversible and reversible heat during discharge. Comparison between the calculated and measured (c) irreversible and (d) reversible heat during discharge.

### 3.4.4 Summary

The proposed calorimetric method provides a fast and accurate tool for determination of entropy coefficient and internal resistance, which saves 92% of testing time compared with the conventional methods.

### 3.5 Wavelet-transform based simultaneous and continuous characterization method

As a matter of fact, the entropy coefficient continuously varies as a function of SOC. Those classical methods and the newly proposed ones in the previous sections can only determine the entropy coefficient at given SOC, which results in discrete values. Thus, interpolations of the values are needed for applications like modeling where continuous values are preferred. There are some suggestions for a continuous measurement of entropy coefficient by applying an electrothermal impedance spectroscopy (ETIS) with piecewise Fourier transform [31]. The heat generation is estimated by the variation of surface temperature of the cell with a thermal transfer function that requires a significant amount of experiments in advance. In addition, the Fourier transform requires a proper length of the windowed piece of the data. In fact, a large piece of data reduces the time resolution while a small piece has a drawback in analyzing low frequency responses [63]. On the other hand, the internal resistance measured from the abovementioned approaches is also discrete with respect to SOC points.

In this section, we propose an improved calorimetric method that enables simultaneous characterization of the two thermal parameters, where the resulting data is a continuous function of the SOC [64]. This method is based on the time-frequency domain analysis using wavelet transform technique and implemented into a previously developed high performance multifunctional calorimeter. The wavelet transform is the technique that analyzes time-series signals and simultaneously displays functions and their local characteristics in time-frequency domain. Basically, it expands targeted functions in terms of a set of basis functions, named as mother wavelets, where the temporal analysis is performed with a contracted, high-frequency version of the mother wavelet, while the frequency analysis is performed with a dilated, low-frequency version of the same wavelet [65].

This technique is used to simultaneously characterize the two thermal parameters. Firstly, a cell is mounted in the calorimeter, where a sinusoidal AC-current superimposed with a small DC current is applied and the heat generation rate as a response is measured. The measured heat generation rate profile is processed by the continuous wavelet transform, which delivers the entropy coefficient and internal resistance as a function of SOC. The results are compared with those measured by the conventional potentiometric method and EIS analysis, respectively. In addition, the determined parameters are applied to a simplified battery thermal model for the calculation of the total heat generation.

### 3.5.1 Principle

In Section 3.4.1, we have illustrated that the reversible and irreversible heat can be easily separated in the frequency domain, and the corresponding parameters: entropy coefficient and internal resistance are expressed as the amplitudes of the terms in Eq.(32).

The wavelet analysis technique is a powerful tool to detect and analyze non-stationary time-series signals by decomposing the signals into a time-frequency space [66]. The wavelet transform has two basic transform features: continuous wavelet transform (CWT) and discrete wavelet transform (DWT). CWT is more suitable for extraction of a signal feature while DWT is for data compression and signal de-noising processing applications [67]. Therefore, the CWT technique was selected for analysis of the heat generation response of the cell, which allows simultaneous analysis of the heat generation signal in both frequency and time domain.

The CWT analyzes the signals using wavelet basis functions, called mother wavelet in two aspects: (a) temporal analysis performing with a contracted, high-frequency version of the mother

wavelet and (b) frequency analysis performing with a dilated, low-frequency version of the same wavelet. The mother wavelet is generally expressed as:

$$\psi_{a,b}(t) = \frac{1}{\sqrt{a}} \psi\left(\frac{t-b}{a}\right) \quad (42)$$

, where  $a$  and  $b$  denote the scaling and shifting parameters of the mother wavelet function, which represent the factor of the translation and the center of the mother wavelet, respectively and  $t$  is the time coordinate.

The CWT projects the time-domain heat generation signal on the mother wavelet function at different parameter sets, resulting in the wavelet coefficient that describes the correlation between the heat signal and the mother wavelet function, which is expressed as:

$$W_{a,b}(\tau, s) = \int_{-\infty}^{\infty} \dot{Q}_{total}(t) \cdot \psi_{a,b}^* dt \quad (43)$$

, where  $\tau$  and  $s$  denote the position of a wavelet in time and frequency domain, and  $*$  denotes a conjugated complex number.

Eq.(23) includes the modulus of the wavelet coefficient at frequency  $f_i$  that is used to determine the magnitude of the entropy coefficient as a function of time, while the sign of the entropy coefficient is calculated from the phase angle between  $I(t)$  and the corresponding  $\dot{Q}_{total}(t)$  signal at frequency  $f_i$ . Thus, the entropy coefficient is determined as follows:

$$\frac{dU_{oc}}{dT}(t) = \text{sgn}\left[\left|\angle PA(t, f_i)\right| - \frac{\pi}{2}\right] \cdot \frac{2}{\Delta IT} \|W_{a,b}(t, f_i)\| \quad (44)$$

, where  $|\angle PA(t, f_i)|$  denotes the absolute value of the phase angle in radian at time  $t$  and frequency  $f_i$ .

In Eq.(22), the phase angle is either  $\pi$  or 0 should the sign of the entropy coefficient be positive or negative. In real experiments, there has been a time delay between the current and the heat generation because of the cell's heat capacity, which leads to a slight deviation of the phase angle around its expected value.

On the other hand, the value of the internal resistance as a function of time can be determined from the amplitude of the wavelet coefficient at frequency  $2f_i$ :

$$R(t) = \frac{4}{(\Delta I)^2} \|W_{a,b}(t, 2f_i)\| \quad (45)$$

The simultaneous and continuous characterization of reversible and irreversible heat sources is accomplished by offsetting the sinusoidal AC-current with a small DC current ( $I_0$ ) that serves to continuously change the SOC of the cell. The value of the DC-current should be relatively small, so that its effects on the overall time-frequency domain analysis can be neglected. Then, the SOC as a function of time is calculated by:

$$SOC(t) = SOC^0 - \frac{\int_0^t I_0(\tau) d\tau}{Q_{max}} \times 100\% \quad (46)$$

, where  $SOC^0$  and  $Q_{max}$  denotes the initial SOC and the maximum capacity.

Using Eqs. (44)-(46), the entropy coefficient and internal resistance as a function of SOC is simultaneously and continuously obtained.

### 3.5.2 Experiment

#### 3.5.2.1 Cell and test station

The battery cell used for the experiments is the same as those described in Section 2.3.1. The schematic diagram of the test station is shown in Figure 26. In order to generate a sinusoidal current signal, a power supply is connected to an electronic load in parallel as a combined current source. The power supply outputs a DC current, while the electronic load generates a sinusoidal current load with a compensated DC offset, which is the same magnitude but opposite sign to the one generated by the power supply. Thus, it can be assumed that the sinusoidal current is ideal whose maximum amplitude and frequency can go up to 100A and 10Hz. During the tests, the terminal voltage and the surface temperature of the cell are measured and collected. Measurements of heat generation rate are carried out using the multifunctional calorimeter.

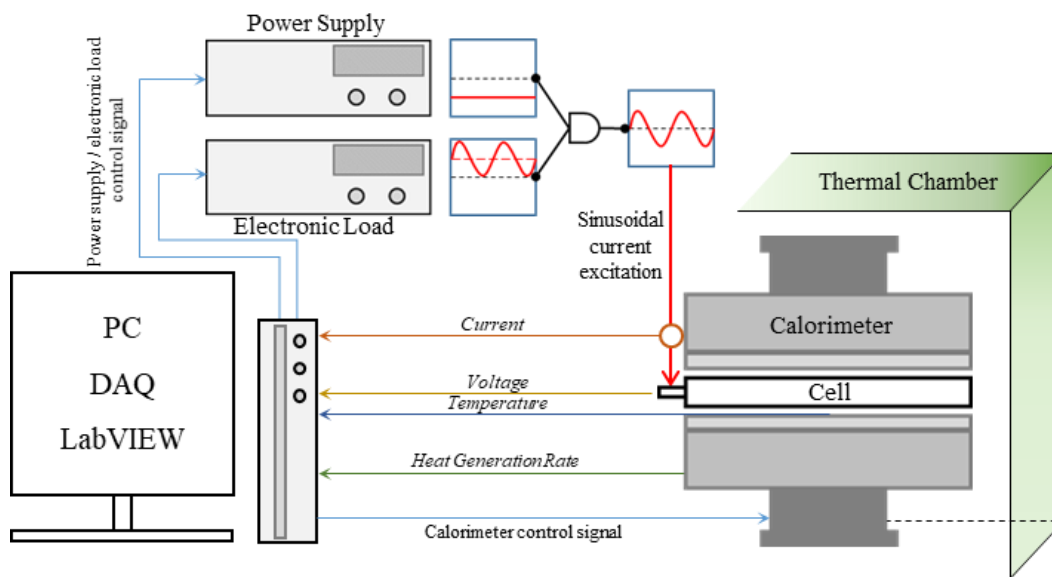


Figure 26. Schematic diagram of the test station

### 3.5.2.2 Experiments procedure

The cell to be tested was placed in the calorimeter located in a thermal chamber, where the ambient temperature is set to 25°C. Initially, the cell was fully charged at 25°C using C/3 CC-CV protocol, discharged with C/3 to reach 90% SOC, and rested for an hour to let it reach equilibrium. The starting SOC point of the measurement was at 90% instead of 100% in order to prevent the cells from overcharging during the first cycles of the sinusoidal current excitation, which was selected by rough estimation. To start the measurement, a sinusoidal AC-current with a discharge DC-current offset was applied to the cell until the terminal voltage reached the cutoff value. The amplitude and the frequency of the sinusoidal AC-current profile were  $\Delta I = 38.85\text{A}$  (1.5C) and  $f_i = 0.0025$  Hz, respectively. The DC-current continuously changes the SOC of the cell and its amplitude is selected with a small value of 1.295A (C/20) that should not adversely affect the overall time-frequency domain analysis. The experimental procedure took a total time of 17.3 hrs. The input current and the corresponding terminal voltage, heat generation rate and the surface temperatures of the cells were recorded with a sampling frequency of 10 Hz. The relationship of the two parameters as a function of SOC was continuously and simultaneously calculated using the built-in functions of MATLAB, *cwt* and *wcoherence* for the calculation of the wavelet coefficient and phase angle, respectively.

For comparison, the parameters are also measured at 25°C by the conventional potentiometric method and EIS test respectively as references, which has been discussed in previous sections.

### 3.5.3 Result and discussion

The measured three waveforms of the input current (a), terminal voltage (b) and heat generation rate (c) are plotted in Figure 27. In this section, the discharging current is defined as positive, and the charging current as negative. The input current includes a sinusoidal AC current superimposed by a small DC-current offset. The terminal voltage is a continuous waveform, a decaying quasi-sinusoidal oscillation, as shown in Figure 27 (b). This phenomenon becomes more apparent at low SOC range, where the terminal voltage decreases rapidly. The measured heat generation rate, as plotted in Figure 27 (c) varies continuously, but contains an additional frequency besides the excitation frequency of the input current, whose shape and the magnitude are varying at different time steps. The full profile of the heat generation rate is plotted in Figure 28.

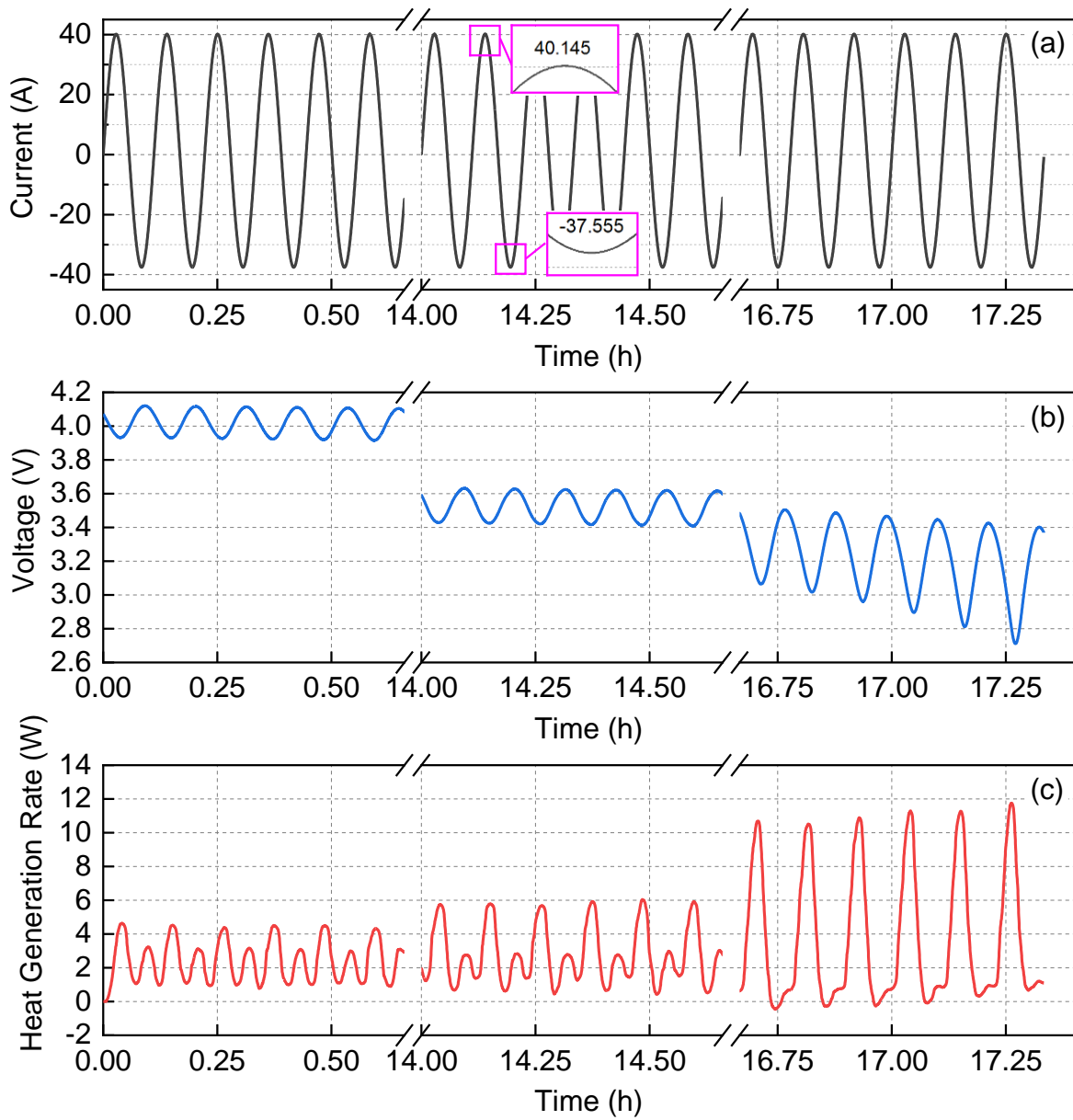


Figure 27. (a) Input current and corresponding response of (b) terminal voltage and (c) heat generation rate at 25°C.

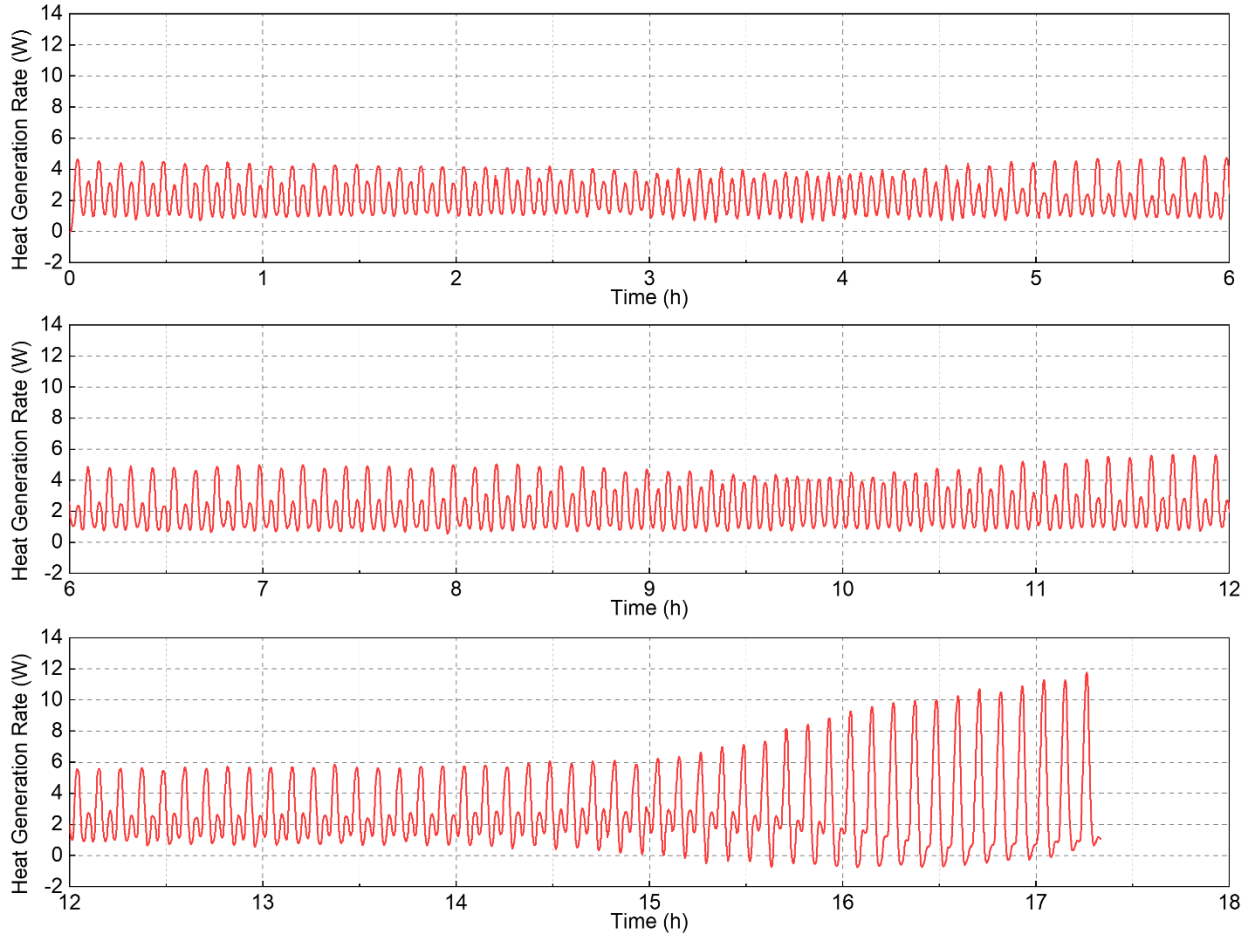


Figure 28. Full profile of heat generation rate.

Prior to the application of the wavelet analysis on the measured time-series heat generation rate profile, a proper mother wavelet function and associated parameters should be selected, which is basically based on the signal characteristics and the nature of the applications. Currently, several types of mother wavelets are being widely employed for computing the CWT, including the Morlet [66], Morse [68] and bump wavelet [69]. In this work, the bump wavelet is selected as the mother wavelet due to its high performance in time-frequency analysis, specifically for oscillatory signals analysis [70]. The bump wavelet is a symmetric function in frequency [71], defined in the Fourier domain as [72]:

$$\psi(s\omega) = \exp\left(1 - \frac{1}{1 - (s\omega - \mu)^2 / \sigma^2}\right) \cdot \chi\left[\frac{(\mu - \sigma)}{s}, \frac{(\mu + \sigma)}{s}\right] \quad (47)$$

, where  $\chi$  is the indicator function, with the parameters  $\mu \in [3, 6]$  and  $\sigma \in [0.1, 1.2]$  governing the resolution in time and frequency domain. Smaller values of  $\sigma$  result in a wavelet with superior frequency localization but poorer time localization, while larger values produce a wavelet with better time localization but poorer frequency localization. In this work, we set the  $\mu = 5$  and  $\sigma = 0.6$ , which are the default values of MATLAB built-in functions. (For different types of lithium-ion cells, some parameter tuning process might be needed in order to obtain a clear time-frequency representation plot.)

The measured heat generation rate response in Figure 27 (c) has 623,990 time-series data points that is processed to obtain the wavelet coefficient  $W_{a,b}(t, f_i)$ . After the CWT, a  $149 \times 623,990$  wavelet coefficient matrix is obtained. Then, the modulus of the wavelet coefficient is calculated and plotted as a function of time and frequency, which is shown as the scalogram in Figure 29 (a), where the x-axis and the y-axis represent time in the unit of hour and the frequency in a logarithmic scale. The cone of influence that shows the areas where edge effects become significant is also plotted in the figure as the gray regions outside the dashed white line. In Figure 29 (a), two linear bright regions are observed at frequencies of  $f_i = 0.0025$  and  $2f_i = 0.0050$  Hz, which indicates that the main energy of the heat generation rate waveform is concentrated exactly at the fundamental frequency ( $f_i$ ) and the second order harmonics ( $2f_i$ ) of the sinusoidal current excitation, which corresponds to the reversible and irreversible heat sources, respectively.

In addition, the magnitude of the wavelet coefficient modulus at  $f_i$  and  $2f_i$  varies with time, which indicates that the amplitude of the cell's entropy coefficient and internal resistance are

dependent on the SOC. Specifically, the bright region at  $f_i$  shows two zero points of the wavelet coefficient modulus near 4.2 h and 10 h, which reveals that the cell's entropy coefficient at these two time points are approaching zero.

Moreover, both of the modulus of wavelet coefficients at  $f_i$  and  $2f_i$  show increased values at the end of operation, which indicates a high absolute value of entropy coefficient and internal resistance at low SOC ranges.

The wavelet coherence between the heat generation rate waveform and the input current in a time-frequency plane is plotted in Figure 29 (b) from a calculated  $271 \times 623,990$  wavelet coherence matrix. The coherency of the two signals ranges from the blue (low coherency) to the yellow color (high coherency), and the phase angle between the two signals is represented by the direction of arrows on a unit circle, which ranges from  $-\pi$  to  $\pi$ . For example, a horizontal right arrow indicates a zero rad, while a horizontal left arrow does a  $\pm\pi$  rad. Particularly, the heat generation rate signal and the input current are highly coherent at  $f_i=0.0025$  Hz with the value of the coherence approaching 1. The result coincides with the theoretical expression of the cell's reversible heat generation rate in Eq. (5), which shows a linear relationship to the current. In addition, in the time range between 0–4.2 hrs and 10–17.3 hrs, the arrows are in the right direction, which indicates a positive correlation between the heat generation rate signal and the input current, and as a result, a positive value of the entropy coefficients. Conversely, the negative entropy coefficients are determined in the 4.2–10 hrs range from the leftward arrows.

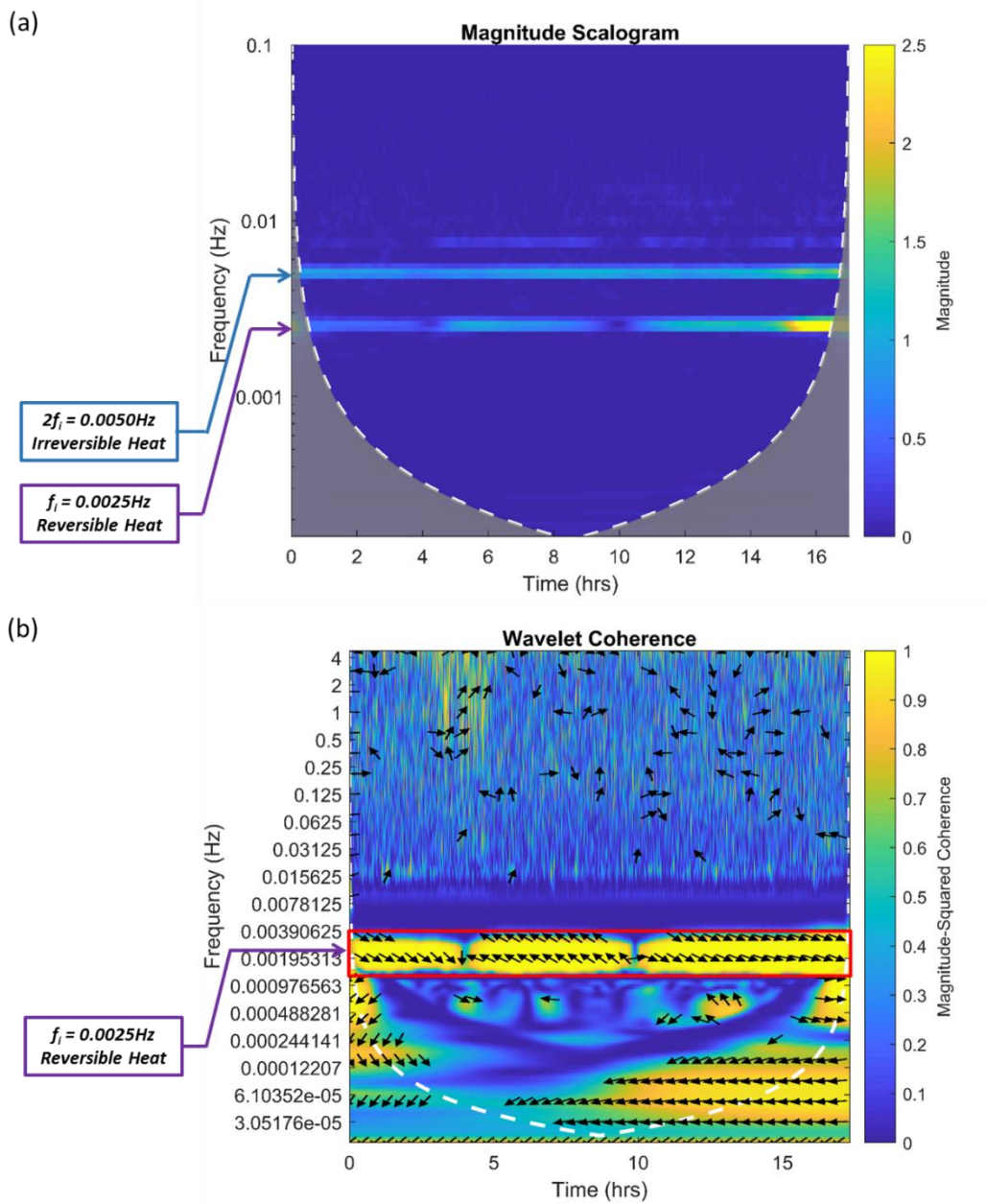


Figure 29. Scalogram of (a) modulus of wavelet coefficient by the CWT of heat generation rate and (b) wavelet coherence between heat generation rate and input current

Based on the wavelet analysis results above and the calculation expressions in Eqs (44)–(46), the variation of the entropy coefficient and internal resistance as a function of SOC are determined and plotted as the light blue solid lines in Figure 30 (a) and (b), respectively. Thanks to the

continuity of the estimated data for the two parameters, the plot becomes continuous and smooth over the operating SOC range. The grey regions at the high and low SOC ranges represent the areas where the edge effects of the wavelet transform become significant. Thus, the data located within these regions include the inevitable calculation errors and should be discarded.

For comparison, the entropy coefficient by the potentiometric method and the internal resistance by the EIS are also plotted in Figure 30 (a) and (b) as a reference. It is obvious that both data points are only at discrete SOC points, as plotted by the blue dots in Figure 30 (a) and (b).

Results have shown that the waveform of the two parameters by the proposed method are in good accordance with the reference values. More specifically, as shown in Figure 30 (a), the entropy coefficient measured by the proposed wavelet analysis ranges from  $-4.29 \times 10^{-4}$  V/K to  $9.38 \times 10^{-5}$  V/K, which is quantitatively consistent with the results by the potentiometric method that is within the range of  $-3.67 \times 10^{-4}$  V/K to  $9.14 \times 10^{-5}$  V/K. In addition, the sign of the entropy coefficient measured by the two methods has shown the same alteration in the range of 62.5–70.0% and 37.5%–41.3% SOC, which indicates the transition between endothermic and exothermic of the reversible heat. In Figure 30 (b), the values of the cell's internal resistance determined by the proposed method change from 1.60 to 2.93 m $\Omega$ , while the one by EIS is fluctuating within the range of 1.71–3.01 m $\Omega$ . In addition, the resistance generally increases as SOC decreases, which indicates that more irreversible heat is generated when the cell operates at low SOC ranges.

The total testing time by the classical two methods for the parameters has taken around 339 hrs, resulted from 304 hrs by the potentiometric method and 35 hrs by EIS tests. In contrast, the measurement time by the proposed method has taken only 17.3 hrs, which is only 1/20 of that by the classical method. The computational time for the post data processing by the wavelet transform calculation is around 80.5 s on a PC with a 3.70 GHz Intel Xeon E3-1240 CPU and a 16 GB RAM.

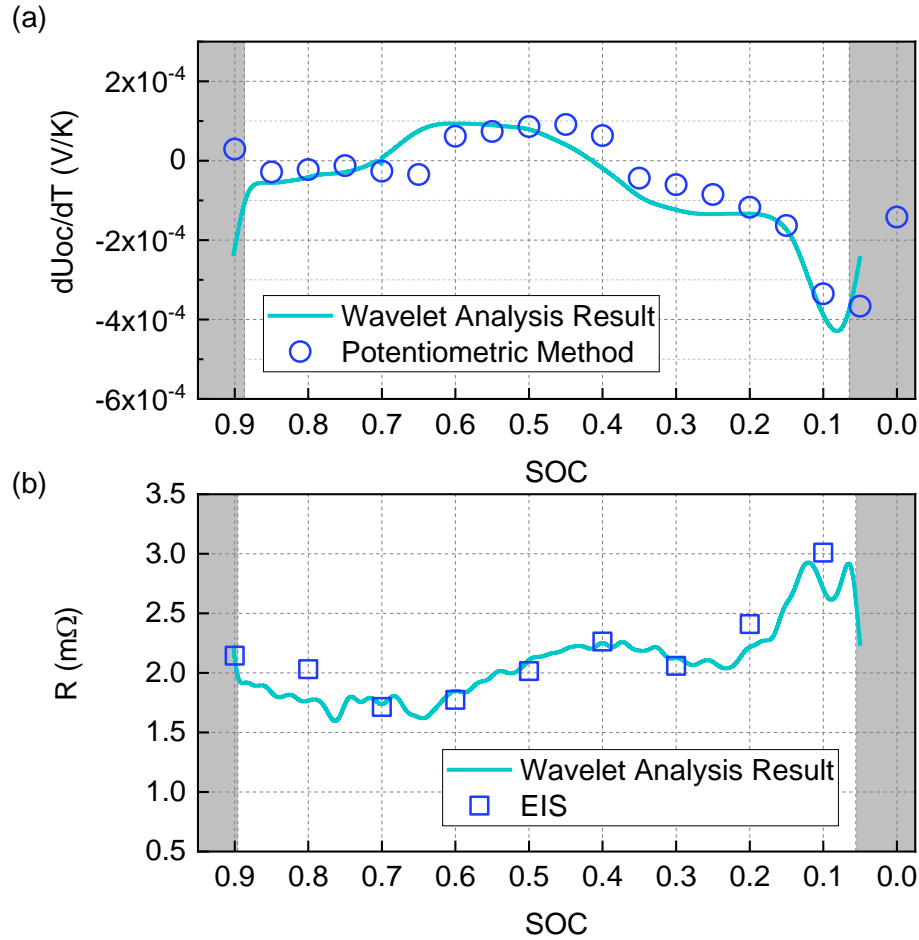


Figure 30. Calculated (a) entropy coefficient and (b) internal resistance as a function of SOC from the wavelet analysis result and comparison with those by potentiometric and EIS method, respectively. Grey regions represent the data with errors caused by the edge effects of wavelet transform.

After the entropy coefficient and the internal resistance of the cell are determined, the heat generation rate using Eq. (5) is calculated and then compared with the experimentally measured data for verification. Under consideration of the minimum resolution of the developed calorimeter, relatively high heat generation is desirable by increased C rates. However, high C rates result in dominance of the irreversible heat, so the reversible heat cannot be effectively studied. Therefore, 1C CC charging and discharging is chosen and the cell's total heat generation rate is measured at 25°C. The range of SOC considered was from 0% to 100%.

Figure 31 (a) and (b) show comparison of calculated and measured heat generation rate as a function of SOC. The total heat generation rate from the simple model and the experiment is plotted as orange solid lines and blue solid lines. The grey regions are the ranges with errors caused by the edge effects of wavelet transform.

The comparison has shown a similar shape within the SOC range from 6% to 89%. When the cell is discharged under 1C, the heat generation rate increases at the beginning, decreases slightly in the mid-SOC range, and then increases again to the maximum value at the end of discharging. In addition, the overall thermal behavior of the cell under 1C discharge is an exothermic process. The calculation profile basically shows the trend of the heat generation rate fluctuation including the local maximum and minimum points at around 30% and 20% SOC, respectively, and the overall tendency and magnitude. However, there is a discrepancy and hysteresis between the measurement and calculation curves that might be caused by the inherent errors of the simplified thermal model of the battery, and the complex heat transfer mechanisms within the cell. As for the charging process, the heat absorption takes place at the beginning of charging until the cell is charged to around 13% SOC, and then heat generation starts. The heat generation rate reaches a peak near 52% SOC and decreases slightly in high SOC ranges.

The calculated profiles can represent the features of the heat generation rate profile such as the transition between endothermic and exothermic process and the overall tendency, albeit some discrepancy and hysteresis exist. Calculation of both separate heat generation rates based on Eq. (5) as plotted as grey and black dashed lines respectively in Figure 31 (a) and (b) has shown the irreversible heat is exothermal and has the same amplitude at a given SOC point regardless of charge flows. In contrast, the reversible heat generation is endothermal or exothermal at different SOC, and the sign at a given SOC point is reversed when the cell is switched from discharging to

charging. In addition, the shape of the irreversible heat generation rate profile is flat, while the one of the reversible heat generation shows significant fluctuation, which implies that the reversible heat mainly attributes to the shape of the total heat generation profile. Potentially, the thermal behaviors might be changing at different C rates and degree of degradation, which will be further studied in the future.

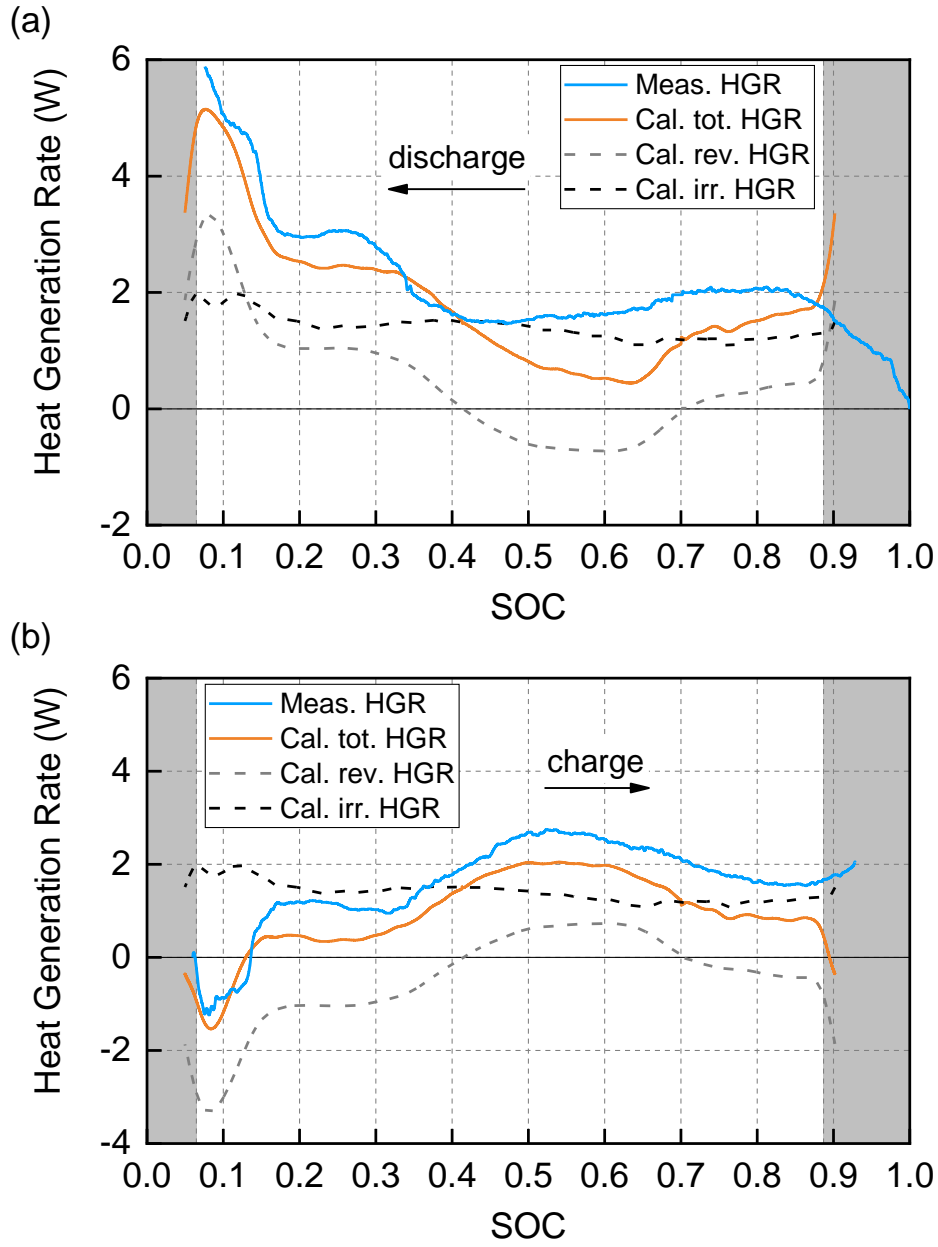


Figure 31. Comparison of measured and calculated heat generation rate under (a) 1C discharge and (b) 1C charge. Grey regions for erroneous data caused by the edge effects of wavelet transform.

### 3.5.4 Summary

In this section, we proposed a fast and continuous characterization method for simultaneous measurement of the entropy coefficient and internal resistance of the lithium-ion battery that are

the key two parameters needed for calculation of the reversible and irreversible heat sources. The method is developed based on the time-frequency domain analysis by wavelet transform technique and is incorporated into the developed multifunctional calorimeter. A large format LMO/NMC-graphite pouch type lithium-ion cell is used for the experiment, where a sinusoidal AC-current superimposed by a small DC current is applied and the heat generation as a response is measured by the calorimeter. The measured time-series heat generation rate profile is processed by the CWT, and the entropy coefficient and internal resistance as a function of SOC are obtained. The results of the entropy coefficient and internal resistance are compared with those measured by the conventional potentiometric and EIS methods, respectively. In addition, the determined parameters are applied to a simplified battery thermal model for the calculation of the total heat generation. The comparison of both results has shown a good agreement in the shape and tendency. The testing time by the proposed method has taken around 5% of that by the conventional approaches.

4.1 Model development

4.1.1 Electrochemical model

The electrochemical model of lithium-ion cells describes the cell's physical behavior by the principles of diffusion, mass transport, electrochemical kinetics, and Ohm's laws. Figure 32 shows the description of electrochemical model of lithium-ion battery along with the governing equations. The detailed list of PDEs with boundary conditions and the coupled nonlinear algebraic equation are shown in Table 1 in section 3.2.1.1.

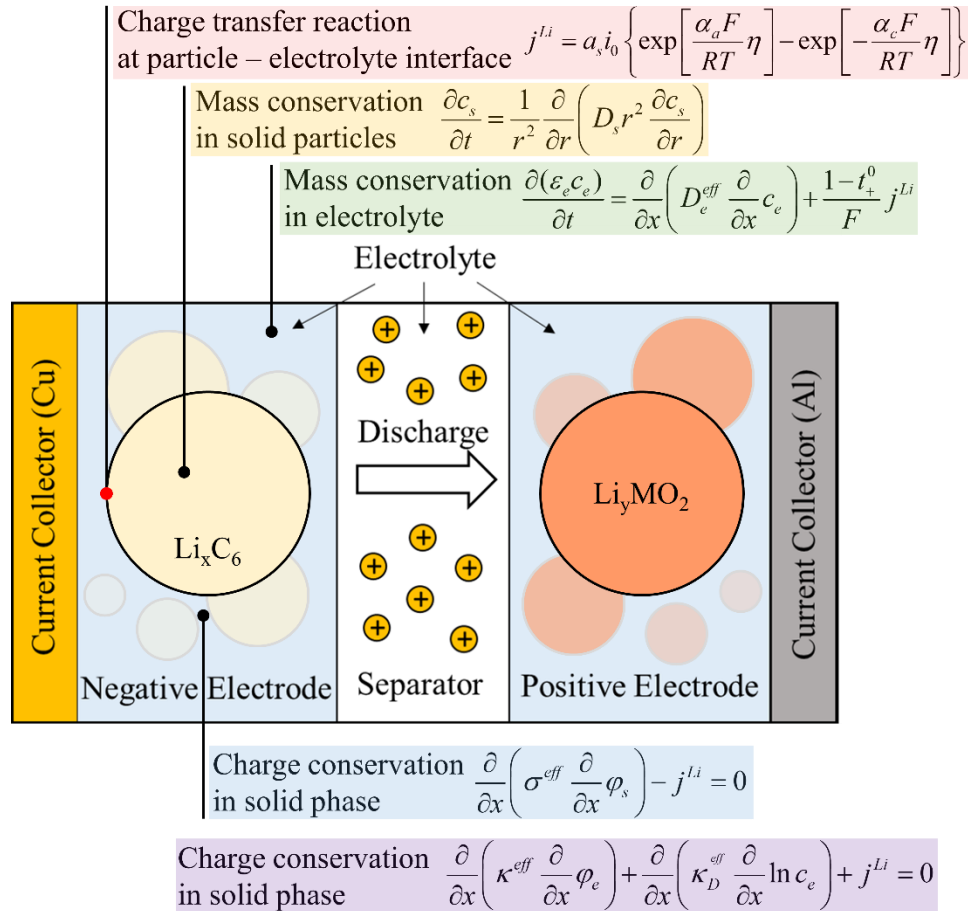


Figure 32. Description of electrochemical model of lithium-ion battery

#### 4.1.2 Degradation model

The lithium-ion batteries degrade as a result of the severe operation conditions, which leads to the byproducts production, morphology and structure change, and further affects the cell's performance such as the stored capacity, output power, and so on. Degradation process in lithium-ion cells originates from multiple complex mechanism in both electrode, electrolyte, separator and current collectors [78]. However, recent researches have revealed that the degree of degradation occurred at anode plays a significant role, which includes two dominant side reaction mechanism: (1) formation of SEI and (2) lithium plating. The SEI formation results from the electrolyte decomposition reaction, which is accelerated at high temperature and high current charging process, while the lithium plating usually takes place when the cell is charged under high current and low temperature, where lithium ions are prompted to form metallic lithium at anode. Figure 33 includes the chemical reactions of the SEI formation and lithium plating, and the associated expressions of the modeling.

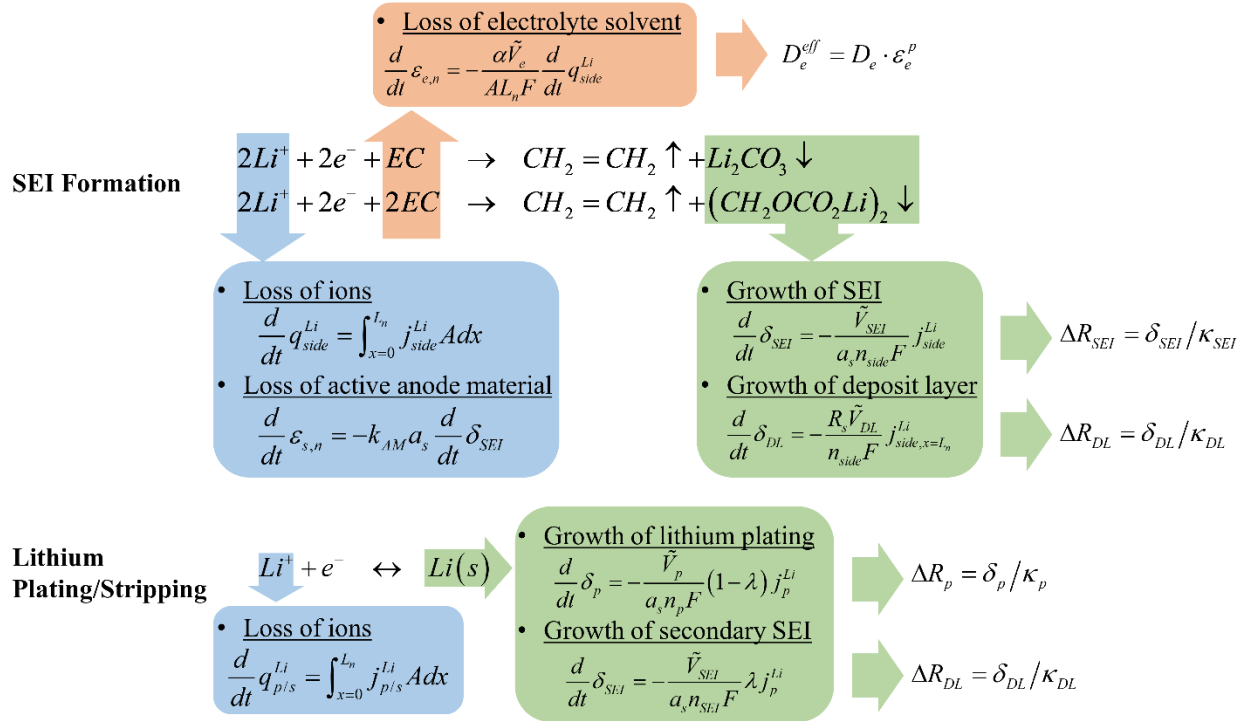


Figure 33. Description of degradation model considering side reaction and lithium plating/stripping.

#### 4.1.3 Thermal model

During the charging and discharging, heat is generated due to charge transport, chemical reactions, and intercalation and deintercalation process within the cell. Some of the generated heat is transferred to the ambient environment or a cooling system, but the remaining heat generated raises the temperature within the cell. The heat generated within the cell can be modeled by an electrochemical-model-based thermal model, which includes reversible heat, irreversible heat and heat of mixing. The reversible heat is generated by the change of entropy. The irreversible heat is comprised by Ohmic heat due to the resistance in solid particles, electrolyte, contact resistance and SEI resistance, and electrochemical reaction heat cause by the charge transfer reaction at the interface between the particles and electrolyte. The heat of mixing is caused by the transient behavior of ion concentration and the nonlinearity of equilibrium potentials in electrodes. Since

the amount of heat of mixing is small enough, it is often neglected in the modeling of the thermal behavior of the cell. Figure 34 shows a detailed description of the cell's thermal model.



$$\begin{aligned}
 \dot{Q} = & -\int j^{Li} T \frac{dU_{OC}}{dT} dV && \text{Entropy Change} \quad \text{-----} \quad \text{Reversible Heat} \\
 & + \int \sigma^{eff} (\nabla \phi_s)^2 dV && \text{Ohmic: Solid Phase} \\
 & + \int \kappa^{eff} (\nabla \phi_e)^2 dV && \text{Ohmic: Electrolyte phase} \\
 & + \int \kappa_D^{eff} \nabla \ln c_e \nabla \phi_e dV && \left. \begin{array}{l} \text{Ohmic: Contact resistance} \\ \text{Ohmic: SEI} \end{array} \right\} \text{Irreversible Heat} \\
 & + I^2 R_C \\
 & + \int (j^{Li})^2 \frac{R_{SEI}}{a_s} dV \\
 & + \int j^{Li} \eta dV && \text{Electrochemical reaction} \\
 & + \text{Heat of mixing (neglected)}
 \end{aligned}$$

Heat Source Terms →

Figure 34. Description of electrochemical-model-based thermal model based on

#### 4.2 Model validation and analysis

The developed electrochemical-thermal life model is validated by a pouch type lithium-ion battery cell whose specification is described in Section 2.3.1. The cells are aged by cycling with 2C charging and 4C discharging at 25°C. The capacity of the cells were measured with C/3 discharge rate at 25°C. After 200, 250, 300 and 325 cycles of the aging tests. The parameters of the battery model are shown in Figure 7.

Table 7. Parameters for lithium-ion cell electrochemical-thermal life model at 25°C

Parameter	Negative electrode	Separator	Positive electrode	Unit
$A$	11407		11407	cm <sup>2</sup>
$\delta$	$6.60 \times 10^{-3}$		$7.30 \times 10^{-3}$	cm
$R_s$	$1.07 \times 10^{-3}$		$1.75 \times 10^{-3}$	cm

$\varepsilon_s$	0.617		0.572	
$\varepsilon_p$	0.260	0.5	0.390	
$c_{s,max}$	0.031		0.050	mol cm <sup>-3</sup>
$c_e$	0.012	0.012	0.012	mol cm <sup>-3</sup>
$D_s$	4.0×10 <sup>-19</sup>		6.5×10 <sup>-9</sup>	cm <sup>2</sup> s <sup>-1</sup>
$D_e$	6.3×10 <sup>-6</sup>	6.3×10 <sup>-6</sup>	6.3×10 <sup>-6</sup>	cm <sup>2</sup> s <sup>-1</sup>
$\sigma$	5.3811		0.1982	S cm <sup>-1</sup>
$\kappa$	0.057	0.057	0.057	S cm <sup>-1</sup>
$\alpha_a, \alpha_c$	0.5		0.5	
$k$	12.9		6.28	(A cm <sup>-2</sup> )(cm <sup>3</sup> mol <sup>-1</sup> ) <sup>1.5</sup>
$Q_{max}$		25.8		Ah
$U_{eq,side}$		0.4		V
$\tilde{V}_{SEI}$		2		cm <sup>3</sup> mol <sup>-1</sup>
$\kappa_{SEI}$		2.5×10 <sup>-8</sup>		S cm <sup>-1</sup>
$\tilde{V}_{DL}$		7560		cm <sup>3</sup> mol <sup>-1</sup>
$\kappa_{DL}$		1.0×10 <sup>-3</sup>		S cm <sup>-1</sup>
$\tilde{V}_{DL}$		252		cm <sup>3</sup> mol <sup>-1</sup>
$U_{eq,p}$		0		V

Figure 35 (a) shows the experimental measured and simulated relative capacity of the cells as a function of different cycles. The relative capacity is defined as the ratio of the capacity at different cycles to that of the fresh cell. Result shows a good prediction of the cell's capacity at each cycle. The simulated terminal voltages and the associated heat generation rate at different cycles are compared with experimental results, as shown in Figure 35 (b) and (c). Results show

that the model can basically reflect the terminal behavior and heat generation responses of the cell from fresh to aged condition. The simulation error becomes larger after 325 cycles, which may be caused by the severe and complex degradation mechanism such as cracking, fracture, phase transition and structural changes at electrodes, which is not considered in this model.

Figure 35 (d) shows a comparison of total heat generation which is composed of the reversible and irreversible parts, at different aging conditions at 25 °C. As the cell gets aged from 0 cycles to 200 cycles, the total heat generation is slightly decreased because of the reduced discharging time by the capacity fade. However, when the cell was further aged to 325 cycles, the irreversible heat and the associated total heat generation increased, which is caused by the increased internal resistance caused by the degradation effects.

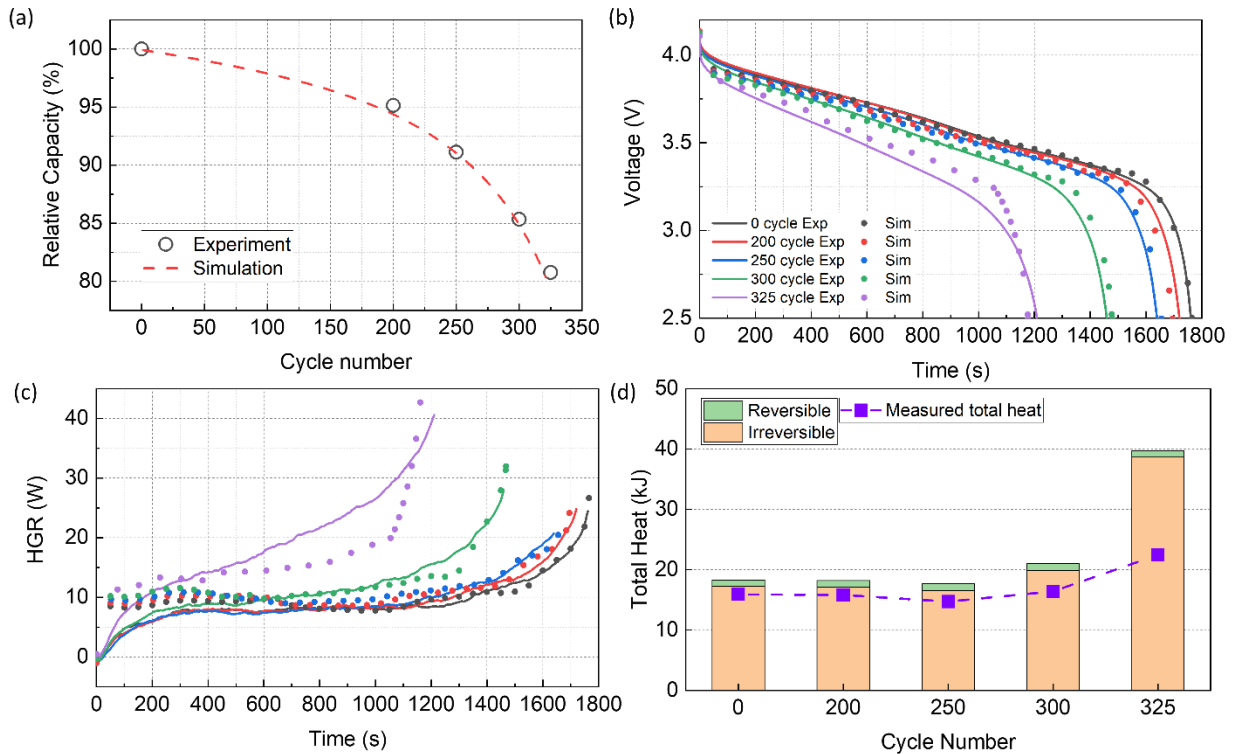


Figure 35 Model validation results: (a) capacity fade at 2C CC charging; comparison of discharging behaviors of (b) terminal voltage and (c) heat generation rate at 2C CC discharging; (d) total reversible and irreversible heat generation.

### 4.3 Summary

In this section, we present an electrochemical-thermal life model that estimates capacity fade, terminal voltage, heat generation rate at different degradation conditions. The model is developed using a physics-based electrochemical model of the cells, considering the SEI formation and lithium plating as sources of degradation, and describing the associated heat generation mechanisms caused by entropy change, Ohmic heat in solid phase, electrolyte phase, contact resistance, SEI resistance and reaction heat. The simulation results are validated by experimental data, and the heat sources are analyzed.

## Chapter 5. Improved battery electrochemical model considering variable diffusivity of lithium ions in solid

### 5.1 Literature review

When the cell is charged or discharged, the dynamic response of the terminal voltage, available power and actual capacity are affected by internal processes including ion transport, chemical reactions and intercalation and deintercalation, such as diffusion process of lithium ions, electronic conductivity and electrochemical kinetics. The most predominate process for dynamic behaviors of a cell is the diffusion that takes place in solid phase [79]. The associated parameter is the solid phase diffusivity (or diffusion coefficient),  $D_s$ .

In most of recent published papers, the diffusion coefficient in solid is regarded as a constant [73]-[76][77][80]. However, in reality, the diffusion coefficient of lithium ion, particularly in cathode particles, varies dependent upon temperature [81][82], cycling numbers [83], as well as ion concentration or SOC [84]-[87]. For example, experimental investigation on NMC532 ( $\text{Li}[\text{Ni}_{0.5}\text{Mn}_{0.3}\text{Co}_{0.2}]\text{O}_2$ ) [85] revealed that the diffusion coefficient of lithium ions in spherical cathode materials ranges from  $\sim 10^{-9} \text{ cm}^2 \text{ s}^{-1}$  at lithiated states to  $\sim 10^{-11} \text{ cm}^2 \text{ s}^{-1}$  at delithiated states. Thus, in this work, a varying diffusion coefficient is considered to be incorporated into ROM-SPM such that the accuracy of the model can be increased while maintaining the low computational cost. The model is called single particle model with variable diffusivity (ROM-SPMVD) [86].

As the key parameter of the ROM-SPMVD, the value of the diffusion coefficient at each SOC should be known. Currently, the value of the diffusion coefficient has been attempted to measure at different SOCs and temperatures by employing several techniques [87] that include the incremental titration based galvanostatic intermittent titration technique (GITT) [84][88][91][92] and potentiostatic intermittent titration technique (PITT) [89][90], electroanalytical techniques

such as electrochemical impedance spectroscopy (EIS) [90][91] and cyclic voltammetry (CV) [93]. The GITT is the one that is widely used because of the possibility to determine the diffusion coefficient accurately at discrete SOC points. However, this method has often been applied to half cells, which requires specialized experimental instrumentations and testing conditions. Therefore, this technique is not applicable for measuring commercial cells made of several dozens of full cells. In addition, the diffusion coefficient measured from half cells might not be identical to the one needed for a model. Thus, a fast and efficient method that allows for determination of the diffusion coefficient as a function of SOC without fabricating a half cell, which can be directly used in the model is also desired.

In this section, the ROM-SPMVD is firstly constructed on the basis of ROM-SPM by using the polynomial approximation method for lithium ions concentration in electrodes, the residue grouping method for lithium ions concentration in electrolyte, and the analytical solution for the potential in electrolyte. Particularly, the equations derived for the lithium ion concentration in solid are numerically solved by the first order Runge–Kutta method. Then, the lithium ion diffusion coefficient–SOC relationship in cathode is predicted from the newly developed nondestructive method that is based on the ROM-SPM using gradient-descent algorithm, and the result is compared with that obtained from GITT given in references. Finally, the predicted diffusion coefficients using the proposed method is incorporated in the ROM-SPMVD that is validated against the experimental data at the discharge profiles and HPPC test at 25°C. In addition, the model is also validated at 45°C and 0°C with the predicted  $D_{s,p}(SOC)$  at each temperature to examine the validity in other temperatures. The accuracy of the terminal voltage response and computation time are compared with those of ROM-SPM.

## 5.2 Model development and simplification

Generally, a single cell of the pouch type lithium-ion polymer battery is made of microcells that are connected in parallel to increase capacity and power. The model for the cell is approximated by a micro cell under assumption that all of the microcells have the same characteristics. The microcell has a sandwich structure with three domains, a composite anode, a separator and a composite cathode between the two current collectors at the end of each electrodes. The electrochemical behavior of the microcell can be described by the principles of diffusion, mass transport, electrochemical kinetics, and Ohm's laws. The governing equations with boundary conditions are listed in Table 1.

The equations listed above include partial differential equations and nonlinear equations that can be simplified into linear ordinary differential equations by mathematical treatments, which results in a reduced order model (ROM). When the volume current density maintains uniformly distributed in anode and cathode, all of the particles can be assumed to be the same and can be replaced by a spherical particle, which is called ROM-SPM [94]. Figure 36 shows the schematic diagram of the ROM-SPM.

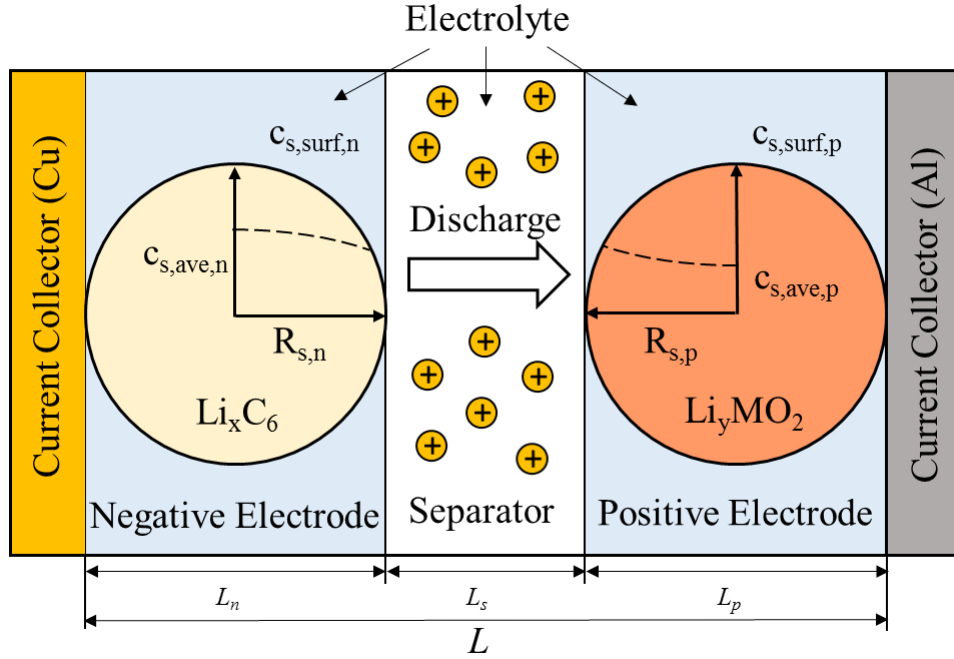


Figure 36. Schematic diagram of ROM-SPM.

The uniformed volume current density in solid phase and electrolyte is expressed as:

$$j^{Li} = \frac{I}{L \cdot A} \quad (48)$$

The terminal voltage of the cell is the difference between two solid potentials of two electrodes and an Ohmic voltage drop in current collectors:

$$V_{cell} = \phi_s(L) - \phi_s(0) - IR_c \quad (49)$$

The Fick's law for ion diffusion in solid phase is simplified using the polynomial approximation method [73]. The ion concentrations inside the solid particles are replaced using

averaged concentration,  $c_{s,ave}$ , averaged concentration flux,  $q_{ave}$  and surface concentration,  $c_{s,surf}$ , which results:

$$\begin{aligned}\frac{d}{dt}c_{s,ave} &= -\frac{3}{R_s Fa_s} j^{Li} \\ \frac{d}{dt}q_{ave} + \frac{30D_s}{R_s^2} q_{ave} + \frac{45}{2R_s^2 Fa_s} j^{Li} &= 0. \\ \frac{35}{R_s} c_{s,surf} - 8q_{ave} - \frac{35}{R_s} c_{s,ave} &= -\frac{j^{Li}}{D_s Fa_s}\end{aligned}\quad (50)$$

If the diffusion coefficient in solid phase depends upon SOC, Eq. (50) can be modified as:

$$\begin{aligned}\frac{d}{dt}c_{s,ave} &= -\frac{3}{R_s Fa_s} j^{Li} \\ \frac{d}{dt}q_{ave} + \frac{30D_s(SOC)}{R_s^2} q_{ave} + \frac{45}{2R_s^2 Fa_s} j^{Li} &= 0. \\ \frac{35}{R_s} c_{s,surf} - 8q_{ave} - \frac{35}{R_s} c_{s,ave} &= -\frac{j^{Li}}{D_s(SOC) Fa_s}\end{aligned}\quad (51)$$

In fact, SOC is defined as a ratio of the releasable charge capacity to the maximum charge capacity ( $Q_{max}$ ) that can be expressed using the averaged lithium ions concentration within the electrode particles:

$$SOC = SOC_0 - \frac{\int_0^t I(\tau) d\tau}{Q_{max}} \times 100\% = \frac{\theta - \theta_{0\%}}{\theta_{100\%} - \theta_{0\%}} \times 100\% \quad (52)$$

, where  $SOC_0$  denotes the initial SOC,  $\theta = c_{s,ave}/c_{s,max}$ , and the subscripts of 100% or 0% denote the states where battery is fully charged (100% SOC) or discharged (0% SOC).

When SOC in Eq. (51) is substituted by Eq. (52), the second equation in Eq. (51) becomes a first order ODE with a variable coefficient and can be numerically solved using the first order Runge-Kutta method. The equation is iteratively solved by:

$$k_i = -\frac{30D_s \left( \frac{\int_0^t I(\tau) d\tau}{Q_{\max}} \right)}{R_s^2} q_{ave}(t_i) - \frac{45}{2R_s^2 Fa_s} j^{Li}(t_i) \quad (53)$$

$$q_{ave}(t_{i+1}) = q_{ave}(t_i) + k_i \Delta t$$

, where  $\Delta t$  is time step, and  $i=1,2,\dots,N$  is the iteration index.

The PDE of lithium ion concentration in the electrolyte phase is approximated using the residue grouping method that groups the states according to similarity of eigenvalues [75]. The detailed description can be found in a previously published paper [95].

The equation for Ohm's law in electrolyte is a PDE with a nonlinear term that is linearized as follows:

$$\frac{\partial}{\partial x} \left( \kappa^{eff} \frac{\partial \phi_e}{\partial x} \right) + \frac{\partial}{\partial x} \left( \frac{\kappa_D^{eff}}{c_{e,0}} \frac{\partial c_e}{\partial x} \right) + j^{Li} = 0. \quad (54)$$

By integrating the linearized equation twice, an analytical expression for the potential difference in electrolyte phase can be obtained:

$$\phi_e(L) - \phi_e(0) = -\frac{I}{2A} \left( \frac{L_n}{\kappa_n^{eff}} + \frac{2L_s}{\kappa_s^{eff}} + \frac{L_p}{\kappa_p^{eff}} \right) + \frac{2RT}{c_{e,0}} \left( \frac{1-t_+^0}{F} \right) (c_e(L,t) - c_e(0,t)). \quad (55)$$

The electrochemical kinetics are described by the Butler-Volmer equation that is a function of concentration, potential and electrochemical reaction rate, where the anodic and cathodic charge transfer coefficients are set to equally 0.5. Then, the equation is used to get the overpotential as follows:

$$j^{Li} = a_s i_0 \left\{ \exp \left[ \frac{0.5F}{RT} \eta \right] - \exp \left[ -\frac{0.5F}{RT} \eta \right] \right\} = 2a_s i_0 \sinh \left( \frac{0.5F}{RT} \eta \right), \quad (56)$$

$$\eta = \frac{RT}{0.5F} \sinh^{-1} \left( \frac{j^{Li}}{2a_s i_0} \right). \quad (57)$$

The terminal voltage of the cell results in as:

$$V_{cell} = (U_p - U_n) + [\phi_e(L) - \phi_e(0)] + (\eta_p - \eta_n) - IR_c. \quad (58)$$

Here,  $U_n$  and  $U_p$  denote the equilibrium potential of the solid in negative (anode) and positive (cathode), and are expressed as a function of stoichiometric numbers and the associated surface ion concentration:

$$U_p = U_p(x), \text{ and } U_n = U_n(y)$$

, where  $x = \frac{c_{s,surf}^p}{c_{s,max}^p}$  and  $y = \frac{c_{s,surf}^n}{c_{s,max}^n}$ .

Finally, the model was implemented and solved with the custom-made code developed in MATLAB environment.

### 5.3 Determination of diffusion coefficient in solid phase of cathode

Determination of the diffusion coefficient in solid phase of cathode of a cell is the most crucial task and very challenging because only the terminal voltage of a cell can be measured. Therefore, a model based diffusion coefficient determination algorithm is proposed under two assumptions: (1) the overpotential caused by the diffusion in cathode particles is predominant, and is separable from the terminal voltage; and (2) the diffusion coefficient of cathode is a sensitive parameter to the terminal voltage. These assumptions are examined by the overpotential analysis and the parameter sensitivity analysis as follows.

#### 5.3.1 Overpotential and parameter sensitivity analysis

##### 5.3.1.1 Overpotential analysis

The relationship between the diffusion and overpotential is analyzed using the experimentally validated ROM, which parameters are listed in Appendix A. All the parameters including the diffusion coefficients in active materials are set to be constant.

Simulation results of the terminal voltage during discharge with 0.4C (23.2A) from 100% SOC and the open circuit voltage (OCV) are plotted in Figure 37 (a). The OCV (indicated as black line in Figure 37 (a)) is the potential differences between cathode and anode at equilibrium states, where no concentration gradient exists in both particles and electrodes, and expressed as:

$$E_{cell} = E_p(\bar{x}) - E_n(\bar{y}), \quad (59)$$

where  $\bar{x} = \frac{c_{s,ave}^p}{c_{s,max}^p}$  and  $\bar{y} = \frac{c_{s,ave}^n}{c_{s,max}^n}$ .

The total cell overpotential is the difference between the terminal voltage and the OCV:

$$\eta_{cell} = V_{cell} - E_{cell}. \quad (60)$$

Then, the total overpotential can be decomposed into those for electrodes, electrolyte and current collectors:

$$\begin{aligned} E_{cell} - V_{cell} &= (E_p - E_n) - (U_p - U_n) - [\phi_e(L) - \phi_e(0)] - (\eta_p - \eta_n) + IR_c \\ &= (E_p - U_p) \quad \text{(a) solid concentration overpotential in positive electrode} \\ &\quad - (E_n - U_n) \quad \text{(b) solid concentration overpotential in negative electrode} \\ &\quad - [\phi_e(L) - \phi_e(0)] \quad \text{(c) electrolyte Ohmic and concentration overpotential} \\ &\quad - (\eta_p - \eta_n) \quad \text{(d) difference between activation overpotential of both electrodes} \\ &\quad + IR_c \quad \text{(e) Ohmic voltage drop at current collectors} \end{aligned}$$

Contribution of individual overpotential to the total cell overpotential is depicted in Figure 37 (a). The overpotential caused by solid phase concentration (a) and resistance of current collectors (e) are the dominant parts, and around 0.024V and 0.020V that make a percentage of 91.5% of the total overpotential, while (b), (c) and (e) together contribute with a small portion. These results are similar to those by ROM-P2D [96].

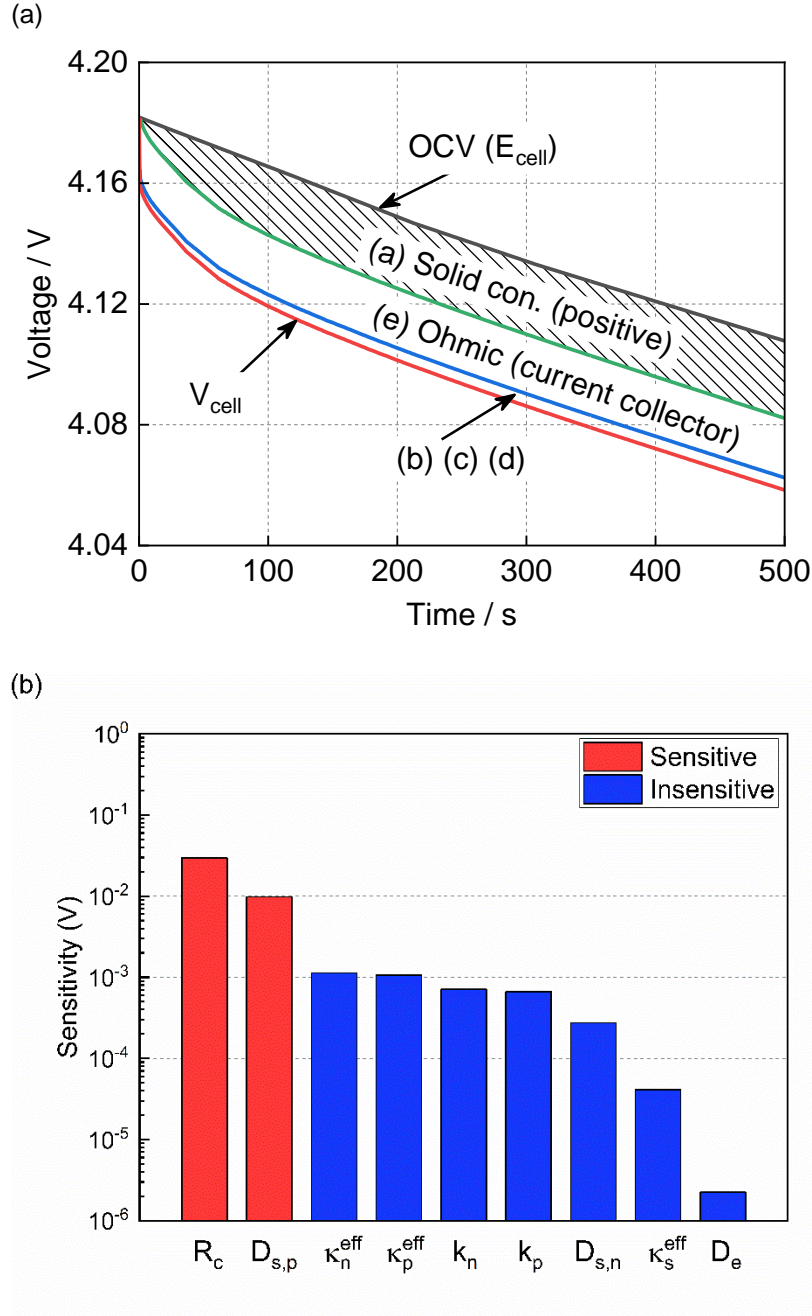


Figure 37. (a) Overpotential analysis and (b) parameter sensitivity analysis result of ROM-SPM.

The first one (a) is the potential difference between the cathode particle at equilibrium state,  $E_p$  and transient state  $U_p$ . Since  $E_p$  and  $U_p$  are a function of  $C_{s,ave}^p$  and  $C_{s,surf}^p$ , the overpotential is directly affected by variation of the lithium ion concentration within the particles in the

composite cathode. In fact, the variation is induced by the diffusion of ions in the solid in cathode governed by the Fick's law.

The second one (e) is the pure Ohmic voltage drop caused by the resistance of the current collector. The voltage drop increases linearly as the current increases, which is governed by Ohm's law. Since the resistance is easily calculated, the overpotential by diffusion can be estimated and separated.

### 5.3.1.2 Sensitivity analysis of parameters

In order to find out the sensitivity of parameters on the terminal voltages, following analysis of the key parameters in ROM-SPM was performed. The sensitivity variables can be obtained by the partial derivative of the terminal voltage over the parameters:

$$S_i = \frac{\partial V_{cell}}{\partial X_i} \quad (61)$$

, where  $X_i$  and  $S_i$  represent the parameters and the corresponding sensitivity variables.

From the expression for the terminal voltage given in Eq. (58), the parameters that have considered for the sensitivity analysis are: (1) diffusion coefficient in solid phase in anode ( $D_{s,n}$ ) and cathode ( $D_{s,p}$ ), (2) diffusion coefficient in electrolyte ( $D_e$ ), (3) effective electrolyte ionic conductivity in anode ( $\kappa^{eff}_n$ ), separator ( $\kappa^{eff}_s$ ) and cathode ( $\kappa^{eff}_p$ ), (4) kinetic rate constant in anode ( $k_n$ ) and cathode ( $k_p$ ), as well as (5) Ohmic resistance ( $R_c$ ).

The mathematical expression for the sensitivity variables of the parameters are listed in Table 8.

Table 8. Mathematical expression of sensitivity variables of the parameters for ROM-SPM

Parameter	Sensitivity variables
$D_s$	$\frac{\partial V_{cell}}{\partial D_s} = \pm \frac{\partial U}{\partial c_{s,surf}} \left[ \frac{1080}{7Fa_s LA} t \exp\left(-\frac{30D_s}{R_s^2} t\right) + \frac{R_s}{35Fa_s D_s^2 LA} \right] I(t)$
$D_e$	$\frac{\partial V_{cell}}{\partial D_e} = \frac{\partial}{\partial D_e} [\phi_e(L) - \phi_e(0)] = \frac{2RT}{c_{e,0}} \left( \frac{1-t_+^0}{F} \right) \frac{\partial}{\partial D_e} (c_e(L,t) - c_e(0,t))$ $\frac{\partial}{\partial D_e} c_e(0,t) = \left( (1 - \exp(-t/\tau_n)) \frac{\partial}{\partial D_e} P_2 - P_2 \exp(-t/\tau_n) \frac{t}{\tau_n^2} \frac{\partial}{\partial D_e} \tau_n \right) \frac{I(t)}{A}$ $\frac{\partial}{\partial D_e} c_e(L,t) = \left( (1 - \exp(-t/\tau_p)) \frac{\partial}{\partial D_e} P_6 - P_6 \exp(-t/\tau_p) \frac{t}{\tau_n^2} \frac{\partial}{\partial D_e} \tau_p \right) \frac{I(t)}{A}$
$\kappa_i^{eff}$	$\frac{\partial V_{cell}}{\partial \kappa_i^{eff}} = -\frac{1}{2A} \frac{\partial}{\partial \kappa_i^{eff}} \left( \frac{L_n}{\kappa_n^{eff}} + \frac{2L_s}{\kappa_s^{eff}} + \frac{L_p}{\kappa_p^{eff}} \right) I(t)$ $= \begin{cases} \frac{L_n}{2A} \frac{1}{(\kappa_n^{eff})^2} I(t), i = n \\ \frac{L_s}{A} \frac{1}{(\kappa_s^{eff})^2} I(t), i = s \\ \frac{L_p}{2A} \frac{1}{(\kappa_p^{eff})^2} I(t), i = p \end{cases}$
$k$	$\frac{\partial V_{cell}}{\partial k} = -\frac{RT}{Fi_0} \frac{1}{\sqrt{\left(\frac{I(t)}{2i_0}\right)^2 + (a_s LA)^2}} \frac{I(t)}{k}$
$R_c$	$\frac{\partial V_{cell}}{\partial R_c} = -I(t)$

For comparisons, all the sensitivity variables are normalized by [97]:

$$\bar{S}_i = \frac{\partial V_{cell}}{\partial X_i} X_i. \quad (62)$$

The normalized sensitivities of each parameter are analyzed by applying a set of constant current discharge profiles at 25°C. The discharging profile is composed of 1C, 0.8C, 0.6C, 0.4C and 0.2C, from 100% SOC until the terminal voltage reaches the cut off voltage. The normalized sensitivities for each parameter are calculated at five input current profiles, averaged and plotted in Figure 37 (b). Results show that the  $R_c$  and  $D_{s,p}$  are the most sensitive parameters that affect the terminal voltage of the model, which become strongly identifiable compared with others.

### 5.3.2 ROM-SPM based diffusion coefficient determination algorithm

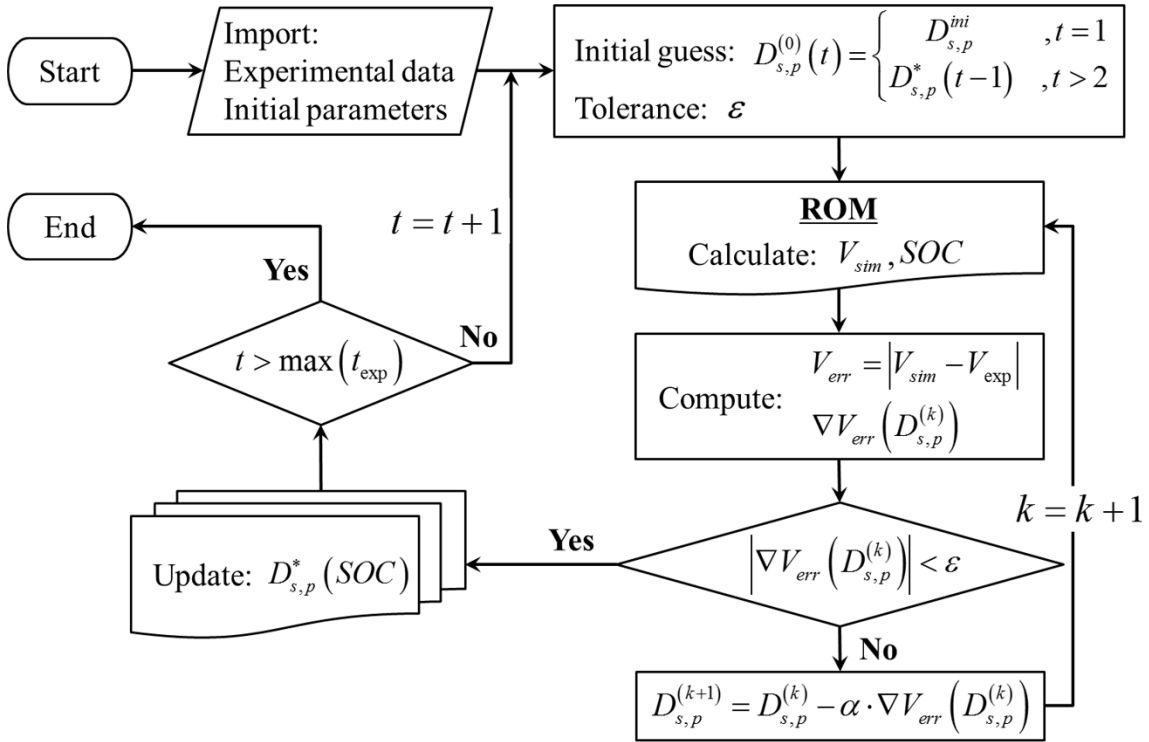
One of the most sensitive parameter for the proposed ROM-SPMVD is the diffusion coefficient. Its determination is challenging because most of the measurements for the diffusion coefficient can only be carried out with a half cell, which is not applicable for commercial cells that consist of stacked or folded microcells. In addition, the measured value is usually inappropriate for the simplified diffusion equation used in ROM. Therefore, we propose a new method for determination of the diffusion coefficient based on a gradient descent (GD) method (loop) [98], where an optimal value can be found by minimizing the voltage error between the simulation and the experiment. The simulation is performed using ROM-SPM, where the input is the current and the output is voltage during discharge from 100% SOC to 0%. Initial values of the parameters used for the simulation are listed in Appendix A. The selected current was 0.8C which corresponds to 46.4A, and should minimize degradation. An initial value of  $D_{s,p}$  is set as  $4.0 \times 10^{-10} \text{ cm}^2 \text{ s}^{-1}$  at 25°C.

Figure 38 (a) shows a flowchart of the method for determination of diffusion coefficient, which is carried out using an iterative GD optimization loop. In the GD loop, a cost function is formulated as an absolute error between the simulated and experimentally measured terminal voltage. Then, the cost function is minimized by calculating the gradient of the cost function with regard to the diffusion coefficient ( $\nabla V_{err}$ ) and updating the value of  $D_{s,p}$  with a specified learning rate ( $\alpha$ ). This GD method requires a minimum error bound that is called the termination tolerance,  $\varepsilon$ , which represents the maximum admissible discrepancy between the predicted and measured voltage. In fact, the terminal voltage decreases rapidly at low SOC. As a result, any small change of the diffusion coefficient largely affects the terminal voltage, which can lead to a convergence of the algorithm. Consequently, the determination tolerance should be increased, which is approximated with Eq. (63) for the given OCV-SOC curve. The value 0.001mV indicates the tolerance for the SOC range of 100%~20%, while the tangential function represents an increase of the error bound when SOC is smaller than 20%, which is plotted in Figure 38 (b). At each SOC point, the GD loop is repeated until the condition of the termination tolerance is satisfied.

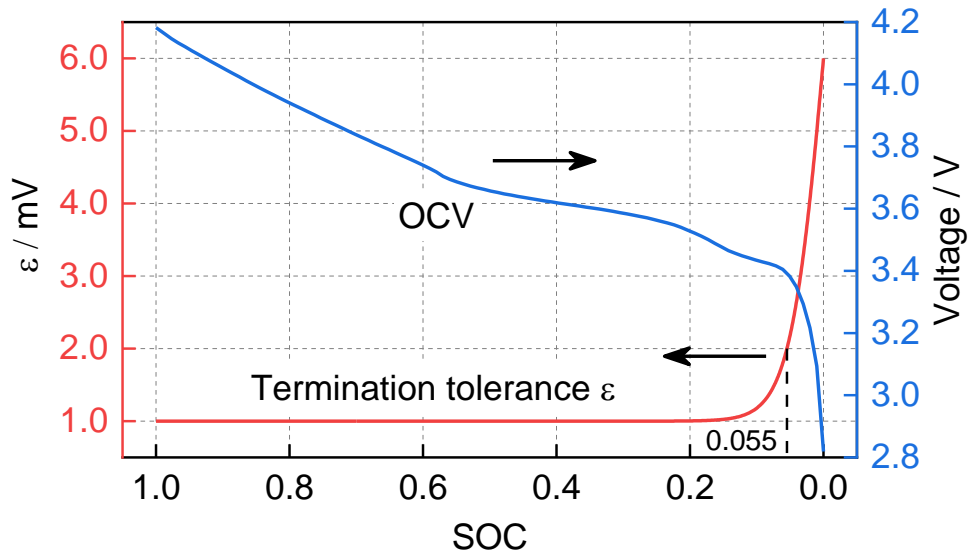
$$\varepsilon = 0.005 \times [1 + \tan(-20 \times SOC)] + 0.001 \text{ [mV]} \quad (63)$$

At the first, the  $D_{s,p}^*$  is taken as the predicted diffusion coefficient of cathode materials at certain SOC, and be used as the initial guess for the next time step. The process of algorithm will stop when all the experimental data are used for determination, and out put the  $D_{s,p}(SOC)$  relationship at the end of the process.

(a)



(b)



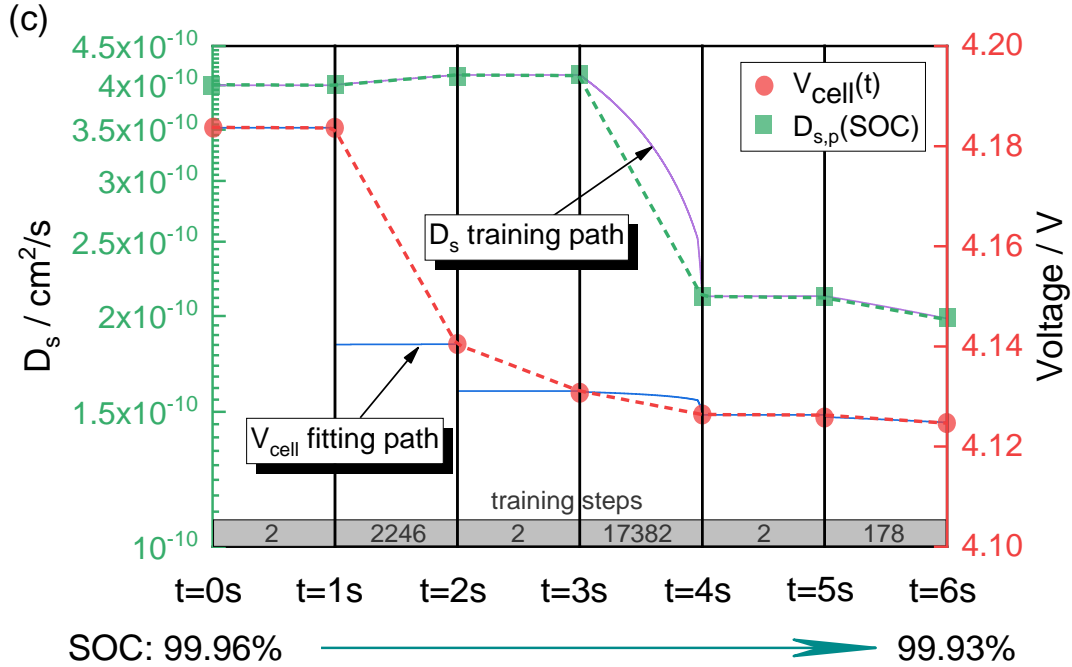


Figure 38. (a) Flowchart of diffusion coefficient determination procedure. (b) Termination tolerance versus SOC, combined with an OCV-SOC curve as a reference. (c) Training and fitting path of  $D_{s,p}$  and  $V_{cell}$  to show the convergence of the algorithm

## 5.4 Prediction of the $D_{s,p}$ and model validation

### 5.4.1 Experiments and $D_{s,p}$ prediction

For experiments, a large format pouch type NMC622/Graphite lithium-ion energy cell is used, which is the same as the one used in Section 3.2.2.1.

Cells are placed in the multifunctional calorimeter and in a thermal chamber with a preset constant temperature, and the terminal current and voltage, and surface temperatures are measured. During the operation, the cells' temperature is actively controlled by the thermostat system with a maximum temperature rise of 0.25°C for all the experiments, such that the effects of the temperature on the discharging characteristics are limited.

During the tests, the  $D_{s,p}(SOC)$  of the cathode NMC materials is estimated using the aforementioned method. Firstly, the cell was fully charged at 25°C and rested for one hour and then discharged with a 0.8C (46.4A) constant current until the voltage reaches 2.5V. The current and voltage are processed using the method outlined in section 3.2. The initial  $D_{s,p}$  and learning rate  $\alpha$  are listed in Table 9.

Table 9. Initial  $D_{s,p}$  and learning rate at 0°C, 25°C and 45°C

Temperature/°C	Initial $D_{s,p} / \text{cm}^2 \text{s}^{-1}$	Learning rate $\alpha$
0	$3.0 \times 10^{-11}$	$1.0 \times 10^{-22}$
25	$4.0 \times 10^{-10}$	$1.0 \times 10^{-21}$
45	$9.0 \times 10^{-10}$	$5.0 \times 10^{-21}$

Figure 38 (c) shows the detailed training and fitting path of  $D_{s,p}$  and  $V_{cell}$  with time steps. The training steps are included at the bottom of the figure. At the beginning of each time step, an initial value of  $D_{s,p}$  is assumed, and the corresponding  $V_{cell}$  is calculated. Then the  $D_{s,p}$  converges to the optimal (green circle in ) following the training path (solid purple line) using the gradient descent iteration, while the  $V_{cell}$  approaches to the experimental measured value (red circle) along with the fitting path (solid blue line). Then, the  $D_{s,p}(SOC)$  relationship curve at 25°C is obtained and plotted in Figure 39 (a).

Similarly, the  $D_{s,p}(SOC)$  is estimated at 45°C and 0°C. For simplicity, we only consider the temperature effect on  $D_{s,p}$ , and neglecting its effect on the current collector resistance and other parameters. The initial value of  $D_{s,p}$  at 45°C and 0°C was set to be greater and smaller than that at 25°C respectively, as listed in Table 9, which could be verified from the tendency of the experimental measured diffusion coefficient [81]. With this approach, the convergence of the

method is accelerated. In addition, the learning rates were also adjusted to improve the convergence speed at each temperature. The predicted  $D_{s,p}(SOC)$  relationship at 0°C and 45°C are also depicted in Figure 39 (a).

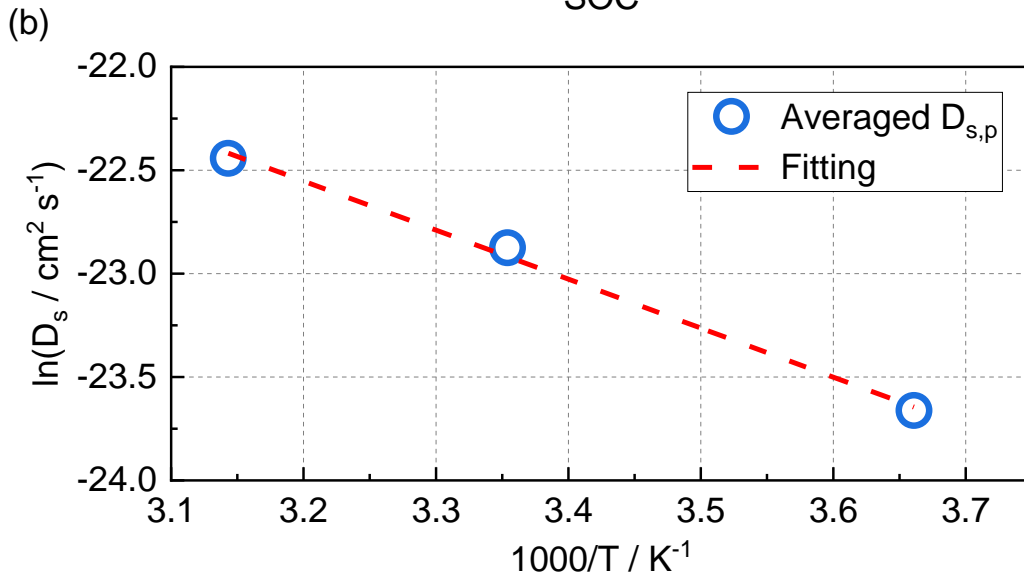
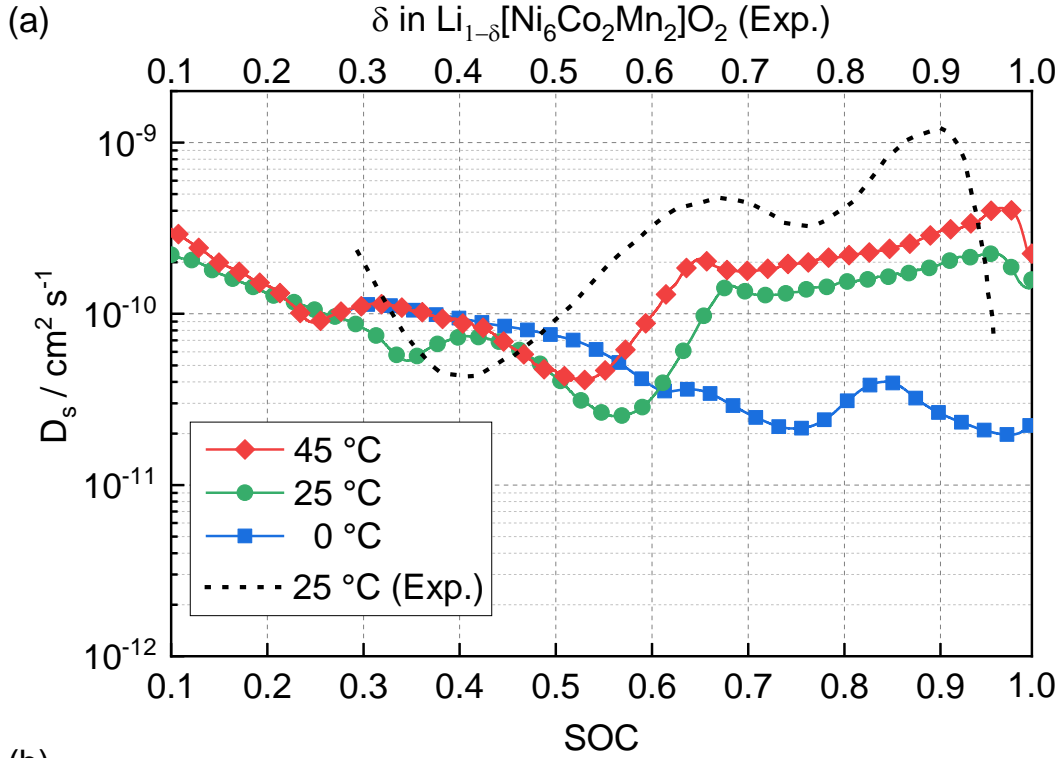


Figure 39. (a) Predicted  $D_{s,p}(SOC)$  at 0°C, 25°C and 45°C. The black dash line represents the experimental measured diffusion coefficient using GITT method at 25°C taken from Ref. [46], (b) Logarithmic scale of averaged diffusion coefficient versus inverse temperature at 0, 25 and 45°C.

As shown in Figure 39 (a), the values of predicted diffusion coefficient of NMC622 cathode at 25°C ranges between  $2.53 \times 10^{-11} \text{ cm}^2 \text{ s}^{-1}$  and  $2.26 \times 10^{-10} \text{ cm}^2 \text{ s}^{-1}$ . When SOC increases from 0% to 50% SOC, the  $D_{s,p}$  values tend to decrease from  $2.21 \times 10^{-10} \text{ cm}^2 \text{ s}^{-1}$  to  $4.23 \times 10^{-11} \text{ cm}^2 \text{ s}^{-1}$ , and then reach to a peak value of  $1.46 \times 10^{-10} \text{ cm}^2 \text{ s}^{-1}$  at around 68% SOC. Then, the  $D_{s,p}$  gradually increases from  $1.29 \times 10^{-10} \text{ cm}^2 \text{ s}^{-1}$  to  $2.26 \times 10^{-10} \text{ cm}^2 \text{ s}^{-1}$  as the SOC increases, and then slightly decreases at 100% SOC.

The result of the predicted  $D_{s,p}(SOC)$  was compared with a few experimentally measured ones of the same materials, as listed in Table 10. These experiments were performed using the cells that consist of NMC622 ( $\text{Li}[\text{Ni}_{0.6}\text{Mn}_{0.2}\text{Co}_{0.2}]\text{O}_2$ ) and metal lithium. The diffusion coefficients of lithium ion were measured by galvanostatic intermittent titration technique (GITT) or potentiostatic intermittent titration technique (PITT) method. The experimental measured lithium ion diffusion coefficient at 25°C in those references were in the range of  $1 \times 10^{-11} \sim 1 \times 10^{-9} \text{ cm}^2 \text{ s}^{-1}$ , which is consistent with the range of the predicted values of  $D_{s,p}$  using the proposed method. In addition, the shape of the predicted  $D_{s,p}(SOC)$  curve at 25°C shows similar to that obtained using GITT method [46] with respect to a decrease at low SOC range, two peaks at 68% SOC and 95% SOC and the overall tendency.

Table 10. Measured lithium ion diffusion coefficient of NMC622 materials from literatures.

Ref.	Cell	Temperature / °C	$D_s$ range / $\text{cm}^2 \text{ s}^{-1}$	Measurement method
[84]	NMC622/Li	25	$1 \times 10^{-11} \sim 9 \times 10^{-11}$	GITT
[46]	NMC622/Li	25	$4 \times 10^{-11} \sim 1 \times 10^{-9}$	GITT

[101]	NMC622/Li	25	$1 \times 10^{-10} \sim 1 \times 10^{-9}$	PITT
[81]	NMC622/Li	25	$7 \times 10^{-11} \sim 8 \times 10^{-11}$	GITT
		50	$9 \times 10^{-11} \sim 1 \times 10^{-10}$	
		0	$3 \times 10^{-11} \sim 6 \times 10^{-11}$	

Moreover, the predicted lithium ion diffusion coefficient of NMC622 is dependent upon the temperature, which can be described using Arrhenius equation:

$$\ln(D_{s,p}) = \ln(D_{0,p}) - \frac{E_a}{RT} \quad (64)$$

, where  $E_a$  is the activation energy for lithium ion diffusion, and  $D_{0,p}$  is the diffusion coefficient at infinite temperature.

The logarithmic scale of the averaged diffusion coefficient versus inverse temperature at 0, 25 and 45°C is plotted in Figure 39 (b), where, the dashed line indicates the fitting using the Arrhenius equation. The determined activation energy for lithium ion diffusion is 19.71 kJ mol<sup>-1</sup>, which is comparable to the range from 4.82 kJ mol<sup>-1</sup> to 45.83 kJ mol<sup>-1</sup> that is typically seen for NMC materials [81], [99], [100].

#### 5.4.2 ROM-SPMVD validation

The predicted  $D_{s,p}(SOC)$  is incorporated into the ROM-SPMVD and analyzed with experimental data. The fully charged cell was discharged with different C rates, 1C, 0.6C and 0.2C to the cutoff voltage of 2.5V at 25°C. Experimental and simulated terminal voltage are plotted in Figure 40, where the ROM-SPM and ROM-SPMVD are compared. At low C rate (0.2C), the

effects of dependence of the diffusion coefficient on the discharge characteristic are minimum, so that the terminal voltage matches well with the experimental data. When the applied current increases, the simulated voltage curve from ROM-SPM gets deviated from the experimental data. The RMSEs of the voltage at 0.6C and 1C are 0.049V and 0.117V, respectively that were reduced to 0.032V and 0.024V by ROM-SPMVD. ROM-SPMVD performs well in high currents.

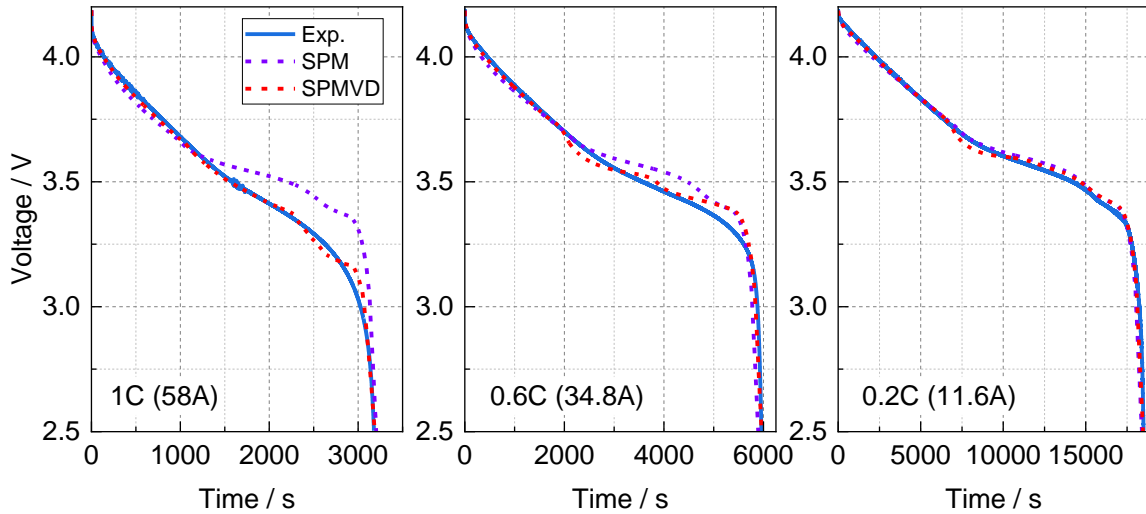


Figure 40. Validation result: 1C, 0.6C and 0.2C CC discharge at 25°C.

RMSE of the voltage by ROM-SPM and ROM-SPMVD are plotted in Figure 41 (a) and the computational time of the ROM-SPM and ROM-SPMVD is plotted in Figure 41 (b), where the models are coded using MATLAB script and simulated on a PC that has a 3.4 GHz Intel Quad Core processor with 16 GB RAM.

It took 27.96 seconds for ROM-SPMVD to calculate the discharging characteristic with 0.2C, which is around 2.4 times than the ROM-SPM. This extended calculation time is mainly caused by the embedded interpolation-based diffusion coefficient update script in ROM-SPMVD. However, it is still very efficient compared with ROM-P2D that take 5 time more and the FOM

that takes 50 times more [77], that seems to be acceptable for real time applications. In addition, the ROM-SPMVD takes advantage of the simplified structure of ROM-SPM that replaces the high order matrix calculation with analytical equations for solid phase concentration and electrolyte potential calculation is friendly for implementation of the ROM into the BMS.

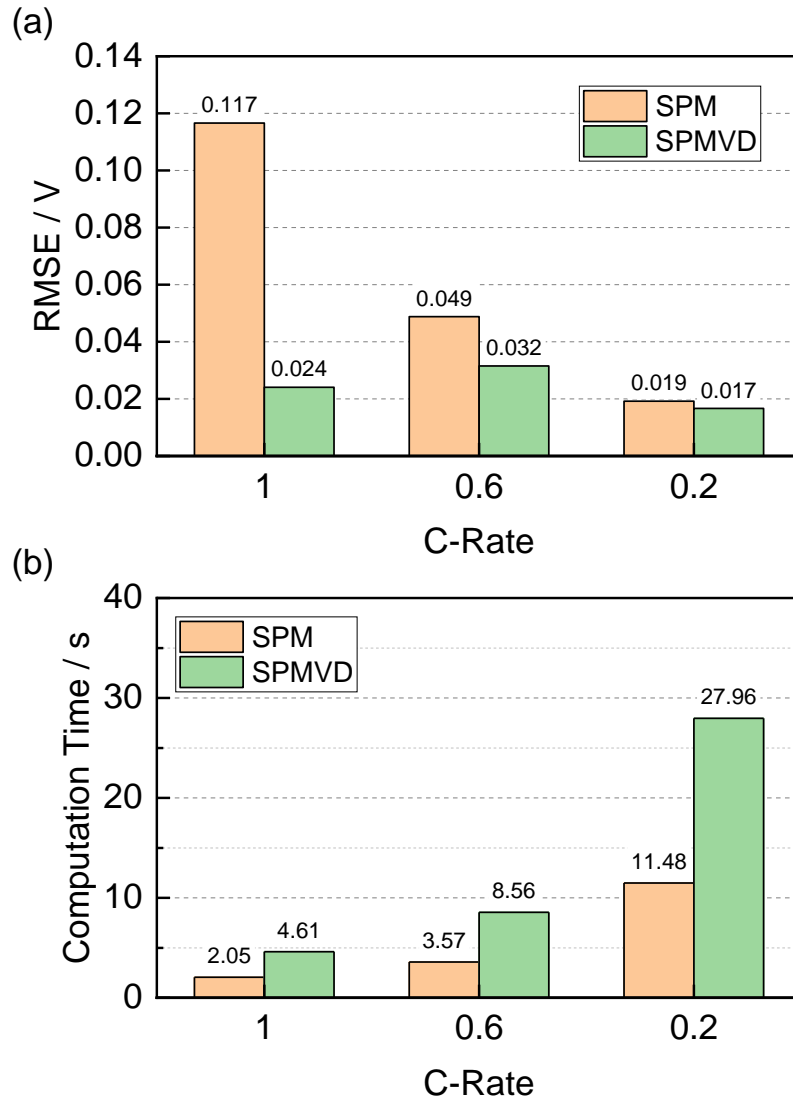


Figure 41. Comparison of (a) RMSE and (b) computation time between ROM-SPM and ROM-SPMVD at 1C, 0.6C and 0.2C CC discharge at 25°C.

In order to verify the long-term performance and the performance under dynamic operations, the HPPC tests at 25°C are carried out. Figure 42 (a) shows the input current profile of the HPPC test. The HPPC consists of a sequence of a 30-second discharge pulse at  $I_{max}$  (112A) that is the manufacture's absolute maximum allowable pulse discharge current for 30 seconds and a 40-second rest. At first, the cell was fully charged at the rate of C/3 (19.3A) and rested for 1 hour. After the resting period, the cell was subject to a 10-second regen pulse at  $0.75 I_{max}$  (84A). Between each pair of the discharge and regen pulses, the cell was discharged to 10% of capacity at C/3 (19.3A). This sequence was repeated until a cutoff voltage reaches 2.5V.

Figure 42 (b) compares the terminal voltage obtained from the simulation and experiment, where both curves match well at both charge, discharge and resting period over full range of SOC. The RMSE is reduced to 0.012V.

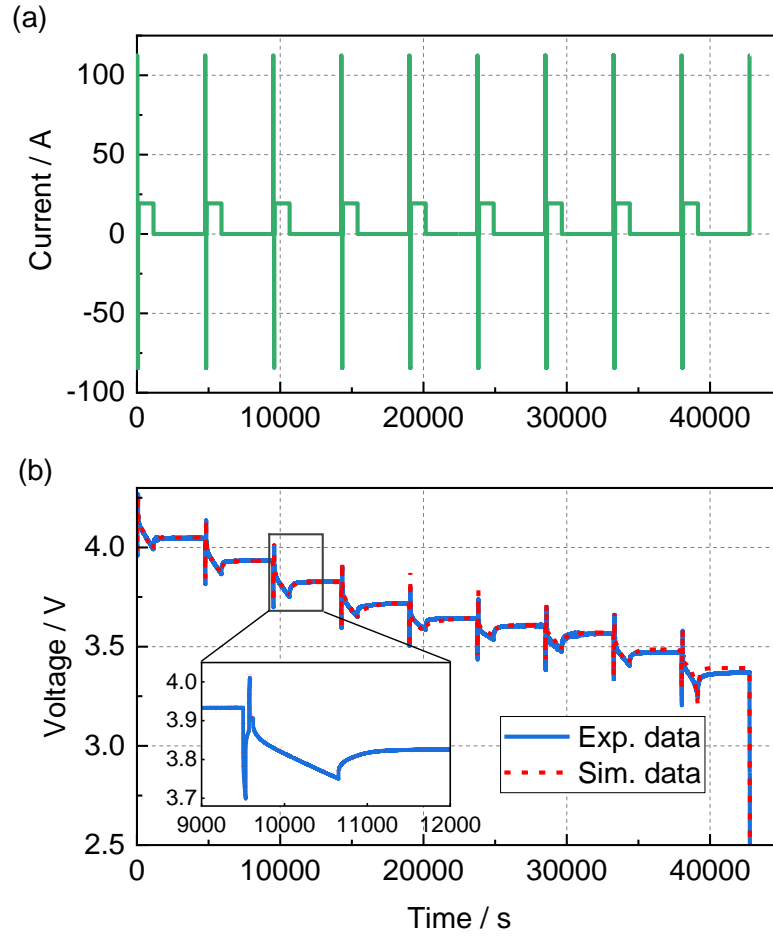


Figure 42. Validation result: (a) HPPC current; (b) HPPC voltage curves.

Likewise, the response of the ROM-SPMVD is further investigated at two other different ambient temperature of  $45^{\circ}\text{C}$  and  $0^{\circ}\text{C}$ , where the  $D_{s,p}$  (SOC) at  $45^{\circ}\text{C}$  and  $0^{\circ}\text{C}$ , as shown in Figure 39 (a) was incorporated into the model. The results were plotted in Figure 43, where the performance of ROM-SPM and ROM-SPMVD are compared to each other.

For the ROM-SPM, the value of the diffusion coefficient at  $45^{\circ}\text{C}$  and  $0^{\circ}\text{C}$  was so chosen as to best fit to the experimental curve, which results in  $4.5 \times 10^{-10} \text{ cm}^2 \text{ s}^{-1}$  and  $5.2 \times 10^{-11} \text{ cm}^2 \text{ s}^{-1}$ . At  $45^{\circ}\text{C}$ , the ROM-SPM tends to deviate from the experimental data under 1C discharge, while ROM-

SPMVD keeps following the voltage drops. The RMSE of the voltage by ROM-SPMVD and ROM-SPM is 0.018V and 0.074V, respectively.

At 0°C, a similar tendency has been observed. The discrepancy of the ROM-SPM becomes larger, while ROM-SPMVD follows the voltage fairly well. The RMSE of voltage by ROM-SPM and ROM-SPMVD were 0.143V and 0.049V, respectively.

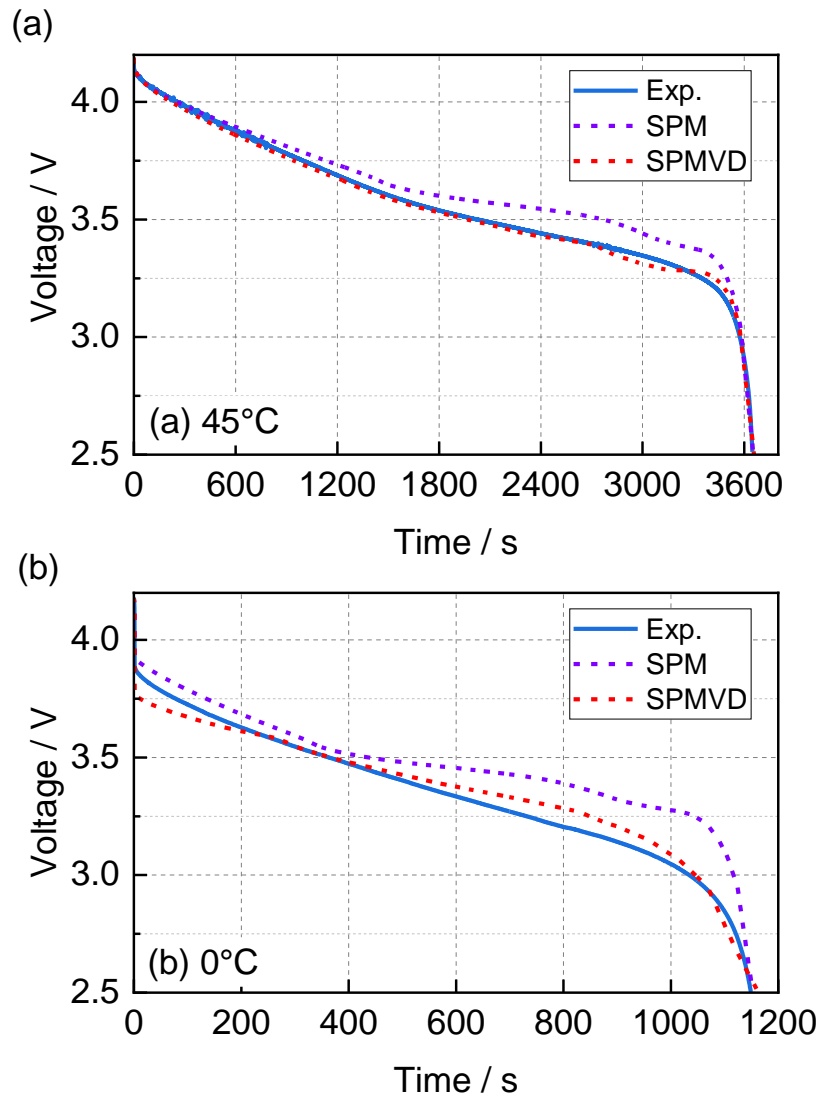


Figure 43. Validation result: 1C CC discharge at (a) 45°C and (b) 0°C.

## 5.5 Summary

ROM-SPM of lithium-ion batteries have advantages over other models because of short calculation time and the associated potentials in real time applications. However, the inaccuracy of the terminal voltage predicted by the ROM-SPM, especially at high C rates, limits wide applications. Therefore, a reduced order electrochemical model considering variable diffusion coefficient of lithium ions in solid is proposed and developed based on ROM-SPM scheme in order to improve the accuracy. Experimental validation has revealed that by considering of variable diffusion coefficient in solid phase in cathode, the voltage error of ROM-SPMVD can be reduced up to 79% compared with that of ROM-SPM.

Here is a summary of the major outcomes:

- A control oriented ROM-SPMVD of lithium-ion battery is developed that minimizes terminal voltage errors at high currents.
- Sensitivity analysis of the model parameters leads to a conclusion that the diffusion coefficient of lithium ions in solid of cathode is one of the most sensitive parameters.
- A nondestructive ROM based method for determination of the  $D_{s,p}$  as a function of SOC and temperature is proposed.
- ROM-SPMVD is validated against experimental data of a pouch type lithium-ion energy cell at different current profiles and different temperatures.

## Chapter 6. Conclusion

### 6.1 Conclusion

This dissertation comprehensively studied and analyzed the thermal behavior of large format pouch type lithium-ion batteries by experimental characterization and theoretical modeling. In this work, we:

- Developed a low-cost multifunctional calorimeter as hardware and associated software that enables the accurate and dynamic measurement of HGR with the maximum measurement error of  $0.67W$  and the response time of less than 10s. The measured results reveal that the high C-rates and low temperature affects the irreversible heat generation significantly, while the high temperatures mainly affect the reversible heat generation. In addition, the percentage of heat-induced energy loss,  $p_{heat}$  increases at high C-rates and low temperatures, indicating that more energy is dissipated.
- Proposed several novel experimental techniques that facilitate the fast and accurate characterization of the two heat source terms, which include
  - 1) Accelerated equilibration method: The method is proposed by applying an optimal control theory along with the electrochemical model. The resulting current profile significantly reduces the settling time needed for a battery cell to reach an equilibrium state when SOC is changed from one to a target value. The proposed profile at a constant temperature of  $25^{\circ}C$  reduces up to 55.8% and 58.3% testing time compared with that by the current pulse-resting method dependent upon  $\pm 1mV$  and  $\pm 0.5mV$  OCV error bounds.

- 2) Hybridized time-frequency domain analysis (HTFDA) method: The method works by applying two following sequential steps: time-domain background voltage offset correction and frequency-domain entropy coefficient determination. The measurement time of the HTFDA is drastically reduced to around 1/10 of that of the conventional potentiometric method, while maintaining the accuracy.
  - 3) Improved frequency-domain calorimetric method: The method characterizes the heat source terms by applying a sinusoidal current excitation and analyze the heat generation profiles in the frequency domain. It provides a fast and accurate tool for determination of entropy coefficient and internal resistance, which saves 92% of testing time compared with the conventional methods.
  - 4) Simultaneous and continuous characterization method: The method is developed based on the time-frequency domain analysis by wavelet transform technique. A sinusoidal AC-current superimposed by a small DC current is applied to the cell and the heat generation as a response is measured by the calorimeter. The measured time-series heat generation rate profile is processed by the continuous wavelet transform, and the entropy coefficient and internal resistance as a continuous function of SOC are obtained. The testing time by the proposed method saves around 95% of that by the conventional approaches.
- Develop a physics based electrochemical-thermal life model for the analysis of the heat generation mechanism within lithium-ion cells.

- Further proposed an improved battery electrochemical model by considering a SOC-dependent diffusion coefficient lithium ions in cathode, which has been validated to show a drastic increase of the accuracy in predicting the terminal voltage, while maintaining low computational time.

## 6.2 Future work

### 6.2.1 Experimental measurement and modeling of 2D heat generation behavior (2D-HGR)

In this work, we experimentally measured and simulated the lumped heat generation behavior of the cell. In real applications, the local heat generation rate of the cell varies at different locations, which may result in the generation of hot spots. The 2D-HGR distribution depends on the dimension, tab locations, electrode and electrolyte materials, nominal capacity, operational temperature and applied current. Accurate characterization of the 2D-HGR will facilitate the cost effective and efficient design of cooling systems in electric vehicle in order to ensure safe operation. In order to study this issue, a calorimeter that enables the measurement of 2D-HGR is required. In addition, an accurate 2D thermal model is desired for the analysis of the current distribution and associated non-uniform heat generation mechanisms.

### 6.2.2 Improvement of battery model using machine learning methods

The electrochemical model of lithium-ion cells is composed of a set of PDEs, ODEs, and nonlinear equations. Current numerical methods solve the above equations requiring relatively large computational time. In addition, several electrochemical, degradation and thermal mechanisms of the cells are not well understood and thus are difficult to be physically modeled. Based on the above considerations, the machine learning techniques might be a possible approach

for (1) accurately and effectively solving the coupled PDEs and ODEs, and (2) efficiently modeling the internal behaviors of the cell during operations to further increase the accuracy of the battery model.

## Reference

- [1] H. Liu, Z. Wei, W. He, and J. Zhao, "Thermal issues about Li-ion batteries and recent progress in battery thermal management systems: A review," *Energy Conversion and Management*, Vol. 150, pp. 304–330, 2017.
- [2] X. Zhao, Y. Yin, Y. Hu, and S.-Y. Choe, "Electrochemical-thermal modeling of lithium plating/stripping of  $\text{Li}(\text{Ni}_{0.6}\text{Mn}_{0.2}\text{Co}_{0.2})\text{O}_2/\text{Carbon}$  lithium-ion batteries at subzero ambient temperatures," *Journal of Power Sources*, Vol. 418, pp. 61–73, 2019.
- [3] P. Lyu, X. Liu, J. Qu, J. Zhao, Y. Huo, Z. Qu, and Z. Rao, "Recent advances of thermal safety of lithium ion battery for energy storage," *Energy Storage Materials*, Vol. 31, pp. 195–220, 2020.
- [4] Y. Yin, Y. Bi, Y. Hu, and S.-Y. Choe, "Optimal fast charging method for a large-format lithium-ion battery based on nonlinear model predictive control and reduced order electrochemical model," *Journal of The Electrochemical Society*, Vol. 167, No. 16, p. 160559, 2021.
- [5] J. Kim, J. Oh, and H. Lee, "Review on battery thermal management system for electric vehicles," *Applied Thermal Engineering*, Vol. 149, pp. 192–212, 2019.
- [6] W. Wu, S. Wang, W. Wu, K. Chen, S. Hong, and Y. Lai, "A critical review of battery thermal performance and liquid based battery thermal management," *Energy Conversion and Management*, Vol. 182, pp. 262–281, 2019.
- [7] M. Song, Y. Hu, S.-Y. Choe, and T. R. Garrick, "Analysis of the heat generation rate of lithium-ion battery using an electrochemical thermal model," *Journal of The Electrochemical Society*, Vol. 167, No. 12, p. 120503, 2020.
- [8] S. Gairola and Y. Hu, "A method for simultaneous state of charge, maximum capacity and resistance estimation of a Li-ion cell based on equivalent circuit model," *SAE Technical Paper Series*, 2020.
- [9] M. S. Patil, J.-H. Seo, S. Panchal, S.-W. Jee, and M.-Y. Lee, "Investigation on thermal performance of water-cooled Li-ion pouch cell and pack at high discharge rate with U-turn type microchannel cold plate," *International Journal of Heat and Mass Transfer*, Vol. 155, p. 119728, 2020.
- [10] L. H. J. Raijmakers, D. L. Danilov, R. A. Eichel, and P. H. L. Notten, "A review on various temperature-indication methods for Li-ion batteries," *Applied Energy*, Vol. 240, pp. 918–945, 2019.
- [11] N. Damay, C. Forgez, M. P. Bichat, and G. Friedrich, "A method for the fast estimation of a battery entropy-variation high-resolution curve – Application on a commercial  $\text{LiFePO}_4/\text{graphite}$  cell," *Journal of Power Sources*, Vol. 332, pp. 149–153, 2016.
- [12] C. Heubner, M. Schneider, and A. Michaelis, "Detailed study of heat generation in porous  $\text{LiCoO}_2$  electrodes," *Journal of Power Sources*, Vol. 307, pp. 199–207, 2016.

- [13] T. M. Bandhauer, S. Garimella, and T. F. Fuller, "A critical review of thermal issues in lithium-ion batteries," *Journal of Electrochemical Society*, Vol. 158, No. 3, p. R1, 2011.
- [14] R. Kantharaj and A. M. Marconnet, "Heat generation and thermal transport in lithium-ion batteries: A Scale-Bridging Perspective," *Nanoscale and Microscale Thermophysical Engineering*, Vol. 23, No. 2, pp. 128–156, 2019
- [15] J. S. Hong, H. Maleki, S. Al Hallaj, L. Redey, and J. R. Selman, "Electrochemical-calorimetric studies of lithium-ion cells," *Journal of The Electrochemical Society*, Vol. 145, No. 5, pp. 1489–1501, 1998.
- [16] S. A. Hallaj, J. Prakash, and J. Selman, "Characterization of commercial Li-ion batteries using electrochemical–calorimetric measurements," *Journal of Power Sources*, Vol. 87, No. 1-2, pp. 186–194, 2000.
- [17] H. Bang, H. Yang, Y. Kook Sun, and J. Prakash, "In situ studies of  $\text{Li}_x\text{Mn}_2\text{O}_4$  and  $\text{Li}_x\text{Al}_{0.17}\text{Mn}_{1.83}\text{O}_{3.97}\text{S}_{0.03}$  cathode by IMC," *Journal of The Electrochemical Society*, Vol. 152, No. 2, pp. A421–A428, 2005.
- [18] C. Lin, S. Xu, and J. Liu, "Measurement of heat generation in a 40 Ah  $\text{LiFePO}_4$  prismatic battery using accelerating rate calorimetry," *International Journal of Hydrogen Energy*, Vol. 43, No. 17, pp. 8375–8384, 2018.
- [19] K. Chen, G. Unsworth, and X. Li, "Measurements of heat generation in prismatic Li-ion batteries," *Journal of Power Sources*, Vol. 261, pp. 28–37, 2014.
- [20] L. Sheng, L. Su, H. Zhang, Y. Fang, H. Xu, and W. Ye, "An improved calorimetric method for characterizations of the specific heat and the heat generation rate in a prismatic lithium ion battery cell," *Energy Conversion and Management*, Vol. 180, pp. 724–732, 2019.
- [21] S. Panchal, I. Dincer, M. Agelin-Chaab, R. Fraser, and M. Fowler, "Experimental and theoretical investigations of heat generation rates for a water cooled  $\text{LiFePO}_4$  battery," *International Journal of Heat and Mass Transfer*, Vol. 101, pp. 1093–1102, 2016.
- [22] S. Panchal, S. Mathewson, R. Fraser, R. Culham, and M. Fowler, "Thermal management of lithium-ion pouch cell with indirect liquid cooling using dual cold plates approach," *SAE International Journal of Alternative Powertrains*, Vol. 4, No. 2, pp. 293–307, 2015.
- [23] M. Xiao and S.-Y. Choe, "Theoretical and experimental analysis of heat generations of a pouch type  $\text{LiMn}_2\text{O}_4$ /carbon high power Li-polymer battery," *Journal of Power Sources*, Vol. 241, pp. 46–55, 2013.
- [24] Y. Yin, Z. Zheng, and S.-Y. Choe, "Design of a calorimeter for measurement of heat generation rate of lithium ion battery using thermoelectric device," *SAE International Journal of Alternative Powertrains*, Vol. 6, No. 2, pp. 252–260, 2017.
- [25] Y. Hu, S.-Y. Choe, and T. R. Garrick, "Measurement of heat generation rate and heat sources of pouch type Li-ion cells," *Applied Thermal Engineering*, Vol. 189, p. 116709, 2021.
- [26] M. Guiatni and A. Kheddar, "Modeling identification and control of peltier thermoelectric modules for telepresence," *Journal of Dynamic Systems, Measurement, and Control*, Col.

133, No. 3, 2011.

- [27] B. M. Wilamowski and H. Yu, "Neural network learning without backpropagation," *IEEE Transactions on Neural Networks*, Vol. 21, No. 11, pp. 1793–1803, 2010.
- [28] K. E. Thomas, C. Bogatu, and J. Newman, "Measurement of the entropy of reaction as a function of state of charge in doped and undoped lithium manganese oxide," *Journal of The Electrochemical Society*, Vol. 148, No. 6, pp. A570–A575, 2001.
- [29] K. Takano, Y. Saito, K. Kanari, K. Nozaki, K. Kato, A. Negishi, and T. Kato, "Entropy change in lithium ion cells on charge and discharge," *Journal of Applied Electrochemistry*, Vol. 32, pp. 251–258, 2002.
- [30] P. J. Osswald, M. D. Rosario, J. Garche, A. Jossen, and H. E. Hoster, "Fast and accurate measurement of entropy profiles of commercial lithium-ion cells," *Electrochimica Acta*, Vol. 177, pp. 270–276, 2015.
- [31] J. P. Schmidt, A. Weber, and E. Ivers-Tiffée, "A novel and precise measuring method for the entropy of lithium-ion cells:  $\Delta S$  via electrothermal impedance spectroscopy," *Electrochimica Acta*, Vol. 137, pp. 311–319, 2014.
- [32] M. Balasundaram, V. Ramar, C. Yap, L. Li, A. A. Tay, and P. Balaya, "Heat loss distribution: impedance and thermal loss analyses in  $\text{LiFePO}_4$ /graphite 18650 electrochemical cell," *Journal of Power Sources*, Vol. 328, pp. 413–421, 2016.
- [33] R. Fu, S.-Y. Choe, V. Agubra, and J. Fergus, "Modeling of degradation effects considering side reactions for a pouch type Li-ion polymer battery with carbon anode," *Journal of Power Sources*, Vol. 261, pp. 120–135, 2014.
- [34] Y. Hu, Y. Yin, and S.-Y. Choe, "Accelerated equilibration for lithium-ion battery using optimal time control with electrochemical model," *Journal of Power Sources*, Vol. 480, p. 228623, 2020.
- [35] D. Zhang, B. N. Popov, and R. E. White, "Modeling lithium intercalation of a single spinel particle under potentiodynamic control," *Journal of The Electrochemical Society*, Vol. 147, No. 3, p. 831, 2000.
- [36] K. A. Smith, C. D. Rahn, and C.-Y. Wang, "Model order reduction of 1D diffusion systems via residue grouping," *Journal of Dynamic Systems, Measurement, and Control*, Vol. 130, No. 1, p. 011012, 2008.
- [37] F. M. Kindermann, A. Noel, S. V. Erhard, and A. Jossen, "Long-term equalization effects in Li-ion batteries due to local state of charge inhomogeneities and their impact on impedance measurements," *Electrochimica Acta*, Vol. 185, pp. 107–116, 2015.
- [38] J. T. Betts, *Practical methods for optimal control using nonlinear programming*, SIAM, 2001.
- [39] R. Klein, N. A. Chaturvedi, J. Christensen, J. Ahmed, R. Findeisen, and A. Kojic, "Optimal charging strategies in lithium-ion battery," *Proceedings of the 2011 American Control Conference*, 2011.

- [40] S. Lee, Y. Kim, J. B. Siegeland, and A. G. Stefanopoulou, "Minimum-time measurement of open circuit voltage of battery system," American Control Conference, pp. 884-889, June 2019.
- [41] Y. Hu, S.-Y. Choe, and T. R. Garrick, "Hybridized time-frequency method for the measurement of entropy coefficient of lithium-ion battery," *Electrochimica Acta*, Vol. 362, p. 137124, 2020.
- [42] C. Birkl, E. Mcturk, M. Roberts, P. G. Bruce, and D. Howey, "A parametric open circuit voltage model for lithium ion batteries," *Journal of The Electrochemical Society*, Vol. 162, No. 12, pp. A2271–A2280, 2015.
- [43] H. He, X. Zhang, R. Xiong, Y. Xu, and H. Guo, "Online model-based estimation of state-of-charge and open-circuit voltage of lithium-ion batteries in electric vehicles," *Energy*, Vol. 39, No. 1, pp. 310–318, 2012.
- [44] Y. Deng, C. Feng, J. E, H. Zhu, J. Chen, M. Wen, and H. Yin, "Effects of different coolants and cooling strategies on the cooling performance of the power lithium ion battery system: A review," *Applied Thermal Engineering*, Vol. 142, pp. 10–29, 2018.
- [45] H. P. Boehm, R. Setton, and E. Stumpp, "Nomenclature and terminology of graphite intercalation compounds," *Carbon*, Vol. 24, No. 2, pp. 241–245, 1986.
- [46] H. J. Noh, S. Youn, C. S. Yoon, and Y. K. Sun. " Comparison of the structural and electrochemical properties of layered Li [Ni<sub>x</sub>Co<sub>y</sub>Mn<sub>z</sub>]O<sub>2</sub> (x= 1/3, 0.5, 0.6, 0.7, 0.8 and 0.85) cathode material for lithium-ion batteries." *Journal of Power Sources*, Vol. 233, pp. 121-130, 2013.
- [47] G. Wirth, U. Hilleringmann, J. Horstmann, and K. Goser, "Negative differential resistance in ultrashort bulk MOSFETs," *IECON99. Conference Proceedings. 25th Annual Conference of the IEEE Industrial Electronics Society*.
- [48] K. E. Thomas and J. Newman, "Heats of mixing and of entropy in porous insertion electrodes," *Journal of Power Sources*, Vol. 119-121, pp. 844–849, 2003.
- [49] J. Huang, Z. Li, B. Y. Liaw, Z. Wang, S. Song, N. Wu, and J. Zhang, "Entropy coefficient of a blended electrode in a lithium-ion cell," *Journal of The Electrochemical Society*, Vol. 162, No. 12, 2015.
- [50] S. Skoog, "Electro-thermal modeling of high-performance lithium-ion energy storage systems including reversible entropy heat," 2017 IEEE Applied Power Electronics Conference and Exposition (APEC), 2017.
- [51] B. Wu, Z. Li, and J. Zhang, "Thermal design for the pouch-type large-format lithium-ion batteries," *Journal of The Electrochemical Society*, Vol. 162, No. 1, 2014.
- [52] K. Jalkanen, T. Aho, and K. Vuorilehto, "Entropy change effects on the thermal behavior of a LiFePO<sub>4</sub>/graphite lithium-ion cell at different states of charge," *Journal of Power Sources*, Vol. 243, pp. 354–360, 2013.
- [53] F.-L. Yun, W.-R. Jin, L. Tang, W. Li, J. Pang, and S.-G. Lu, "Analysis of capacity fade from entropic heat coefficient of Li[Ni<sub>x</sub>Co<sub>y</sub>Mn<sub>z</sub>]O<sub>2</sub>/graphite lithium ion battery," *Journal*

of The Electrochemical Society, Vol. 163, No. 5, 2016.

- [54] S. J. Bazinski and X. Wang, “The influence of cell temperature on the entropic coefficient of a lithium iron phosphate (LFP) pouch cell,” *Journal of The Electrochemical Society*, Vol. 161, No. 1, Apr. 2013.
- [55] J. R. Dahn, R. Fong, and M. J. Spoon, “Suppression of staging in lithium-intercalated carbon by disorder in the host,” *Physical Review B*, Vol. 42, No. 10, pp. 6424–6432, Jan. 1990.
- [56] K.-W. Nam, W.-S. Yoon, H. Shin, K. Y. Chung, S. Choi, and X.-Q. Yang, “In situ X-ray diffraction studies of mixed  $\text{LiMn}_2\text{O}_4\text{-LiNi}_{1/3}\text{Co}_{1/3}\text{Mn}_{1/3}\text{O}_2$  composite cathode in Li-ion cells during charge–discharge cycling,” *Journal of Power Sources*, Vol. 192, No. 2, pp. 652–659, 2009.
- [57] P. Röder, N. Baba, and H.-D. Wiemhöfer, “A detailed thermal study of a  $\text{Li}[\text{Ni}_{0.33}\text{Co}_{0.33}\text{Mn}_{0.33}]\text{O}_2/\text{LiMn}_2\text{O}_4$ -based lithium ion cell by accelerating rate and differential scanning calorimetry,” *Journal of Power Sources*, Vol. 248, pp. 978–987, 2014.
- [58] N. A. Cañas, P. Einsiedel, O. T. Freitag, C. Heim, M. Steinhauer, D.-W. Park, and K. A. Friedrich, “Operando X-ray diffraction during battery cycling at elevated temperatures: A quantitative analysis of lithium-graphite intercalation compounds,” *Carbon*, Vol. 116, pp. 255–263, 2017.
- [59] K. Maher and R. Yazami, “Effect of overcharge on entropy and enthalpy of lithium-ion batteries,” *Electrochimica Acta*, Vol. 101, pp. 71–78, 2013.
- [60] D. I. Stroe and E. Schaltz, “Lithium-ion battery state-of-health estimation using the incremental capacity analysis technique,” *IEEE Transactions on Industry Applications*, Vol. 56, No. 1, pp. 678–685, 2019.
- [61] A. Cordoba-Arenas, S. Onori, Y. Guezennec, and G. Rizzoni, “Capacity and power fade cycle-life model for plug-in hybrid electric vehicle lithium-ion battery cells containing blended spinel and layered-oxide positive electrodes,” *Journal of Power Sources*, Vol. 278, pp. 473–483, 2015.
- [62] K. Liu, K. Li, and C. Zhang, “Constrained generalized predictive control of battery charging process based on a coupled thermoelectric model,” *Journal of Power Sources*, Vol. 347, pp. 145–158, 2017.
- [63] K.-P. Chan and A. W.-C. Fu, “Efficient time series matching by wavelets,” *Proceedings 15th International Conference on Data Engineering (Cat. No.99CB36337)*, 1999.
- [64] Y. Hu and S.-Y. Choe, “Simultaneous and continuous characterization of reversible and irreversible heat of lithium-ion battery using wavelet transform technique,” *Electrochimica Acta*, Vol. 375, p. 137973, 2021.
- [65] A. Graps, “An introduction to wavelets,” *IEEE Computational Science and Engineering*, Vol. 2, No. 2, pp. 50–61, 1995.
- [66] A. J. Alhasan, D. D. White, and K. undefined Brabanterb, “Continuous wavelet analysis of pavement profiles,” *Automation in Construction*, Vol. 63, pp. 134–143, 2016.

- [67] X. Chen, L. Yin, Y. Fan, L. Song, T. Ji, Y. Liu, J. Tian, and W. Zheng, "Temporal evolution characteristics of PM<sub>2.5</sub> concentration based on continuous wavelet transform," *Science of The Total Environment*, Vol. 699, p. 134244, 2020.
- [68] S. S. Abdeldayem and T. Bourlai, "ECG-based human authentication using high-level spectro-temporal signal features," 2018 IEEE International Conference on Big Data (Big Data), 2018.
- [69] O. Alpar, "Online signature verification by continuous wavelet transformation of speed signals," *Expert Systems with Applications*, Vol. 104, pp. 33–42, 2018.
- [70] M. Misiti, Y. Misiti, G. Oppenheim, and J.M. Poggi. *Wavelet toolbox user's guide*, 2015.
- [71] I. Kiskin, D. Zilli, Y. Li, M. Sinka, K. Willis, and S. Roberts, "Bioacoustic detection with wavelet-conditioned convolutional neural networks," *Neural Computing and Applications*, Vol. 32, No. 4, pp. 915–927, Jan. 2018.
- [72] Z. Ren, K. Qian, Z. Zhang, V. Pandit, A. Baird, and B. Schuller, "Deep scalogram representations for acoustic scene classification," *IEEE/CAA Journal of Automatica Sinica*, Vol. 5, No. 3, pp. 662–669, 2018.
- [73] V. Subramanian, V. Diwakar and D. Tapriyal, "Efficient macro-micro scale coupled modeling of batteries," *Journal of The Electrochemical Society*, Vol. 152, No. 10, pp. A2002-A2008, 2005.
- [74] J. Forman, S. Bashash, J. Stein and H. Fathy, "Reduction of an electrochemistry-based li-ion battery model via quasi-linearization and Padé approximation," *Journal of The Electrochemical Society*, Vol. 158, No. 2, pp. A93-A101, 2011.
- [75] K. Smith, C. Rahn and C. Wang, "Model order reduction of 1d diffusion systems via residue grouping," *Journal of Dynamic Systems, Measurement, and Control*, Vol. 130, No. 1, pp. 011012, 2008.
- [76] L. Cai and R. White, "Reduction of model order based on proper orthogonal decomposition for lithium-ion battery simulations," *Journal of The Electrochemical Society*, Vol. 156, No. 3, pp. A154-A161, 2009.
- [77] X. Li, M. Xiao, and S.-Y. Choe, "Reduced order model (ROM) of a pouch type lithium polymer battery based on electrochemical thermal principles for real time applications," *Electrochimica Acta*, Vol. 97, pp. 66-78, 2013.
- [78] J. Vetter, P. Novák, M. R. Wagner, C. Veit, K-C. Möller, J. O. Besenhard, M. Winter, M. Wohlfahrt-Mehrens, C. Vogler, and A. Hammouche. "Ageing mechanisms in lithium-ion batteries," *Journal of power sources*, Vol 147, No. 1-2, pp. 269-281, 2005.
- [79] S. G. Marquis, V. Sulzer, R. Timms, C. P. Please, and S. J. Chapman, "An asymptotic derivation of a single particle model with electrolyte," *Journal of The Electrochemical Society*, Vol. 166, No. 15, 2019.
- [80] Y. Yin, Y. Hu, S.-Y. Choe, H. Cho, and W. T. Joe, "New fast charging method of lithium-ion batteries based on a reduced order electrochemical model considering side reaction," *Journal of Power Sources*, Vol. 423, pp. 367–379, 2019.

- [81] S. Cui, Y. Wei, T. Liu, W. Deng, Z. Hu, Y. Su, H. Li, M. Li, H. Guo, Y. Duan, W. Wang, M. Rao, J. Zheng, X. Wang, and F. Pan, "Optimized temperature effect of li-ion diffusion with layer distance in  $\text{Li}(\text{Ni}_x\text{Mn}_y\text{Co}_z)\text{O}_2$  cathode materials for high performance li-ion battery," *Advanced Energy Materials*, Vol. 6, No. 4, p. 1501309, 2015.
- [82] A. Tang, X. Wang, G. Xu, R. Peng, and H. Nie, "Chemical diffusion coefficient of lithium ion in  $\text{Li}_3\text{V}_2(\text{PO}_4)_3$  cathode material," *Materials Letters*, Vol. 63, No. 27, pp. 2396–2398, 2009.
- [83] X. Tang, L. Li, B. Huang, and Y. He, "Phenomenon of enhanced diffusion of lithium-ion in  $\text{LiMn}_2\text{O}_4$  induced by electrochemical cycling," *Solid State Ionics*, Vol. 177, No. 7-8, pp. 687-690, 2006.
- [84] Y. Wei, J. Zheng, S. Cui, X. Song, Y. Su, W. Deng, Z. Wu, X. Wang, W. Wang, M. Rao, Y. Lin, C. Wang, K. Amine, and F. Pan, "Kinetics tuning of li-ion diffusion in layered  $\text{Li}(\text{Ni}_x\text{Mn}_y\text{Co}_z)\text{O}_2$ ," *Journal of the American Chemical Society*, Vol. 137, No. 26, pp. 8364-8367, 2015.
- [85] S. Yang, X. Wang, X. Yang, Y. Bai, Z. Liu, H. Shu, and Q. Wei, "Determination of the chemical diffusion coefficient of lithium ions in spherical  $\text{Li}[\text{Ni}_{0.5}\text{Mn}_{0.3}\text{Co}_{0.2}]\text{O}_2$ ," *Electrochimica Acta*, Vol. 66, pp. 88-93, 2012.
- [86] Y. Hu, Y. Yin, Y. Bi, and S.-Y. Choe, "A control oriented reduced order electrochemical model considering variable diffusivity of lithium ions in solid," *Journal of Power Sources*, Vol. 468, p. 228322, 2020.
- [87] C. Delacourt, M. Ati, and J. M. Tarascon. "Measurement of lithium diffusion coefficient in  $\text{Li}_y\text{FeSO}_4\text{F}$ ," *Journal of The Electrochemical Society*, Vol. 158, No. 6, pp. A741-A749, 2011.
- [88] M. A. Cabañero, N. Boaretto, M. Röder, J. Müller, J. Kallo, and A. Latz, "Direct determination of diffusion coefficients in commercial li-ion batteries," *Journal of The Electrochemical Society*, Vol. 165, No. 5, 2018.
- [89] P.-C. Tsai, B. Wen, M. Wolfman, M.-J. Choe, M. S. Pan, L. Su, K. Thornton, J. Cabana, and Y.-M. Chiang, "Single-particle measurements of electrochemical kinetics in NMC and NCA cathodes for Li-ion batteries," *Energy & Environmental Science*, Vol. 11, No. 4, pp. 860-871, 2018.
- [90] M. Wang, M. Luo, Y. Chen, Y. Su, L. Chen, and R. Zhang, "Electrochemical deintercalation kinetics of  $0.5\text{Li}_2\text{MnO}_3 \cdot 0.5\text{LiNi}_{1/3}\text{Mn}_{1/3}\text{Co}_{1/3}\text{O}_2$  studied by EIS and PITT," *Journal of Alloys and Compounds*, Vol. 696, pp. 907-913, 2017.
- [91] S. Yang, X. Wang, X. Yang, Y. Bai, Z. Liu, H. Shu, and Q. Wei, "Determination of the chemical diffusion coefficient of lithium ions in spherical  $\text{Li}[\text{Ni}_{0.5}\text{Mn}_{0.3}\text{Co}_{0.2}]\text{O}_2$ ," *Electrochimica Acta*, Vol. 66, pp. 88-93, 2012.
- [92] P. Prosini, M. Lisi, and D. Zane. "Determination of the chemical diffusion coefficient of lithium in  $\text{LiFePO}_4$ ," *Solid State Ionics*, Vol. 148, pp. 45-51, 2002.
- [93] S.-I. Pyun and H.-C. Shin, "The kinetics of lithium transport through  $\text{Li}_{1-\delta}\text{CoO}_2$  thin film electrode by theoretical analysis of current transient and cyclic voltammogram," *Journal of*

Power Sources, Vol. 97-98, pp. 277-281, 2001.

- [94] D. Zhang, B. N. Popov, and R. E. White, "Modeling lithium intercalation of a single spinel particle under potentiodynamic control," *Journal of The Electrochemical Society*, Vol. 147, No. 3, p. 831, 2000.
- [95] Y. Zhao and S.-Y. Choe, "A highly efficient reduced order electrochemical model for a large format  $\text{LiMn}_2\text{O}_4$ /Carbon polymer battery for real time applications," *Electrochimica Acta*, Vol. 164, pp. 97-107, 2015.
- [96] D. M. Bernardi and J.-Y. Go, "Analysis of pulse and relaxation behavior in lithium-ion batteries," *Journal of Power Sources*, Vol. 196, pp. 412-427, 2011.
- [97] Q. Lai, S. Jangra, H.J. Ahn, G. Kim, W.T. Joe, and X. Lin, "Analytical sensitivity analysis for battery electrochemical parameters," *American Control Conference (ACC)*, pp. 890-896, 2019.
- [98] Y. Nesterov, "Introductory lectures on convex optimization: a basic course," Springer Science & Business Media, 2013.
- [99] R. Amin and Y.-M. Chiang, "Characterization of electronic and ionic transport in  $\text{Li}_{1-x}\text{Ni}_{0.33}\text{Mn}_{0.33}\text{Co}_{0.33}\text{O}_2$ (NMC333) and  $\text{Li}_{1-x}\text{Ni}_{0.50}\text{Mn}_{0.20}\text{Co}_{0.30}\text{O}_2$ (NMC523) as a function of li content," *Journal of The Electrochemical Society*, Vol. 163, No. 8, 2016.
- [100] P. Lyu, Y. Huo, Z. Qu, and Z. Rao, "Investigation on the thermal behavior of Ni-rich NMC lithium ion battery for energy storage," *Applied Thermal Engineering*, Vol. 166, p. 114749, 2020.
- [101] Q. Wang, C.-H. Shen, S.-Y. Shen, Y.-F. Xu, C.-G. Shi, L. Huang, J.-T. Li, and S.-G. Sun, "Origin of structural evolution in capacity degradation for overcharged NMC622 via operando coupled investigation," *ACS Applied Materials & Interfaces*, Vol. 9, No. 29, pp. 24731–24742, 2017.